









Nonequilibrium Processes in the Solar Corona, Transition Region, Flares, and Solar Wind (*Invited Review*)

Jaroslav Dudík¹  · Elena Dziřčáková¹ · Nicole Meyer-Vernet²  · Giulio Del Zanna³ · Peter R. Young^{4,5,6}  · Alessandra Giunta⁷ · Barbara Sylwester⁸  · Janusz Sylwester⁸  · Mitsuo Oka⁹  · Helen E. Mason³ · Christian Vocks¹⁰  · Lorenzo Matteini¹¹ · Sám Krucker¹² · David R. Williams¹³  · Šimon Mackovjak¹⁴

Received: 21 July 2016 / Accepted: 9 June 2017 / Published online: 31 July 2017
© Springer Science+Business Media B.V. 2017

Abstract We review the presence and signatures of the non-equilibrium processes, both non-Maxwellian distributions and non-equilibrium ionization, in the solar transition region, corona, solar wind, and flares. Basic properties of the non-Maxwellian distributions are described together with their influence on the heat flux as well as on the rates of individual collisional processes and the resulting optically thin synthetic spectra. Constraints on the presence of high-energy electrons from observations are reviewed, including positive detection of non-Maxwellian distributions in the solar corona, transition region, flares, and wind. Occurrence of non-equilibrium ionization is reviewed as well, especially in connection to hydrodynamic and generalized collisional-radiative modeling. Predicted spectroscopic signatures of non-equilibrium ionization depending on the assumed plasma conditions are sum-

✉ J. Dudík
dudik@asu.cas.cz

- 1 Astronomical Institute, Czech Academy of Sciences, Fričova 298, 25165 Ondřejov, Czech Republic
- 2 CNRS, PSL, LESIA, Observatoire de Paris, 5 place Jules Janssen, 92195 Meudon, France
- 3 DAMTP, University of Cambridge, Wilberforce Road, Cambridge CB3 0WA, UK
- 4 College of Science, George Mason University, Fairfax, VA, 22030, USA
- 5 NASA Goddard Space Flight Center, Code 671, Greenbelt, MD, 20771, USA
- 6 Northumbria University, Newcastle Upon Tyne, NE1 8ST, UK
- 7 STFC Rutherford Appleton Laboratory, Chilton, Didcot, Oxon. OX11 0QX, UK
- 8 Space Research Centre (CBK PAN), Warsaw, Bartycka 18A, Poland
- 9 Space Sciences Laboratory, University of California, Berkeley, CA, 94720, USA
- 10 Leibniz-Institut für Astrophysik, An der Sternwarte 16, 14482 Potsdam, Germany
- 11 Imperial College London, London SW7 2AZ, UK
- 12 University of Applied Sciences and Arts Northwestern Switzerland, Bahnhofstrasse 6, 5210 Windisch, Switzerland
- 13 ESAC, European Space Agency, Villanueva de la Cañada, 28692 Madrid, Spain
- 14 Institute of Experimental Physics, SAS, Watsonova 47, 04001 Košice, Slovak Republic

marized. Finally, we discuss the future remote-sensing instrumentation that can be used for the detection of these non-equilibrium phenomena in various spectral ranges.

Keywords Energetic particles, Electrons · Flares, Energetic particles · Spectral line, Theory · Spectral line, Intensity and diagnostics · Solar wind, Theory · Spectrum, X-ray

1. Introduction

Traditionally, optically thin astrophysical spectra are interpreted in terms of equilibrium. This means that the conditions in the emitting plasma are assumed to be time-independent and described by temperature, density, and emission measure. The very definition of temperature means that the distribution of particles is assumed to be Maxwellian. Alternatively, if the emission is time-dependent, it is assumed that the plasma evolves through a series of equilibria, and that its emission can be calculated at each instant from the instantaneous values of temperature, density, and emission measure.

When these assumptions are violated, non-equilibrium ensues. Processes creating the non-equilibrium can be either those leading to departures from a Maxwellian, *i.e.*, to non-Maxwellian distributions, or time-dependent non-equilibrium ionization, or both. Non-equilibrium ionization refers to the ionic composition (charge state) of plasma that is dependent on its evolutionary history. In the context of the upper solar atmosphere, transient ionization can arise as a result of dynamic phenomena that involve changes in the local plasma properties that are faster than the ionization timescales, such as rapid heating or cooling (*e.g.*, Bradshaw and Mason, 2003a,b; Bradshaw and Cargill, 2006; Olluri, Gudiksen, and Hansteen, 2013a; Martínez-Sykora *et al.*, 2016). Non-Maxwellians can be caused by a variety of processes, such as acceleration by electric fields, *e.g.*, during magnetic reconnection (*e.g.*, Petkaki and MacKinnon, 2011; Zharkova *et al.*, 2011; Burge, Petkaki, and MacKinnon, 2012; Burge, MacKinnon, and Petkaki, 2014; Cargill *et al.*, 2012; Gordovskyy *et al.*, 2013, 2014; Pinto *et al.*, 2016), turbulence (Hasegawa, Mima, and Duong-van, 1985; Laming and Lepri, 2007; Bian *et al.*, 2014), shocks or interaction of various waves such as whistlers with particles (Vocks, Mann, and Rausche, 2008; Vocks, Dzifčáková, and Mann, 2016), or long-range interactions inducing correlations among particles in the system (Tsalis, 1988, 2009; Collier, 2004; Leubner, 2004; Livadiotis and McComas, 2009, 2010, 2011, 2013). Moreover, since the cross-section for the Coulomb collisions among the particles varies with kinetic energy as E^{-2} , the collision frequency scales as $E^{-3/2}$, and thus it takes longer for high-energy particles to equilibrate. This is the basic reason for the occurrence of high-energy tails in astrophysical plasmas, as first pointed out by Scudder and Olbert (1979). Furthermore, density and temperature gradients in the plasma can lead to non-Maxwellian tails (*e.g.*, Roussel-Dupré, 1980a; Shoub, 1983; Ljepojevic and MacNeice, 1988). Scudder and Karimabadi (2013) showed that non-Maxwellians occur in regimes where the ratio of the electron mean free path to the pressure gradient (*i.e.*, the electron Knudsen number) is higher than 10^{-2} at any point along a magnetic field line. Such points are argued to be common above $1.05R_{\odot}$, *i.e.*, in the solar corona, but they could occur as low as in the solar transition region (TR) (see also Roussel-Dupré, 1980a).

Non-Maxwellian distributions have significant consequences for the physics of the solar atmosphere. For example, any observational analysis made under the assumption of a Maxwellian will yield an “observed” temperature that is different from the temperature that corresponds to the second moment of the distribution (Meyer-Vernet, 2007; Nicholls, Dopita, and Sutherland, 2012; Nicolaou and Livadiotis, 2016), and it can also depend on the

range of energies observed. In addition, any quantities derived from an integral over the particle distribution will be affected. These include not only the heat flux, which is the third moment of the distribution function, but also the rates of various spectroscopically important processes, such as excitation, ionization, and recombination (*e.g.*, Roussel-Dupré, 1980b; Owocki and Scudder, 1983; Bryans, 2006; Dzifčáková and Dudík, 2013), which affect the emission line intensities. We note that non-Maxwellians also affect magnetohydrodynamic (MHD) modeling, including the Chew, Goldberger, and Low (1956) approximation, since such models assume that the infinite hierarchy of moment equations can be truncated, *e.g.*, by assuming an expression for the heat flux that is dependent only on local plasma properties (Scudder, 1992a). Such assumptions are generally invalid if long-range interactions among particles are present (*cf.*, West, Bradshaw, and Cargill, 2008).

The focus of the present review is to describe these non-equilibrium processes and their consequences in the solar corona and wind, including the coronal boundary in the transition region (TR), and also in solar flares. The focus is on the mechanisms of optically thin emission in a collisionally dominated non-equilibrium plasma. We do not provide a review of the non-Maxwellians detected in other astrophysical plasmas, as these can be found elsewhere, *e.g.*, in Pierrard and Lazar (2010) and Bykov *et al.* (2013). An earlier review on the subject can be found in Bradshaw and Raymond (2013). A review on the kinetic effects in the solar wind, including non-Maxwellian distributions, can be found in Marsch (2006). We also note that we do not treat the radio emission arising from non-Maxwellian plasmas, *e.g.*, due to beam or loss-cone instabilities. Information on such processes can be found in Krueger (1979), Suzuki and Dulk (1985), Aschwanden (2005), Karlický (2009), Benáček, Karlický, and Yasnov (2017), and references therein. Similarly, we do not treat the non-equilibrium ionization of hydrogen and helium or other low-ionization stages belonging to the solar chromosphere, such as Ca II, as this would require the additional treatment of radiative transfer. We instead refer, *e.g.*, to the works of Heinzel (1991), Carlsson and Stein (2002), Leenaarts *et al.* (2007), Kašparová *et al.* (2009), Gudiksen *et al.* (2011), Wedemeyer-Böhm and Carlsson (2011), Golding, Carlsson, and Leenaarts (2014), Allred, Kowalski, and Carlsson (2015), and Golding, Leenaarts, and Carlsson (2016).

This review is structured as follows. Non-Maxwellian distributions and their consequences for the solar wind are described in Section 2, where the particular case of κ -distributions is treated in detail. This section also contains an overview of the processes that can lead to formation of the κ -distribution. The non-Maxwellian spectral synthesis is described in Section 3, which also includes a review of the detections of such non-Maxwellian distributions, or lack thereof. Solar flares are treated in Section 4, including the frequently present high-energy tails detected from bremsstrahlung emission, constraints on the particle distribution derived from imaging observations at lower energies, and spectroscopic signatures of non-Maxwellians in the emission line spectra containing dielectronic satellite lines. Non-equilibrium ionization is treated in Section 5, where we discuss timescales for equilibration, their dependence on electron density and on flows, and where we review the theoretical work on the importance of non-equilibrium ionization in the solar TR, corona, and flares. Future instrumentation that may lead to an advancement in the detection of non-equilibrium processes is briefly described in Section 6.

2. Kappa Distributions in the Solar Corona and Wind

As with most diffuse space and astrophysical plasmas, the outer solar corona and wind are not in equilibrium, and their particle velocity distributions exhibit suprathermal tails. This

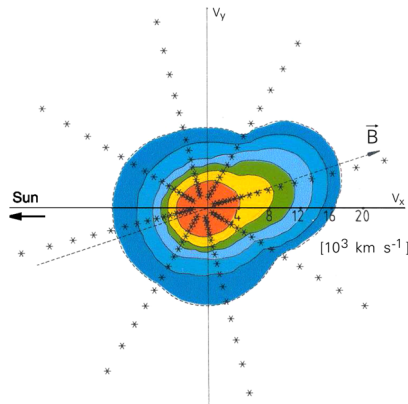


Figure 1 Electron velocity distribution in the fast solar wind measured by the plasma analyzer on *Helios* at 1 AU, showing three main components of the distribution: a cold core carrying the bulk of the electrons, a hotter halo, and the strahl, which is a suprathermal component directed along the magnetic field. The particle density is denoted by logarithmically spaced contours, and the starred lines delineate the detector resolution. The heat flux is carried by the strahl together with the halo, the hotter isotropic component that is slightly displaced with respect to the maximum of the core part indicated in red. *Reproduced with permission from Pilipp et al. (1987), © John Wiley and Sons.*

is illustrated in Figures 1, 2, and 3, and in Figure 8, which show classical examples of solar wind velocity distributions measured *in situ*.

Detailed analyses (see Tao *et al.*, 2016; Pierrard *et al.*, 2016, and references therein) have shown that the solar wind electron velocity distributions are close to Maxwellians at low energies, whereas higher energy electrons (the so-called halo) have a power-law energy distribution that can be modeled by a κ -distribution (see Section 2.1), with an additional strahl component beamed along the magnetic field, as shown in Figure 1. Non-Maxwellian electron distributions in the quiet solar corona or coronal holes and even in the high chromosphere have been proposed in order to explain these solar wind distributions (Olbert, 1981) and to resolve inconsistencies between spectroscopic and radio solar observations (Owociki, Townsend, and Ud-Doula, 1999; Pinfield *et al.*, 1999; Esser and Edgar, 2000; Chiuderi and Chiuderi Drago, 2004; Doyle *et al.*, 2004).

This nonthermal character considerably complicates the modeling and diagnostics of the plasma, since instead of being characterized by the two independent parameters of the Maxwellian (particle number density n and temperature T), the velocity distribution may in general have an infinite number of parameters.

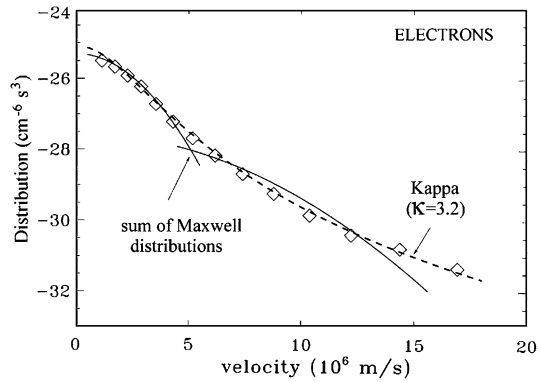
2.1. Kappa Distributions

The κ -distribution of velocities, which may be written

$$f_{\kappa}(v) \propto \left[1 + \frac{v^2}{\kappa v_{\text{th}}^2} \right]^{-\kappa-1}, \quad (1)$$

has long been recognized (Olbert, 1968; Vasyliunas, 1968a,b) as a very convenient tool to model distributions with suprathermal tails (Figure 2) because it is characterized by only three independent parameters: n , T , and κ . v_{th} is the thermal speed, and the index κ characterizes the nonthermal properties. In the limit $\kappa \rightarrow \infty$, the distribution converges to a

Figure 2 Electron velocity distribution measured in the slow solar wind with the particle analyzer on *Ulysses*, and fit with the sum of two Maxwellians (continuous lines) and with a κ -distribution (dashed line). From Meyer-Vernet (2001), adapted from Maksimovic, Pierrard, and Riley (1997). *Reproduced with permission, © John Wiley and Sons.*



Maxwellian:

$$f_M(v) \propto \exp(-v^2/v_{th}^2). \tag{2}$$

We note that Equations (1) and (2) represent isotropic velocity distributions, *i.e.*, the probability for the velocity to have components lying in the ranges $[v_x, v_x + dv_x]$, $[v_y, v_y + dv_y]$, and $[v_z, v_z + dv_z]$ is $f(v) dv_x dv_y dv_z$, with $v = (v_x^2 + v_y^2 + v_z^2)^{1/2}$; in other words, Equations (1) and (2) represent cuts along any direction, and the probability for the speed to lie between v and $v + dv$ is $f(v)$ times the corresponding volume in phase space, *i.e.*, $4\pi v^2 dv$.

Distributions (1) and (2) must be normalized, and the temperature is defined from $m\langle v^2 \rangle / 2 = 3k_B T / 2$, the average kinetic energy per particle of mass m , with k_B being the Boltzmann constant. The temperature T defined in this way is a kinetic temperature, but it also coincides with the thermodynamic temperature defined from the nonextensive entropy (Livadiotis and McComas, 2009; Livadiotis, 2015a). For the κ -distribution (1), this yields

$$T = \frac{\kappa}{\kappa - 3/2} \frac{m v_{th}^2}{2k_B}, \tag{3}$$

which requires $\kappa > 3/2$.

With Equation (3) for the temperature and $mv^2/2 = E$, the κ -distribution can be expressed in terms of kinetic energy E as (Owocki and Scudder, 1983)

$$f(E) dE = A_\kappa \frac{2}{\pi^{1/2} (k_B T)^{3/2}} \frac{E^{1/2} dE}{(1 + \frac{E}{(\kappa - 1.5)k_B T})^{\kappa + 1}}, \tag{4}$$

where

$$A_\kappa = \frac{\Gamma(\kappa + 1)}{\Gamma(\kappa - 0.5)(\kappa - 1.5)^{3/2}} \tag{5}$$

is the normalization constant (Figure 4). As noted above, T is the temperature.

It is important to note that the Debye length L_D , which is determined by the low-energy particles, is defined from $L_D^2 = [\epsilon_0 m / (ne^2)] / \langle v^{-2} \rangle$, with $\langle v^{-2} \rangle$ denoting the average of the inverse square speed (see, *e.g.*, Meyer-Vernet, 1993), so that (Chateau and Meyer-Vernet, 1991)

$$L_D = \frac{1}{\omega_p} \left(\frac{k_B T}{m} \frac{2\kappa - 3}{2\kappa - 1} \right)^{1/2}, \tag{6}$$

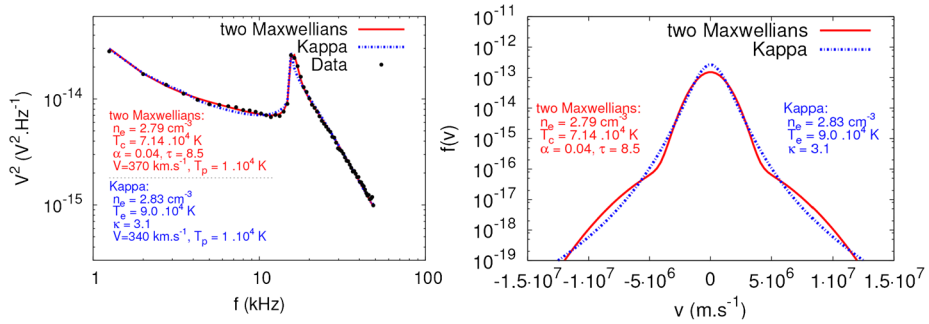


Figure 3 Plasma diagnostics with quasi-thermal noise spectroscopy. Left: Example of a power spectrum measured in the solar wind with the URAP receiver on *Ulysses*; the data are plotted as 64 heavy dots. The dash-dotted (solid) line shows the theoretical quasi-thermal noise with a κ -distribution and the sum of two Maxwellians that best fit the data with the parameters shown. Right: Comparison of the two distributions, κ and sum of two Maxwellians, determined from the power spectrum plotted on the left. *Reproduced with permission from Le Chat et al. (2010), © AIP Publishing LLC.*

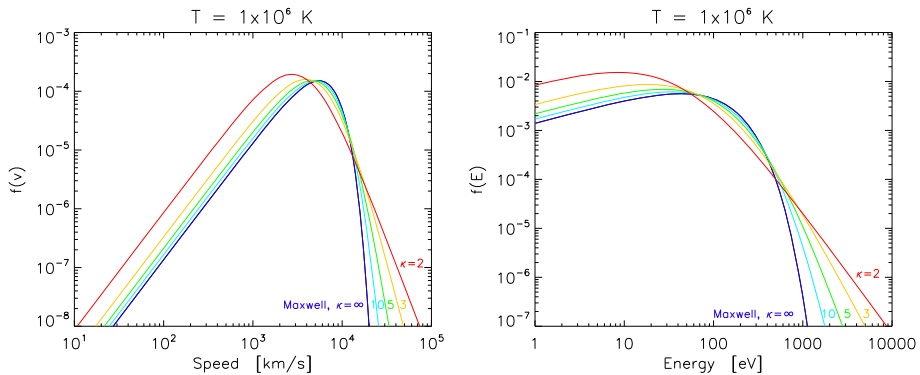


Figure 4 Speed (left) and energy (right) κ -distributions with $\kappa = 2, 3, 5, 10,$ and $25,$ and the Maxwellian distribution with $T = 10^6$ K. Colors correspond to different values of κ .

with the (angular) plasma frequency $\omega_p = (ne^2/\epsilon_0 m)^{1/2}$, where e is the electric charge and ϵ_0 the permittivity of the vacuum.

Equations (3) and (6) show that the smaller the index κ , the lower the most probable speed and the smaller the Debye length for a given temperature. This highlights the fact that at low speeds, the κ -distribution can be fit with a Maxwellian with a lower temperature than its actual kinetic temperature given by Equation (3). In contrast, at high speeds, the κ -distribution has a power-law shape that could mimic, although in a very narrow velocity range, a Maxwellian of much higher temperature. We show an example of this application in Section 2.5; depending on the energy range used in the analysis, a different “temperature” is revealed. This behavior illustrates the two faces of the κ -distribution, which are discussed in detail by Nicholls, Dopita, and Sutherland (2012). When properly taken into account, these two aspects enable one to resolve many apparent contradictions that can arise when Maxwellians are assumed to analyze observations.

2.2. Origin of Suprathermal Tails in Plasma Velocity Distributions

Suprathermal tails originate naturally from the plasma collisional properties, which are governed by Coulomb collisions. The cross-section for close Coulomb collisions is defined from the Landau radius, the distance at which the Coulomb interaction energy equals the kinetic energy. Hence the collisional cross-section decreases as the inverse square of the energy, which is the fundamental reason why velocity distributions have suprathermal tails in astrophysical plasmas, which as a rule are both diffuse and inhomogeneous. When the low-energy particles have a free path (proportional to their inverse collisional cross-section) on the order of magnitude of the scale height, particles moving three times faster, for instance, have a free path greater by a factor of 3^4 , which amounts to two orders of magnitude, as illustrated with a numerical simulation by Beck and Meyer-Vernet (2008). Hence, for the velocity distribution to be quasi-Maxwellian and the plasma amenable to a fluid description, the Knudsen number, the ratio of the mean free path to the scale height, should be much lower than unity (Scudder and Olbert, 1979, 1983), namely, lower than 10^{-3} (Shoub, 1983) or 10^{-2} (Scudder and Karimabadi, 2013), depending on the context. In practice, this means that in most space plasmas, including the solar TR, corona, and wind, velocity distributions should have suprathermal tails, as is indeed observed in the solar wind (see, *e.g.*, Pierrard and Lazar, 2010).

A number of additional mechanisms have been proposed for producing suprathermal tails in the corona and solar wind, such as turbulence, plasma instabilities, whistler waves, Langmuir fluctuations, and nanoflares (see Meyer-Vernet, 2001; Pierrard, Lazar, and Schlickeiser, 2011; Vocks, 2012; Che and Goldstein, 2014; Yoon *et al.*, 2016, and references therein). The wave-particle interaction involving whistler waves is discussed in Section 2.7. For the generation of κ -distributions by turbulence with a diffusion coefficient proportional to $1/v$, we refer to Hasegawa, Mima, and Duong-van (1985), Laming and Lepri (2007), and Bian *et al.* (2014). In the latter study, the κ -distributions are obtained analytically when the diffusive acceleration is balanced by Coulomb collisions in solar flare conditions.

Finally, nonextensive generalizations of thermodynamics involving long-range interactions in plasma have been shown to produce κ -distributions (see, *e.g.*, Tsallis, 2009; Livadiotis and McComas, 2009, 2013; Livadiotis, 2015b).

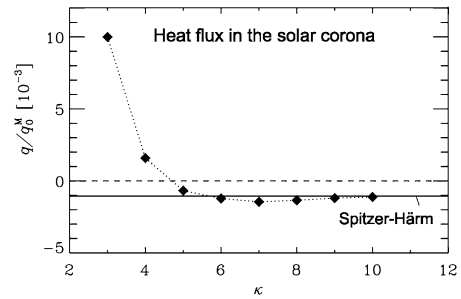
2.3. Effect of Suprathermal Tails on the Heat Flux

Since the heat flux is the third moment of the velocity distribution (in the frame where the mean velocity is zero), it is expected to be mainly carried by suprathermal electrons, which, as already noted, are generally noncollisional.

As has been found by Shoub (1983), the heat flux in the solar TR, corona, and wind is indeed generally not given by the standard collisional Spitzer and Härm (1953) value, even though the Knudsen number is smaller than unity (Scudder and Karimabadi, 2013). This point has recently been confirmed by Landi, Matteini, and Pantellini (2014).

Figure 5 shows how the heat flux in the solar corona changes when the velocity distributions differ from Maxwellians. The heat flux is calculated from a numerical simulation of Landi and Pantellini (2001), taking collisions into account for different values of κ . It is normalized to $10^{-3}q_0^M = 10^{-3}m_e n_0 v_0^3$, *i.e.*, to three orders of magnitude lower than the maximum heat flux that the plasma can presumably sustain; here, n_0 and $v_0 = (2k_B T_0/m_e)^{1/2}$ are the electron density and thermal speed at the base of the simulation. As expected, for $\kappa \rightarrow \infty$, the heat flux approaches the Spitzer–Härm value. However, as the suprathermal tail increases (κ decreases), the heat flux changes, and when $\kappa < 5$, the sign becomes opposite,

Figure 5 Heat flux q in the solar corona (normalized, as explained in the text), from a numerical simulation with different values of κ (dotted), compared to the classical Spitzer–Härm heat flux (solid line). *Credit: Landi and Pantellini (2001), reproduced with permission © ESO.*



with heat flowing upward, from cold to hot regions. Furthermore, for $\kappa \lesssim 3$, the heat flux exceeds the classical Spitzer–Härm value by one order of magnitude in addition to flowing upward (Landi and Pantellini, 2001).

We recall that whereas the ions carry the plasma momentum, heat is mainly transported by the electrons because of their low mass. In the solar wind, where the Knudsen number is much larger than in the corona, on the order of magnitude of unity, the heat flux is expected to be much closer to the noncollisional heat flux than to the classical Spitzer–Härm value. This noncollisional heat flux, introduced by Hollweg (1974), is produced by the fast electrons escaping from the interplanetary electric potential, which skew the solar wind electron velocity distribution since in the absence of collisions, no electrons are coming from infinity. This noncollisional heat flux is on the same order of magnitude as the Spitzer–Härm value in the solar wind at 1 AU (Meyer-Vernet, 2007), but both vary very differently with plasma properties since the noncollisional heat flux is roughly proportional to the electron density and to the wind speed. It has been shown from data and simulations that the solar wind heat flux behaves indeed as the noncollisional heat flux when the Knudsen number exceeds 0.01 (Landi, Matteini, and Pantellini, 2014), as predicted by Scudder and Karimabadi (2013).

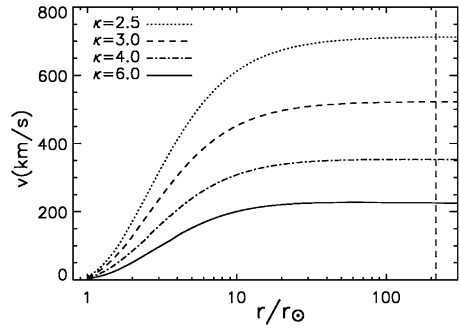
Since the noncollisional heat flux is produced by the tail of the electron velocity distribution, it increases when this tail exceeds the thermal value, which can have major consequences on the energy transport, affecting the temperatures and the wind acceleration. Examples are outlined in the next section.

2.4. Heating the Solar Corona and Accelerating the Solar Wind with Suprathermal Tails

Scudder (1992a,b) suggested that suprathermal particles at the base of the TR could be at the origin of the temperature increase with altitude, culminating at millions of degrees in the corona. This is because the particles around the Sun are subjected to an attracting potential, produced by gravity and by the electrostatic field that ensures plasma quasi-neutrality; this potential filters the particles because it confines the low-energy particles at the base of the atmosphere since they do not have enough energy to climb up the potential well, whereas the more energetic particles are capable of reaching higher altitudes. Hence, the particles' kinetic temperatures increase with altitude. Since the final temperatures increase with this potential, which depends on the mass and charge state, which is higher for heavy ions, minor ions can reach higher temperatures, as has been observed (see, *e.g.*, Pierrard and Pieters, 2014).

Suprathermal electrons not only contribute to heating the solar corona, they should also be capable of accelerating the solar wind, as proposed by Olbert (1981). This is easily understood by writing the energy equation between the base of the wind r_0 where the bulk speed

Figure 6 Solar wind speed as a function of heliospheric distance (normalized to the solar radius) from an exospheric model with different values of κ . From Zouganelis *et al.* (2004). © AAS. Reproduced with permission.



is negligible, and a large distance where both the enthalpy and the gravitational energy are negligible compared to the values at r_0 . This yields the terminal kinetic energy per wind unit mass (Meyer-Vernet, 2007),

$$V^2/2 = 5k_B T_0/m_p - M_{\odot}G/r_0 + q_0/(\rho_0 V_0). \tag{7}$$

Here, V is the terminal wind speed, m_p the proton mass, G the gravitational constant, M_{\odot} the solar mass, and T_0 , $\rho_0 V_0$, and q_0 the temperature, mass flux, and heat flux at the base of the wind, respectively. Equation (7) shows that with typical values of the parameters, accelerating the fast wind requires a heat flux at the base $q_0 \geq 70 \text{ W m}^{-2}$, which is much higher than the collisional heat flux (Meyer-Vernet, 2007). This shows that not only does the heat flux play a crucial role for accelerating the wind, but it must be much higher than the classical collisional value.

The simplest models applicable in that case are the so-called exospheric models (Lemaire, 2010). Such noncollisional models start with an assumed velocity distribution at the base of the wind and calculate the distribution farther away from the Sun by applying the Jeans theorem. In contrast to the fluid models (Parker, 2010), the heat flux is not assumed *a priori*, but calculated everywhere from the third moment of the velocity distribution. The calculations, which are fully self-consistent since the electric potential is calculated at all distances from charge quasi-neutrality and zero-charge flux, have been applied to κ -distributions (Maksimovic, Pierrard, and Lemaire, 1997). The terminal wind speed and electron temperature at large distances can even be estimated analytically as a function of κ (Meyer-Vernet and Issautier, 1998; Meyer-Vernet, 1999), suggesting that the high-speed wind can be produced with $\kappa \leq 3$. Figure 6 shows the wind speed computed as a function of heliocentric distance for different values of κ (Zouganelis *et al.*, 2004). Interestingly, the wind speeds predicted by the exospheric models have been confirmed by numerical simulations that take collisions into account (Zouganelis *et al.*, 2005). However, exospheric models are unable to correctly predict the particle velocity distributions, which must be computed using full kinetic simulations that take collisions into account (Landi, Matteini, and Pantellini, 2012).

Such kinetic simulations, which take only the basic particle properties into account, *i.e.*, expansion and collisions, can explain the solar wind observed electron heat flux that drives the electron energetics, but the effect of direct heating from external sources such as wave instabilities and turbulence is still debated (see, *e.g.*, Cranmer *et al.*, 2009; Landi, Matteini, and Pantellini, 2014).

2.5. *In Situ* Diagnostics in the Solar Wind from Thermal Noise Spectroscopy

Plasma particle velocity distributions are traditionally measured with electrostatic particle analyzers that separate and count the particles in different energy ranges. Such methods are often hampered by spacecraft charging effects; in the solar wind, this complicates the measurement of electrons with an energy lower than the (positive) spacecraft potential (Maksimovic *et al.*, 1995), which must be corrected for both this potential and the photoelectrons emitted by the spacecraft surfaces subjected to solar radiation, whose number density is much greater than that of the ambient solar wind electrons (Garrett, 1981; Salem *et al.*, 2001). A complementary technique is thermal noise spectroscopy (Meyer-Vernet *et al.*, 1998), which is almost immune to these problems because it senses a much larger plasma volume since it measures the electrostatic fluctuations that are produced by the quasi-thermal motion of the plasma particles. The power spectrum at the ports of an electric antenna of length exceeding the Debye length has a peak at the plasma frequency f_p (whose measurement reveals the electron density), of shape determined by the velocity distribution (Meyer-Vernet and Perche, 1989). The high-frequency spectral power density is proportional to the electron kinetic temperature, the low-frequency level is mainly determined by the Debye length (thus by low-energy electrons), whereas the level of the peak reveals high-energy electrons with a speed close to the phase speed of Langmuir waves, which becomes very high when $f \rightarrow f_p$ (Chateau and Meyer-Vernet, 1991).

Figure 3 (left) shows an example of power spectral density measured by the *Unified Radio and Plasma Wave Instrument* (URAP) onboard the *Ulysses* spacecraft (Stone *et al.*, 1992) in the solar wind (dots) fit with two models for the electron velocity distribution: a sum of 2 Maxwellians, and a κ -distribution, with the plasma parameters shown. Both distributions are plotted in the right panel of Figure 3. The fitting with two Maxwellians, labeled *c* and *h* (cold and hot), yields four electron parameters that can be expressed as the total electron density $n_e = n_c + n_h$, the temperature T_c of the cold Maxwellian, and the ratios of the densities $\alpha = n_h/n_c$ and densities $\tau = T_h/T_c$. In contrast, the fitting with a κ -distribution yields three electron parameters: n_e , T_e , and κ (Le Chat *et al.*, 2010). Both fits yield a similar kinetic temperature $T_e = T_c(1 + \alpha\tau)$.

The technique of quasi-thermal noise spectroscopy has been used on a number of space probes to measure electron properties in various solar system plasmas, including the solar wind near 1 AU and farther away from the Sun, on board the ISEE3, *Ulysses*, *Wind*, and STEREO spacecraft. It will be implemented in the solar wind near $60R_\odot$ on *Bepi-Colombo* (with the instrument SORBET, Moncuquet *et al.*, 2006), on *Solar Orbiter* (with RPW, Maksimovic *et al.*, 2005), and on *Solar Probe Plus* (with the instrument FIELDS, Bale *et al.*, 2016) near $10R_\odot$.

2.6. *In Situ* Observations of the Solar Wind Ions

Like the electrons, ions in the solar wind, especially protons and α particles, also show interesting and unexplained characteristics. Figure 7 shows a radial profile of the proton temperature as measured by *Helios* and *Ulysses* spacecraft, which orbit the Sun at 0.3–1 and 1.5–5 AU, respectively. During its expansion, the solar wind plasma cools down less strongly than expected. The red solid line shows the adiabatic prediction $T \propto R^{-4/3}$ for the spherical expansion of a monoatomic gas. The physical reasons for this departure of the solar wind temperatures from the adiabatic profile are not fully known. Measurements at distances of about 0.3 AU $\approx 60R_\odot$ are not yet available, but are planned with the next generation of

Figure 7 Proton temperature radial profile as measured by *Helios* (0.3–1 AU) and *Ulysses* (1.5–5 AU) in the fast solar wind. The adiabatic evolution for a collisional expanding gas is shown as the red line. Perihelions of the *Solar Orbiter* and *Solar Probe Plus* future missions are shown by dashed lines.

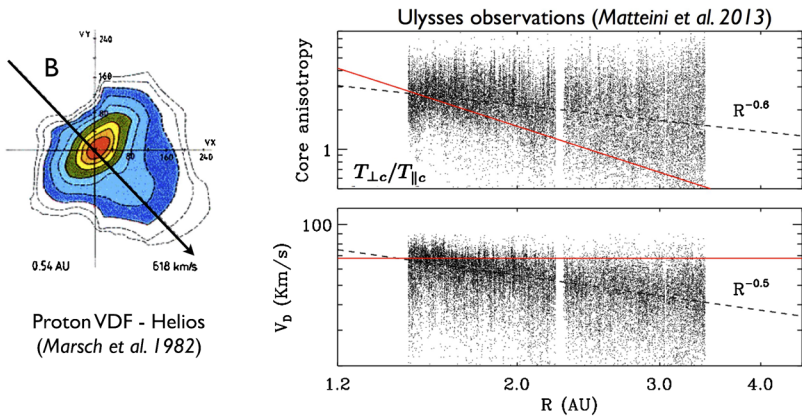
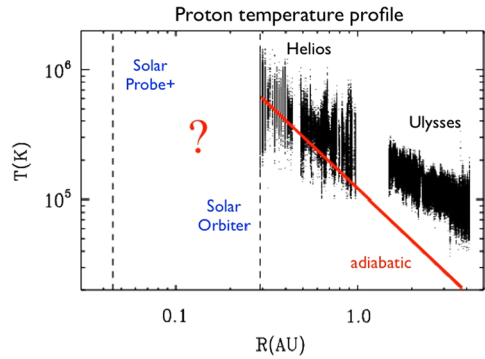


Figure 8 Left: typical proton velocity distribution measured in the fast solar wind by the *Helios* spacecraft. Typical nonthermal features are observed: anisotropy with respect to the local direction of the magnetic field (solid black line) and a relative drift between a thermal proton core and a secondary population (beam) that streams faster along the magnetic field. Right: radial evolution of nonthermal properties core anisotropy (top right) and core-beam relative drift normalized to the local Alfvén speed (bottom right). The red lines show the double-adiabatic expectations. Nonthermal properties are expected to be more enhanced closer to the Sun. *Reproduced with permission from Marsch et al. (1982b) and Matteini et al. (2013), © John Wiley and Sons.*

space missions such as *Solar Orbiter* and *Solar Probe Plus*,¹ which will explore the solar wind at regions as close as $10R_{\odot}$. (See Section 6 for a description of these spacecraft.)

Furthermore, like the electrons, the ion species in the solar wind are also characterized by nonthermal features (Marsch et al., 1982a,b). Distribution functions deviate from simple Maxwellians, but cannot be fully captured by a single κ model. Figure 8, left, shows an example of a typical proton velocity distribution in the solar wind. The local magnetic field, indicated by the black arrow, introduces a preferential direction with respect to which an anisotropy exists in terms of the proton velocity distribution functions (hereafter, VDFs). This leads to the introduction of two different kinetic temperatures along (T_{\parallel}) and across (T_{\perp}) the main magnetic field. Moreover, a secondary population streaming along the magnetic field ahead of the main core population is also present. Its form is sometimes that of a distinct secondary beam or of an elongated shoulder. As a consequence, it is convenient

¹<http://solarprobe.jhuapl.edu>.

to describe the proton distributions as the sum of two populations, core and beam, drifting along the magnetic field, each of them characterized by its own temperature anisotropy (usually assuming a bi-Maxwellian model). Detailed studies of such nonthermal properties suggests that wave-particle interactions driven by kinetic instabilities are at work in the solar wind and constrain the properties of proton distributions (see, *e.g.*, Matteini *et al.*, 2013, and references therein). Similar characteristics are observed for α particles (Maruca, Kasper, and Gary, 2012; Matteini *et al.*, 2015).

We note that strongly nonthermal ion distributions as described above, which are the consequence of the low plasma collisionality, also cast doubt on the comparison of the observations with the adiabatic temperature profile shown in Figure 7, as this is only valid for a fully collisional Maxwellian gas. For a more consistent description of the evolution of a collisionless plasma, a different model has to be used. An example of such a model is the double-adiabatic/CGL closure (*cf.*, Matteini *et al.*, 2012), where the abbreviation stands for Chew–Golberger–Low closure (Chew, Goldberger, and Low, 1956). This model separately considers the evolution of T_{\parallel} , T_{\perp} and particle drifts. Following this approach, the right panels of Figure 8 show the radial evolution of the core anisotropy and the relative core-beam drift in the high-latitude polar wind. The two quantities are compared with the associated CGL predictions for a radial magnetic field shown as the red line in Figure 8. The two profiles deviate from the prediction: the core anisotropy decreases less steeply than expected, suggesting some local heating sources for T_{\perp} , while the relative drift decreases with distance, which is a signature of a slowing down of the beam with respect to the core. These results confirm that instabilities might act during the wind expansion and regulate its nonthermal properties. Detailed calculations of the proton energetics (Hellinger *et al.*, 2011, 2013) show that additional external sources are needed to explain the observed temperature profiles. These are likely related to complex processes such as turbulence, shocks, and magnetic reconnection.

We note that local heating of ions along solar wind expansion cannot fully explain non-thermal features like those shown in Figure 7. Moreover, the observed radial trends (dashed lines) suggest that the proton properties, such as the core anisotropy and beam drift, are expected to be even more pronounced closer to the Sun. It is likely that these *in situ* signatures (anisotropy and beams) are generated in the corona and are slowly relaxed during expansion. This implies that *in situ* measurements closer to the Sun probably sample proton distributions with large departures from Maxwellian and significant contribution from suprathermal plateaus and beams. How such ion properties affect remote-sensing observations of the solar corona is an open question at present.

2.7. Formation and Evolution of Suprathermal Electron Distributions in the Solar Corona and TR

2.7.1. Suprathermal Electron Production in the Solar Corona

Solar wind observations of suprathermal particles, whose velocity distribution functions can be fit by κ -functions in the case of electrons, have been discussed above. Since no direct *in situ* observations are possible in the corona, we now discuss one possible mechanism for the formation of suprathermal electron tails in the solar corona and the TR. Pierrard, Maksimovic, and Lemaire (1999) have shown that suprathermal solar wind electrons in the keV energy range can exist at altitudes of $4R_{\odot}$.

Vocks *et al.* (2005) studied the formation of a suprathermal electron component from an initially Maxwellian distribution through resonant interaction with a given whistler wave

spectrum. There, the wave spectrum was chosen as a power law representing the high-frequency tail of wave spectra associated with coronal heating. This led to the formation of suprathermal tails in solar coronal and wind electron VDFs, showing that the suprathermal tail formation can be a by-product of the coronal heating mechanism.

To better understand the suprathermal tail formation process without the influence of open boundary conditions of the simulation box located both in the low corona and in the outer heliosphere, Vocks, Mann, and Rausche (2008) applied the same model on the closed volume of a coronal loop. These authors showed that power-law-like electron VDFs do form inside the loop, with energies of up to 10 keV. These models showed that the quiet solar corona is indeed capable of producing a substantial suprathermal electron population as a by-product of coronal heating. We note that this is probably robust against the actual details of the coronal heating mechanism, as long as it is associated with some electron acceleration. The treatment of suprathermal electron propagation and thermalization in the model, which competes with the production mechanism, is independent of the latter.

2.7.2. Propagation of Suprathermal Electrons in the TR

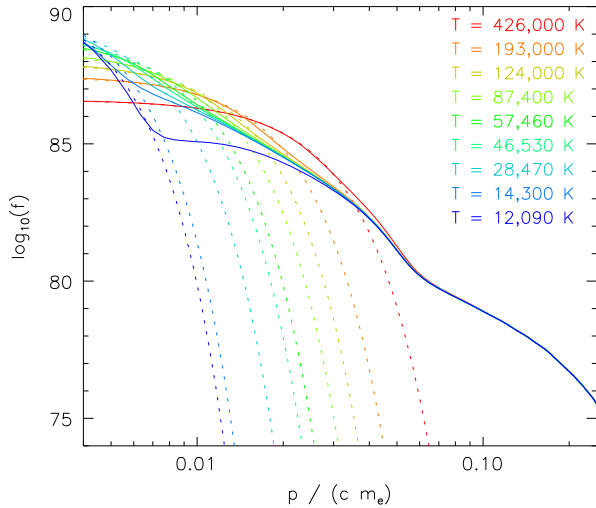
In the model of Vocks, Mann, and Rausche (2008), the footpoints of the closed loop were located in the TR. The interior of the simulation box was restricted to high temperatures above 5×10^5 K and did not include the TR and upper chromosphere. This was done to avoid too wide ranges of electron thermal speeds and phase space gradients inside the simulation box. However, suprathermal electrons from the corona do not stop at the TR. Since the Coulomb collisional mean free path scales as v^4 , coronal electrons are capable of traversing the TR and entering the cooler and denser chromosphere. The strong temperature gradient and associated heat flux in the TR readily suggests that TR electron VDFs can substantially deviate from a Maxwellian.

To investigate the propagation and evolution of the suprathermal electron population in the strong temperature gradients of the TR, Vocks, Džifčáková, and Mann (2016) extended the simulation box of Vocks, Mann, and Rausche (2008) into the upper chromosphere. This Vlasov kinetic model for electrons includes Coulomb collisions both with other electrons and the ion background. A Maxwellian distribution is assumed at the lower boundary in the chromosphere. For the upper boundary, the resulting VDF from the loop model of Vocks, Mann, and Rausche (2008) with its suprathermal tail is used. Since there are no heat sources or sinks in the model, a constant heat flux is assumed. The classic Spitzer $T^{5/2}$ law of thermal conductivity in a plasma then leads to a temperature profile with a steep temperature gradient, with a temperature change on the order of 10^4 K in just a few meters.

Figure 9 shows the resulting pitch-angle-averaged electron VDFs for different temperature levels in the TR. An electron momentum of $p = 0.1 m_e c$ corresponds to a kinetic energy of 2.5 keV. The energy range of the suprathermal electrons shown here therefore covers a few tens of eV up to 10 keV. Maxwellian VDFs with the same densities and temperatures are plotted as dashed lines for reference. The power-law tail of suprathermal electrons is clearly visible in all plots. We note that the VDFs are not normalized. Instead, their numerical values are plotted in absolute units, *i.e.*, $\text{kg}^{-3} \text{m}^{-6} \text{s}^6$. In this way, it can readily be seen that the suprathermal electrons are hardly absorbed within the thin TR and that their phase-space density stays nearly constant. Only the line for the lowest temperature, $T = 12090$ K, shows some deviation for momentum $p < 0.02 m_e c$, which corresponds to electron energies below 100 eV. These electrons are absorbed as a result of the high chromospheric density and the v^4 scaling of collisional mean free paths.

These simulation results show that TR electron VDFs can be far from the thermal equilibrium that is characterized by Maxwellian VDFs.

Figure 9 Pitch-angle-averaged electron VDFs at different positions in the simulation box (solid lines) and Maxwellian VDFs with the same density and temperature (dotted lines). Credit: Vocks, Dzifčáková, and Mann (2016), reproduced with permission © ESO.



3. Remote-Sensing Diagnostics of Nonthermal Distributions in the Solar Corona and TR

Remote-sensing observations of the solar corona are becoming increasingly detailed, and high-resolution spectroscopy is becoming more common. It has become clear that spectroscopic evidence of nonthermal electron distributions in the solar corona, other than during the impulsive phase of flares, and especially in the source regions of solar wind, requires not only very well calibrated observations, but also a wide range of accurate atomic data and modeling. In this section, we discuss the optically thin spectral synthesis and the behavior of the resulting synthetic spectrum when non-Maxwellian distributions are considered. Although we consider primarily the κ -distributions, the spectral synthesis for any non-Maxwellian distribution can be made in an analogous manner.

3.1. Line Intensities and Atomic Data

The intensity of an optically thin spectral line at wavelength λ_{ji} depends mainly on the abundance of the emitting ion X^{+z} and the relative population of the upper emitting level j , $N(X_j^{+z})/N(X^{+z})$ (e.g., Mason and Monsignor Fossi, 1994; Phillips, Feldman, and Landi, 2008),

$$\begin{aligned}
 I_{ji} &= A_X \int \frac{hc}{\lambda_{ji}} A_{ji} N(X_j^{+z}) dl = A_X \int \frac{hc}{\lambda_{ji}} \frac{A_{ji}}{n_e} \frac{N(X_j^{+z})}{N(X^{+z})} \frac{N(X^{+z})}{N(X)} n_e n_H dl \\
 &= A_X \int G_{X,ji}(T, n_e, \kappa) n_e n_H dl,
 \end{aligned}
 \tag{8}$$

where hc/λ_{ji} is the photon energy, λ_{ji} is the emission line wavelength, A_{ji} is the Einstein coefficient for spontaneous emission, and $N(X^{+z})/N(X)$ is the relative ion abundance of the X^{+z} ion. The relative abundance of the element X is denoted by A_X and is usually assumed to be constant along the line of sight l . In the above expression, the n_H and n_e represent the hydrogen and electron number densities, respectively. The function $G_{X,ji}(T, n_e, \kappa)$ is called the line contribution function. It depends on κ (or any other nonthermal parameter) through

the dependence of the individual underlying atomic processes that result in ionization, recombination, excitation, and de-excitation on κ (e.g., Dzifčáková, 1992; Dzifčáková and Kulinová, 2001; Dzifčáková, 2002, 2006; Wannawichian, Ruffolo, and Kartavykh, 2003; Dzifčáková and Mason, 2008; Dzifčáková and Dudík, 2013; Dudík *et al.*, 2014a,b; Dzifčáková *et al.*, 2015).

In case of isothermal plasma, the quantity $EM = \int n_e n_H dl$ gives the total emission measure of the plasma. However, when the coronal plasma is not isothermal, but the emission along the line of sight arises in regions with different temperatures, the intensity is given by

$$I_{ji} = A_X \int G_{X,ji}(T, n_e, \kappa) DEM_\kappa(T) dT, \tag{9}$$

where the quantity $DEM_\kappa(T) = n_e n_H dl/dT$ is the differential emission measure, generalized for κ -distributions by Mackovjak, Dzifčáková, and Dudík (2014).

The above expressions (8)–(9) assume a fundamental approximation that processes affecting the population of atomic states within an ion can be separated from those that affect the populations of different ions in the plasma. This is justified since the timescales for ionization and recombination processes are typically longer than those for electron excitation. Departures from this situation, including nonequilibrium ionization, are discussed in Section 5. In some cases, ionization and recombination can significantly modify the level populations of an ion, but in the case of ionization equilibrium, this can be treated without the need to fully integrate all atomic processes in a single model that incorporates all ions of an element (see Landi *et al.*, 2006).

Accurately solving the level balance equations for individual ions is the key goal of the CHIANTI atomic database (Dere *et al.*, 1997; Landi *et al.*, 2013; Del Zanna *et al.*, 2015a) and software. This requires large quantities of atomic data describing the ionization, recombination, excitation, and de-excitation processes. These processes are treated in the following Sections 3.2–3.4. The dominant excitation process in the solar atmosphere is by electron collisions, but the low electron density means that the dominant de-excitation process is spontaneous radiative decay, and so the plasma is far from thermal equilibrium. This requires that the level balance equations are solved by including all relevant atomic processes between individual atomic states. CHIANTI ion models can contain hundreds of states, leading to tens of thousands of rates.

The key parameters for describing any electron collision process are the electron flux and the cross-section offered by the ion to change it from an excited atomic state i to a state j . For an isotropic particle distribution, the flux of electrons of energy $E = mv^2/2$ is $n_e v f(E) dE$, where $f(E)$ is the particle distribution function. The number of transitions occurring per unit volume per unit time is $n_i \sigma_{ij} n_e v f(E) dE$, where $n_i = N(X_i^{+z})/N(X^{+z})$ is the number density of ions in a state i and σ_{ij} is the cross-section offered by the target ion for transitions to the state j . Integrating over energy leads to the following definition for the excitation rate coefficient:

$$C_{ij} = \int_{E_{ij}}^\infty \sigma_{ij} v f(E) dE, \tag{10}$$

where $E_{ij} = E_j - E_i$ is the energy separation of states i and j , and C_{ij} is usually given in units of $\text{cm}^3 \text{s}^{-1}$. For the ionization and recombination, the total rate coefficient is obtained analogously, with the state j then belonging to the ionized ion X^{+z+1} , and for recombination it belongs to the recombined ion X^{+z-1} . From now on, we use C , q , and α for the excitation, ionization, and recombination rate coefficients, respectively.

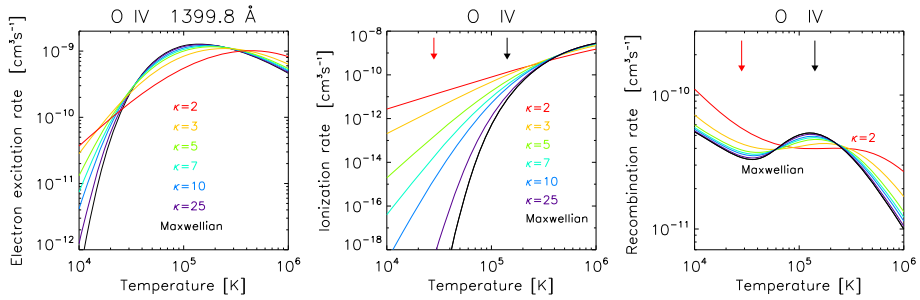


Figure 10 Collisional rates for O IV and their behavior for the κ -distributions: electron excitation rate for the 1399.8 Å line (left), ionization (middle), and recombination rate (right). Temperatures corresponding to the peak of the relative O IV abundance for the Maxwellian and $\kappa = 2$ distribution are shown by the black and red arrows, respectively.

3.2. Electron Excitation

Accurate electron excitation cross-sections are the key data for computing the populations of upper emitting levels that enter into Equation (8). Atomic physicists generally compute the *collision strength* rather than the cross-section (see, *e.g.*, Phillips, Feldman, and Landi, 2008), and an integral over a Maxwellian distribution yields the *effective collision strength*.

In general, atomic physicists publish only the effective collision strengths because the collision strength datasets are large, usually tens of thousands of datapoints for tens of thousands of transitions, which prevents researchers from computing effective collision strengths for non-Maxwellian distributions. One solution is to express the non-Maxwellian as a superposition of Maxwellians, which was implemented in CHIANTI version 5 (Landi *et al.*, 2006) and has recently been discussed in Hahn and Savin (2015), who provided an accurate way to decompose a κ -distribution into a linear series of Maxwellian distributions with different temperatures. Individual non-Maxwellian rates can then be calculated as a linear combination of the Maxwellian rates. A decomposition like this is in principle possible for any non-Maxwellian distribution broader than a single Maxwellian. Summing over many Maxwellians, however, increases the computational time accordingly. Another way to model the non-Maxwellian spectra is to recover the (smooth) behavior of the cross-sections via a parameterization method. This normally provides cross-sections that are accurate to within a few percent of the original values (see, *e.g.*, Dzifčáková and Mason, 2008; Dzifčáková *et al.*, 2015). Once the cross-sections are recovered, it is trivial to convolve them with non-Maxwellians to obtain the rate coefficients. For the κ -distributions, this method has been implemented using the CHIANTI database (version 7.1) and made available to the community via the KAPPA² package (Dzifčáková *et al.*, 2015). An example of the electron excitation rate coefficient for the 1401.2 Å line of O IV and its behavior for κ -distributions is shown in the left panel of Figure 10. We see that the excitation rate is enhanced and low and high temperatures, especially for low κ values, and that its peak is decreased and shifted toward higher T .

The UK APAP network³ (led by N.R. Badnell, University of Strathclyde) have computed a large amount of electron excitation data for spectral modeling in recent years, and a

²<http://kappa.asu.cas.cz>.

³<http://www.apap-network.org>.

database of collision strengths has been built that allows line intensities to be calculated in nonequilibrium conditions (Dudík *et al.*, 2014a,b).

3.3. Ionization and Recombination

3.3.1. Ionization

Electron-impact ionization can take place either directly or through excitation to an unstable state above the ionization threshold that then autoionizes. The cross-sections for both direct and excitation–autoionization can be expressed as analytic forms in terms of the electron energy or temperature (*e.g.*, Younger, 1981; Arnaud and Raymond, 1992), fit to computational or laboratory data. These allow ionization rates to be calculated for arbitrary electron distributions, including nonequilibrium distributions (Dzifčáková and Dudík, 2013). An example of the total ionization rate and its behavior with κ is shown for O IV in Figure 10. We see that the ionization rate increases by orders of magnitude, especially at low T .

3.3.2. Recombination

Recombination is the capture of an electron into a stable excited level of an ion. The direct process is referred to as radiative recombination (RR), while capture into an unstable doubly-excited state that then radiatively decays to a stable state is called dielectronic recombination (DR). RR and DR rates are generally computed separately.

Atomic physicists compute RR rates from photoionization cross-sections as the two processes are related by the principle of detailed balance (*e.g.*, Phillips, Feldman, and Landi, 2008). Cross-sections for transitions from the ground and excited states of the recombined ion to the ground state of the recombining ion are needed, and the rates are generally published as the parameters of analytical fit formulae that are functions of temperature (*e.g.*, Gu, 2003; Badnell, 2006). Non-Maxwellian rates would require access to the original cross-sections, but Dzifčáková (1992) presented a method that allows κ -distribution rates to be computed directly from the Maxwellian fit parameters. This was applied by Dzifčáková and Dudík (2013) to all ions available in CHIANTI.

For DR, the inverse process to dielectronic capture is autoionization and modern calculations (*e.g.*, Badnell *et al.*, 2003) typically compute the DR rates from the autoionization rates and the radiative decay rates that stabilize the doubly-excited states. The DR rates are generally published as the parameters of a fitting formula that is a function of temperature (*e.g.*, Arnaud and Raymond, 1992). Dzifčáková (1992) and Dzifčáková and Dudík (2013) provided a modified formula and fit parameters for the κ -distribution, while rates for other distributions can be derived numerically by integrating the dielectronic capture rates. An example of the total recombination rate for O IV and its behavior for κ -distributions is shown in Figure 10, right.

3.3.3. Behavior of the Ionization Equilibrium for the κ -Distributions

When the ionization and recombination rates are obtained, the ionization equilibrium can be calculated under the assumption that the total number of ionizing transitions is balanced by the total number of recombining transitions,

$$0 = n_e [q^{(z-1)} N^{(z-1)} + (q^{(z)} + \alpha^{(z)}) N^{(+z)} + \alpha^{(z+1)} N^{(z+1)}], \tag{11}$$

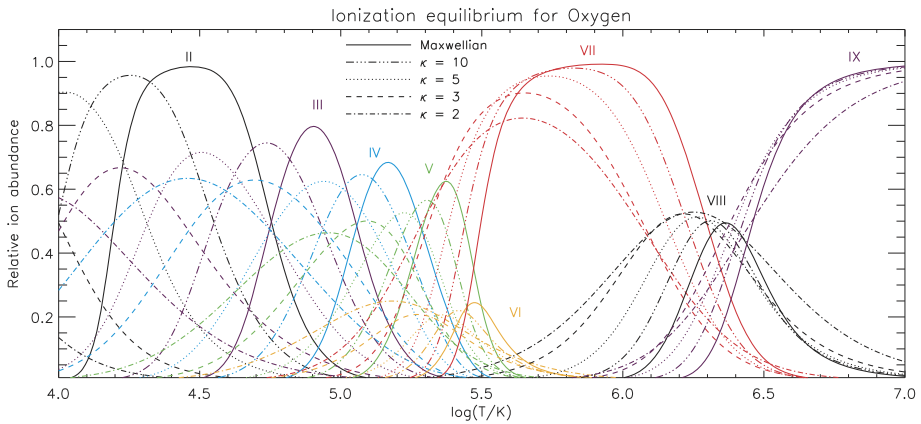


Figure 11 Behavior of the oxygen ionization equilibrium for the κ -distributions. Relative ion abundances for individual ions are shown in different colors, while different line-styles stand for different values of κ .

where we used a shortened notation $N^{(+z)} = N(X^{+z})$. A number of such ionization equilibrium calculations have been published for different sets of cross-sections. For the Maxwellian distributions, older calculations of Arnaud and Rothenflug (1985), Arnaud and Raymond (1992), Mazzotta *et al.* (1998) and Bryans, Landi, and Savin (2009) were available in the CHIANTI database up to version 7.1 (Landi *et al.*, 2013). State-of-the-art calculations use the ionization rates of Dere (2007) and the dielectronic recombination rates calculated by Badnell *et al.* (2003, and subsequent articles). These rates were used by Dzifčáková and Dudík (2013) to calculate the corresponding ionization balances for the κ -distributions. These are available within the KAPPA package.⁴

For the κ -distributions, individual ions can typically exist in a wider range of temperatures than for the Maxwellian distribution. An example for oxygen is shown in Figure 11. The TR ions are furthermore strongly shifted toward lower temperatures as a consequence of the rapidly increasing total ionization rate, by orders of magnitude (see, *e.g.*, Figure 2 in Dzifčáková and Dudík, 2013) dominated by the high-energy tail of the κ -distribution. In contrast, the recombination is dominated by the low-energy electrons. At coronal temperatures, the shift of the peak of the relative ion abundance can be either to higher or lower temperatures. For coronal Fe ions, the shift is typically toward higher $\log(T)$. For oxygen, O VIII is shifted toward lower T , while the behavior is opposite for O IX (Figure 11).

3.3.4. Density-Dependent Effects on the Ionization State

The tabulations of ion charge-state distributions that are widely used in the literature are computed in the zero-density approximation, *i.e.*, recombination and ionization take place only out of the ground states of the ions. However, high electron densities can alter the ionization state of the plasma. A strong effect is the suppression of dielectronic recombination. This occurs because intermediate states below the ionization threshold that are populated through cascading as the stabilization process proceeds can be reionized by electron collisions. The suppression of dielectronic recombination was estimated by collisional-radiative models and tabulated by Summers (1974a,b). Nikolić *et al.* (2013) used these tabulated rates

⁴<http://kappa.asu.cas.cz>.

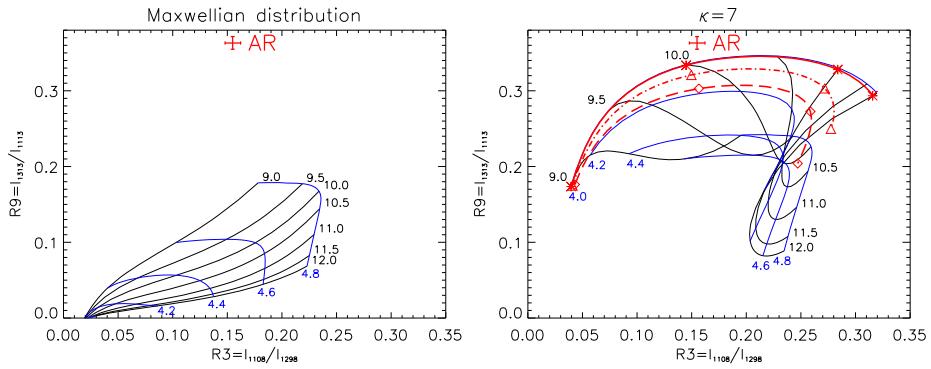


Figure 12 Si III line intensity ratios observed in the active region spectrum by Pinfield *et al.* (1999) and analyzed for the κ -distributions by Dzifčáková and Kulinová (2011). Left: Maxwellian-predicted ratios as a function of $\log(T$ [K]) and $\log(n_e$ [cm^{-3}]). Right: the same for the $\kappa = 7$. The red lines show the predicted ratios for several DEMs from the CHIANTI database. Credit: Dzifčáková and Kulinová (2011), reproduced with permission © ESO.

to compute the density-dependent suppression factors for the zero-density DR rates of Badnell *et al.* (2003) and subsequent articles.

Another effect of high density is that metastable states of the ions can be significantly populated so that the ionization and recombination from these states also need to be taken into account. Both density effects are modeled in the Atomic Data and Analysis Structure (ADAS),⁵ which uses the generalized collisional-radiative (GCR) approach (McWhirter and Summers, 1984; Summers *et al.*, 2006) to simultaneously include all radiative and electron collision processes, and the influence of highly excited states onto the dominant resolved low-lying states. The calculation yields effective ionization and recombination rates as functions of temperature and density, and these are made available through OPEN-ADAS.⁶ An example of the relative ion abundances of Si IV, O IV, and S IV that takes these effects into account can be found in Figure 13 of Polito *et al.* (2016a).

3.4. Diagnostics from TR Lines

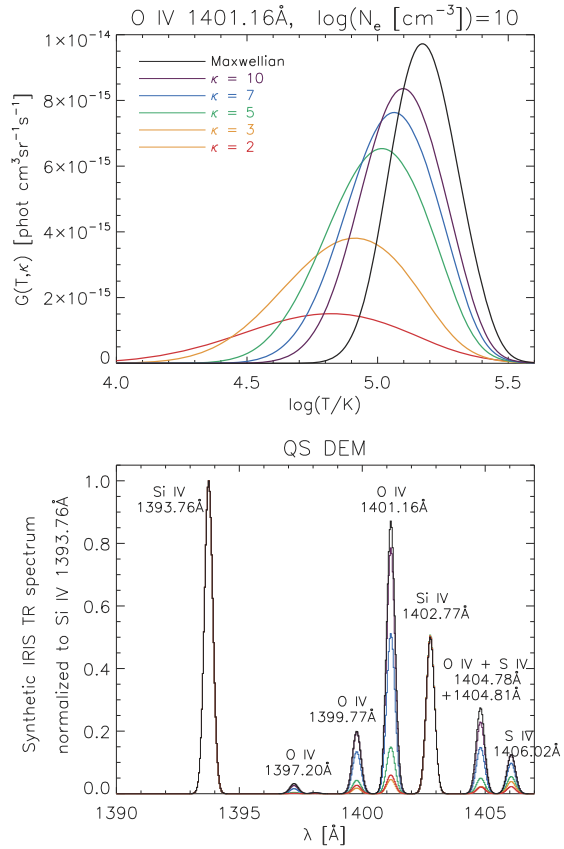
The solar TR is highly dynamic, with steep temperature gradients and strong flows, therefore nonequilibrium effects are expected. Section 5 discusses how line intensities are affected by departures from ionization equilibrium. Here, we consider the effect of non-Maxwellian distributions.

Earlier suggestions of departures from Maxwellian distributions in the solar TR were put forward by Dufton, Kingston, and Keenan (1984) and later by other authors (*e.g.*, Keenan *et al.*, 1989; Pinfield *et al.*, 1999). Pinfield *et al.* (1999) found anomalously high intensities in a high-excitation line from Si III observed by SOHO/SUMER (Wilhelm *et al.*, 1995) and suggested that these discrepancies could have been caused by the presence of non-Maxwellian electron distributions with high-energy tails. Dzifčáková and Kulinová (2011) analyzed these measurements and showed that the spectra are consistent with the presence of κ -distributions when the effect of photoexcitation is taken into account. The values of κ

⁵<http://adas.ac.uk>.

⁶<http://open.adas.ac.uk>.

Figure 13 Behavior of the IRIS spectra for the κ -distributions. Top: contribution functions $G(T, n_e, \kappa)$ for the O IV 1401.16 Å line, calculated at fixed density of $\log(n_e[\text{cm}^{-3}]) = 10$ and for different κ . Bottom: simulated IRIS Si IV, O IV, and S IV line profiles in the IRIS FUV channel, normalized to the Si IV intensities. The calculations have been revised using the atomic data corresponding to CHIANTI 8. From Dudík et al. (2014b), © AAS. Reproduced with permission.



found were rather high, $\kappa = 13$ and 11 for the observed coronal hole and quiet-Sun Si III, respectively, while $\kappa = 7$ was found for the active region spectrum (Figure 12). However, Del Zanna, Fernández-Menchero, and Badnell (2015) showed, using new atomic data calculated using the R-Matrix method, that the observed Si III line intensities are consistent with Maxwellian electrons when the temperature distributions of the plasma are taken into account. The only exception is the active region spectrum. However, the SUMER observations for all Si III lines were not simultaneous. The results of Del Zanna, Fernández-Menchero, and Badnell (2015) clearly indicate that accurate atomic data and modeling are necessary before any non-Maxwellian effects can be established.

Since 2013, the *Interface Region Imaging Spectrometer* (IRIS, De Pontieu et al., 2014) has been observing the TR Si IV, O IV, and S IV lines in the vicinity of 1400 Å. Previous work has demonstrated that some lines such as those from Si IV can be enhanced relative to the O IV lines by factors of five or more compared to the expected ratios in equilibrium conditions (e.g., Doyle and Raymond, 1984; Judge et al., 1995; Curdt et al., 2001; Yan et al., 2015), compared to other lines such as O IV that are formed at similar temperatures, assuming equilibrium conditions. Dudík et al. (2014b) showed that using a Maxwellian distribution and typical TR DEMs, the O IV 1401.16 Å line should be stronger than the neighboring Si IV line at 1402.77 Å when photospheric abundances are considered. Using coronal abundances would increase the predicted Si IV line by a factor of 3–4, which is still not enough to explain the observed spectra. However, considering the κ -distributions,

the Si IV line strongly increases in intensity. This is mostly a consequence of the behavior of the ionization equilibrium for the κ -distributions with temperature. The ionization peaks for both Si IV and O IV are shifted to lower temperatures, but the shift for Si IV is larger. In combination with the steeply increasing DEM with decreasing $\log(T)$, a stronger increase in the Si IV 1402.77 Å line compared to the O IV lines occurs, see Figure 13.

Indications of non-Maxwellian distributions in the TR were also obtained by Testa *et al.* (2014), who considered short-lived (tens of seconds) blueshifts in IRIS TR lines during the chromospheric evaporation process at the footpoints of Fe XVIII coronal loops that are heated by coronal nanoflares. One-dimensional hydrodynamic modeling was unable to reproduce the observations without the inclusion of a power-law beam of nonthermal electrons. The authors have found that a low-energy cutoff of about $E_c \approx 10$ keV, with total event energies of up to 10^{25} ergs, was able to reproduce the observed blueshifts in Si IV.

3.5. Diagnostics from Coronal Continuum and Lines

3.5.1. Constraints from Coronal X-ray Continuum Emission

The relative number of high-energy electrons in the solar corona can be constrained by using the X-ray continuum bremsstrahlung (free–free) emission. This is because the high-energy tails strongly increase the bremsstrahlung emission in X-rays (*e.g.*, Brown, 1971; Lin and Hudson, 1971; Holman *et al.*, 2003; Kontar *et al.*, 2011; Dudík *et al.*, 2012). Hannah *et al.* (2010) used quiet-Sun RHESSI (Lin *et al.*, 2002) observations to obtain upper limits on the number of energetic particles at energies higher than 3 keV that could be produced by coronal nanoflares (see also Klimchuk, 2006, 2015). In particular, it was found that the fraction of emission measures at temperatures above 5 MK (representing the hot second Maxwellian) must be lower than about 10^{-6} of the quiet-Sun corona, and that the possible power-law tails have to have an index higher than 5 for realistic low-energy cutoffs to be physically valid.

If the X-ray emission is instead interpreted as thin-target emission from an isothermal corona with a κ -distribution (rather than with several Maxwellians), constraints for the high-energy tail that is characteristic of a κ -distribution (see Figure 5 in Hannah *et al.*, 2010) can be obtained as a function of temperature. For example, at $T = 2$ MK, a $\kappa = 2$ distribution requires the emission measure to be less than 10^{43} cm $^{-3}$, but for $\kappa = 4$ the emission measure constraint is relaxed to about 10^{45} cm $^{-3}$. At higher T , the maximum emission measures decrease, with stronger decrease for higher κ values.

Since the non-Maxwellian distributions can be approximated by a sum of two or several Maxwellians (see Hahn and Savin, 2015, for the case of κ -distributions), the multi-Maxwellian interpretation of X-ray observations can also yield constraints on the number of high-energy particles. Such studies have been conducted by Ishikawa *et al.* (2014) and Hannah *et al.* (2016). Ishikawa *et al.* (2014) used observations with the *Focusing Optics X-ray Solar Imager* (FOXSI) using focusing X-ray optics mounted on a sounding rocket flight. The FOXSI instrument observed an active region for 6.5 minutes at energies greater than 4 keV. The observations were coordinated with *Hinode*/EIS (Culhane *et al.*, 2007) and *Hinode*/XRT (Golub *et al.*, 2007). The XRT instrument observed in multiple X-ray filters, while EIS observed multiple emission lines up to Fe XXIV, although only lines formed at temperatures of $\log(T/[K]) \lesssim 6.8$ in equilibrium, including Ca XVII, were detected. Using these coordinated observations, Ishikawa *et al.* (2014) derived the DEM for the active region that was observed. The DEM peak was located at $\log(T/[K]) \approx 6.3$ – 6.4 , with FOXSI 6–7 and 7–8 keV bins providing strong constraints at temperatures of $\log(T/[K]) \gtrsim 6.8$. Including these FOXSI data, the authors did not find evidence for a high-temperature component

with an emission measure greater than $3 \times 10^{44} \text{ cm}^{-3}$, which would arise from the DEM inversion of EIS and XRT data alone (see also Schmelz *et al.*, 2009).

Hannah *et al.* (2016) used the NuSTAR (Harrison *et al.*, 2013) direct-imaging observations of an active region at energies above 2 keV to obtain constraints on the high-temperature component and its emission measure. It was found that the observed spectra are well fit with an isothermal component with temperatures of 3.1–4.4 MK. Strong constraints were obtained on hotter sources, with their emission measure decreasing as T^{-8} . At 5 MK, the upper limit was found to be 10^{46} cm^{-3} , while at 12 MK, it was only 10^{43} cm^{-3} . No nonthermal contribution was detected, possibly because the exposure times were insufficient. Exposure times of longer duration will be possible with diminishing solar activity as Cycle 24 approaches its minimum.

3.5.2. Diagnostics from Coronal Lines

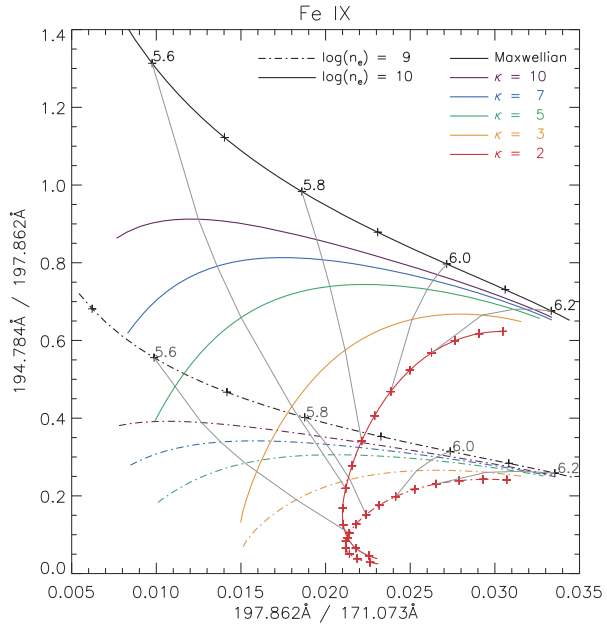
Signatures of non-Maxwellian distributions in coronal lines have been sought from spectrometric observations in the UV, EUV, and X-rays. Feldman, Landi, and Doschek (2007) studied the active region UV spectra of $1s2s^3S - 1s2p^3P$ lines of multiple He-like ions observed by SOHO/SUMER (Wilhelm *et al.*, 1995). These authors searched for signatures of a hot-electron population that was modeled by a second Maxwellian distribution. The ions formed at higher temperatures, such as Ne IX, Mg XI, and especially Si XIII, provided tight constraints on the number of high-energy electrons. In particular, the Si XIII lines were not detected. The authors thus found no indications that a second Maxwellian with temperature $\log(T \text{ [K]}) = 7.0$ would be required to explain the spectra. Instead, the spectra were consistent with multithermal plasma where the temperature of the second Maxwellian is at most $\log(T \text{ [K]}) = 6.5$ (Feldman, Landi, and Doschek, 2007, see Table 4 therein).

Ralchenko, Feldman, and Doschek (2007) investigated the quiet-Sun UV spectra of Si VIII–Si XII, Ar XI–Ar XIII, and Ca XIII–Ca XV ions observed by SUMER. These authors showed that these spectra are consistent with a bi-Maxwellian distribution, where the hot-temperature Maxwellian contains only a few percent of the particles. This fraction depended on the assumed temperature of this hot Maxwellian. It was at most 5–7% for the temperature of 300 eV (2.3 MK) and decreased to 1% for 1 keV (7.7 MK).

Systematic searches for signatures of the κ -distributions in the *Hinode*/EIS spectra were performed by Dzifčáková and Kulinová (2010) for Fe ions and by Mackovjak, Dzifčáková, and Dudík (2013) for other elements. A key finding was that diagnostics of κ are always coupled to diagnostics of T , so that at least two line ratio pairs (*i.e.*, at least three lines) are needed for each ion – see Figures 14 and 15. For the Fe ions, the diagnostics are complicated further by the strong density sensitivity of many of the Fe emission lines. Although it was found that many of the standard EIS density diagnostics (*e.g.*, Young *et al.*, 2009; Watanabe *et al.*, 2009; Del Zanna *et al.*, 2012) do not depend strongly on κ or T , the uncertainties on the density measurements are passed on to the κ determinations, leading to greater uncertainty in the derived values. Fe XVII was identified as the most useful Fe ion as the line ratios are insensitive to density, but the diagnostics were hampered by uncertainties in the atomic data.

Mackovjak, Dzifčáková, and Dudík (2013) determined that only Ca, Ni, S, and O of the non-Fe elements provide diagnostics of κ within the EIS wavelength range. Diagnostics involving lines from neighboring ionization stages were found to be the most sensitive. A key single-ion diagnostic was identified for O IV involving lines at 207.2 and 279.9 Å, but the former was found to be blended in EIS spectra. A κ -diagnostic belonging to S X was identified and applied to an off-limb dataset, but results were not conclusive because the lines were weak and possible contributions from multithermal structures.

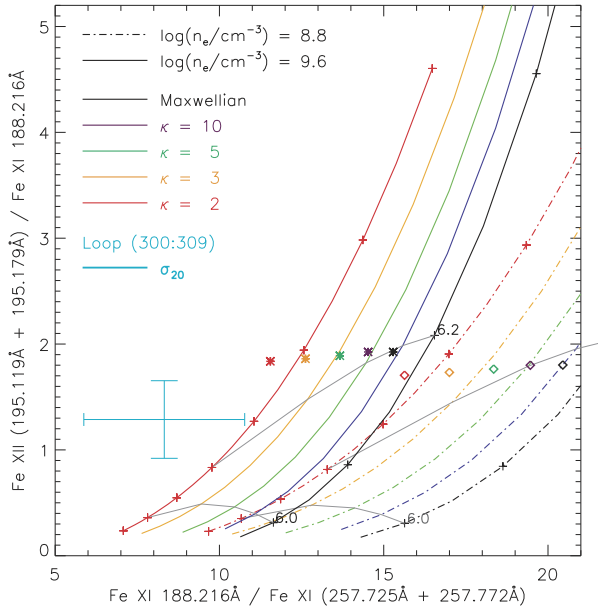
Figure 14 Theoretical ratio–ratio diagram for simultaneous diagnostics of T and κ using Fe IX EUV observations. Individual colors stand for different κ , while line styles denote n_e . The thin gray lines connect points with the same $\log(T [K])$. The wavelengths of the lines that constitute the intensity ratios are indicated at each axis. Credit: Dudík *et al.* (2014a), reproduced with permission © ESO.



An ongoing effort is underway to capitalize on state-of-the-art atomic data produced by the UK APAP team. Dudík *et al.* (2014a) used these data to identify a number of κ -diagnostics of Fe IX to Fe XIII over a wide wavelength region from the visible to soft X-rays. The authors stressed that accurate radiometric calibration and temperature measurements are critical for application of the diagnostics. Two particular diagnostics were highlighted: ratios formed from EUV allowed lines and visible forbidden lines, and Fe IX ratios involving the 197.86 Å emission line. For the former, the intensity ratios of the forbidden to EUV lines increase as κ decreases, with Fe X 6378.26 Å (the coronal red line) highlighted as an excellent line. Fe IX 197.86 Å is unusual in that it is a transition between two energy levels that are much higher in energy than other nearby Fe IX transitions, and examples of theoretical sensitivity curves as functions of κ , T , and n_e are shown in Figure 14. Although these lines are observed by EIS, the instrument sensitivity at 171.07 Å is extremely low, but one example for which the lines were well observed was presented by Del Zanna *et al.* (2014). The authors found that Fe IX intensities for a coronal loop leg anchored in a sunspot were consistent with the assumption of a Maxwellian electron distribution.

Since the single-ion Fe spectra typically do not have strong sensitivity to κ , lines from neighboring ionization stages have to be used. This has the advantage of increased sensitivity to κ since the ratio of two lines formed in neighboring ionization stages is dependent of κ through ionization equilibrium (Section 3.3.3). A disadvantage is, however, that such ratios can also become sensitive to departures from ionization equilibrium (see Section 5). Nevertheless, Dudík *et al.* (2015) used the Fe XI–Fe XII observations from *Hinode*/EIS to diagnose a $\kappa \lesssim 2$ distribution in a transient coronal loop. Many combinations of different Fe XI and Fe XII lines were used; all yielded consistent results. An example is shown in Figure 15. The revision of the EIS radiometric calibration performed earlier by Del Zanna (2013) was instrumental to these diagnostics. This is because the long-wavelength detector of EIS degraded differently from the short-wavelength detector, a fact noted and quantified by Del Zanna (2013). The κ diagnostics of Dudík *et al.* (2015) relied on using pairs of

Figure 15 Diagnostics of a κ -distribution in a transient loop observed by Dudík *et al.* (2015). The observed ratios of the EIS lines are indicated by the azure cross, while the theoretical ratios for individual κ are indicated by the different colors. The theoretical ratios are shown for the two densities of $\log(n_e [\text{cm}^{-3}]) = 8.8$ (dot-dashed) and 9.6 (full lines), respectively. Diamonds and asterisks represent the DEM-predicted line ratios. From Dudík *et al.* (2015), © AAS. Reproduced with permission.



Fe XI lines from two different EIS detectors, such as the Fe XI 188.2 Å/Fe XI 257.7 Å ratio (Figure 15). A significant problem in such diagnostics remains the high absolute calibration uncertainty, which is typically 20% for the coronal spectrometers (Lang *et al.*, 2000, 2006; Culhane *et al.*, 2007). This uncertainty can be comparable to the spread of the individual diagnostic curves (see Figure 15), which hampers the diagnostics of moderate κ values.

Furthermore, Dudík *et al.* (2015) found that the transient coronal loop they studied was not isothermal. Data from the *Atmospheric Imaging Assembly* (AIA; Lemen *et al.*, 2012; Boerner *et al.*, 2012) onboard the *Solar Dynamics Observatory* (SDO; Pesnell, Thompson, and Chamberlin, 2012) were used to derive the corresponding DEMs as a function of κ (Figure 16, see also Equation 9). When folded with the line contribution functions, it was found that the DEM-predicted ratios approach the observed ratios with decreasing κ (asterisks and diamonds in Figure 15). This confirmed the result of $\kappa \lesssim 2$ for this coronal loop.

We note that the low value of κ found could have significant consequences for coronal physics. For example, the total radiative losses from nonthermal plasmas can be modified by up to a factor of 2 compared to Maxwellian plasmas, with details depending on temperature and κ (Dudík *et al.*, 2011). Similarly, the nature of the AIA temperature responses changes with decreasing κ . Generally, the dominant changes in the AIA responses are given by the behavior of the ionization equilibrium. The coronal peaks of the AIA responses are typically broadened and shifted toward higher temperatures for low κ (Figure 17).

3.6. Differential Emission Measures

Since the non-Maxwellian distributions can be approximated by a sum of multiple Maxwellians, analyses of coronal observations involving calculation of DEM (Equation 9), which consists of contributions from several Maxwellians, could in principle yield different results if non-Maxwellian distributions were used instead. Namely, the resulting DEM can depend on the value of κ , which can be either assumed or independently diagnosed (see

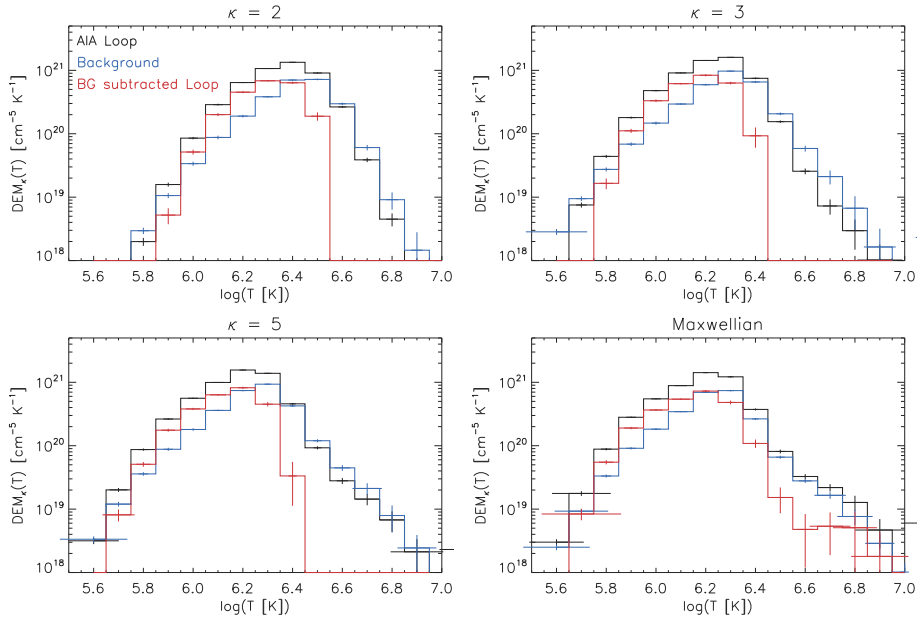
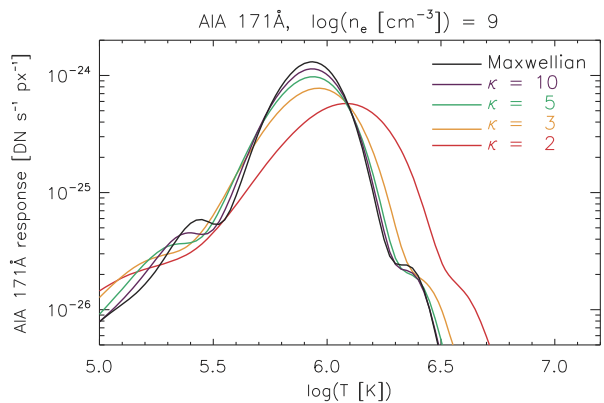


Figure 16 Behavior of the $DEM_{\kappa}(T)$ for different $\kappa = 2, 3, 5$, and the Maxwellian distribution. The DEMs are derived from AIA data. Black lines represent the original AIA data at the position of the transient loop. Blue lines stand for the neighboring background, while the red line denotes the background-subtracted DEMs for the transient loop. Horizontal and vertical error bars are shown at each temperature bin. From Dudík et al. (2015). © AAS. Reproduced with permission.

Figure 17 Example of the behavior of the AIA temperature responses with κ . The AIA 171 Å response is shifted toward higher temperatures with decreasing κ . From Džifčáková et al. (2015). © AAS. Reproduced with permission.



Section 3.5). Mackovjak, Džifčáková, and Dudík (2014) studied quiet-Sun Fe VIII–Fe XV spectra as well as active region spectra including several ions of Fe, Si, S, Ca, and Ar. These authors showed that in the case of the quiet Sun, the EM-loci plots (consisting of multiple $I_{ji}/G_{X,ji}(T, n_e, \kappa)$ curves for each observed line ji , see, e.g., Strong, 1978; Veck et al., 1984; Del Zanna and Mason, 2003) appear less multithermal, as the corresponding $I_{ji}/G_{X,ji}(T, n_e, \kappa)$ curves move toward a common isothermal crossing-point for $\kappa = 2$. Since these curves constitute an upper bound on the corresponding DEM_{κ} , the resulting DEM_{κ} are also less strongly multithermal. We note that the term “multithermal” for the

case of κ -distributions refers to $\text{DEM}_\kappa(T)$ having contributions from more than one temperature bin (Mackovjak, Dzifčáková, and Dudík, 2014).

In contrast to this, the degree of multithermality in the cores of active regions was found to be the same for all κ . The DEMs were only shifted toward higher T as a result of the behavior of the ionization equilibrium. This is of importance since in active region cores, the DEM slope at temperatures lower than its peak are thought to provide constraints on the recurrence frequency of the coronal nanoflares (*e.g.*, Viall and Klimchuk, 2011; Bradshaw, Klimchuk, and Reep, 2012; Warren, Winebarger, and Brooks, 2012; Winebarger, 2012; Cargill, 2014; Del Zanna *et al.*, 2015b). Since the low-temperature slope of the DEM_κ does not change with κ , the constraints on nanoflare timescales derived from observations do not change with respect to the relative number of accelerated particles (*i.e.*, different κ) that are present in the active region corona.

Examples of the effect of different κ values on the shapes of derived DEM_κ curves (from Dudík *et al.*, 2015) are shown in Figure 16. It can be seen that the Maxwellian DEMs peak at $\log(T \text{ [K]}) = 6.2$, with the peaks shifting to higher temperatures with higher κ value: the $\kappa = 2$ DEM peaking at $\log(T \text{ [K]}) = 6.4$.

4. Flare X-ray Emission

Solar flares are characterized by a rapid increase in X-ray emission over short timescales. It is thought that this occurs as a consequence of magnetic energy release involving magnetic reconnection (*e.g.*, Priest and Forbes, 2000; Zweibel and Yamada, 2009), which accelerates particles and heats the plasma. Soft X-ray emission is mostly emitted by flare loops during the peak and gradual phases, while hard X-ray emission is present during the impulsive phase. Accelerated particles during the impulsive phase are routinely detected from hard X-ray bremsstrahlung (free–free) emission (Section 4.1). These accelerated particles should therefore also have an effect on the EUV and X-ray line emission originating in the flaring corona (Sections 4.2 and 4.3).

4.1. Hard X-ray Continuum

We start with a review of hard X-ray (HXR) signatures that indicate nonequilibrium processes in the solar corona. Although much is already known from previous observations, we focus here on the latest HXR mission, the *Reuven Ramaty High-Energy Solar Spectroscopic Imager* (RHESSI Lin *et al.*, 2002), which achieved spatial and spectral resolutions much higher than those of earlier solar HXR missions.⁷ Various new features of solar flare X-rays have been discovered by RHESSI, and they have been reviewed elsewhere (*e.g.*, Benz, 2008; Krucker and Lin, 2008; Fletcher *et al.*, 2011; Hannah *et al.*, 2011; Kontar *et al.*, 2011; Lin, 2011; Vilmer, MacKinnon, and Hurford, 2011; White *et al.*, 2011; Zharkova *et al.*, 2011).

We note that strong HXR emission is normally found at the footpoints of flare loops. These footpoint sources are much more intense than those in the corona (*e.g.*, Duijveman, Hoyng, and Machado, 1982; Sakao, 1994; Saint-Hilaire, Krucker, and Lin, 2008). However, the coronal sources have received considerable attention recently because of their proximity to the possible reconnection region. In the following subsections, we briefly review observations and interpretations of coronal hard X-ray sources.

⁷http://hesperia.gsfc.nasa.gov/rhessi3/news-and-resources/results/top_rhessi_accomp.html.

4.1.1. Overview of Hard X-ray Coronal Observations

Solar flares produce nonthermal electrons with energies of up to several tens of MeV. While magnetic reconnection has been considered as a key mechanism of energy release during solar flares (e.g., Masuda *et al.*, 1994; Tsuneta, 1996; Sui and Holman, 2003), it still remains unclear how the requisite production of nonthermal electrons can be explained by magnetic reconnection. *Yohkoh*'s discovery of a coronal HXR source that appeared to float above the tops of flaring loops indicates that electron energization (*i.e.*, heating and/or production of a nonthermal component) takes place in the corona (e.g., Masuda *et al.*, 1994). Since then, various theoretical ideas have been proposed to explain energetic electrons associated with the 'above-the-loop-top' HXR source. Some of the key theories proposed are the fast-mode termination shocks (e.g., Tsuneta and Naito, 1998; Guo and Giacalone, 2012; Li *et al.*, 2013; Nishizuka and Shibata, 2013), turbulence (e.g., Miller *et al.*, 1997; Bian *et al.*, 2014), collapsing magnetic traps (e.g., Somov and Kosugi, 1997; Karlický and Kosugi, 2004; Bogachev and Somov, 2005; Giuliani, Neukirch, and Wood, 2005), and magnetic islands (e.g., Drake *et al.*, 2006; Oka *et al.*, 2010; Bian and Kontar, 2013). Many of the recent theories use more than one of these mechanisms. For more details, we refer to more comprehensive reviews by Miller *et al.* (1997), and Zharkova *et al.* (2011), for example.

RHESSI established that during flares, a nonthermal power-law tail often exists in the energy spectrum of a coronal HXR source (e.g., Lin *et al.*, 2003; Veronig and Brown, 2004; Battaglia and Benz, 2006; Krucker *et al.*, 2008; Kašparová and Karlický, 2009; Simões and Kontar, 2013), in particular in the above-the-loop-top source (e.g., Krucker *et al.*, 2010; Ishikawa *et al.*, 2011; Chen and Petrosian, 2012; Oka *et al.*, 2013, 2015; Krucker and Battaglia, 2014). This clearly indicates that time-dependent and nonequilibrium processes exist in the solar corona during flares. The measured spectral slopes of the high-energy tail as well as the inferred energy partition between thermal and nonthermal electrons are expected to provide key information on the possible nonequilibrium processes and to constrain theories of electron acceleration. However, the nonthermal and thermal emissions generally originate from different sources, *i.e.*, above-the-loop-top sources and coronal flare loops, and therefore the combined diagnostic capability can be applied for the rare cases where both sets of emissions originate from the same volume.

4.1.2. Electron Energy Partition and the κ -Distributions

In two particular flares with very intense above-the-loop-top sources, it was shown that all electrons are accelerated in a bulk energization process to form a power law with no thermal pre-flare plasma left (Krucker *et al.*, 2010; Krucker and Battaglia, 2014). This requires an extremely efficient process for the formation of the nonthermal electron distribution. However, the nonthermal component is significantly weaker than this case in most flares, and for some events the nonthermal component is even undetected. Some studies have reported a super-hot ($\gtrsim 30$ MK) thermal source in addition to the hot ($\lesssim 30$ MK) loop-top source (Caspi and Lin, 2010; Caspi, Krucker, and Lin, 2014; Longcope *et al.*, 2010), suggesting a need for strong heating in addition to acceleration to nonthermal energies.

A caveat is that the main thermal flare loop is generally so bright that instrumental limitations are masking the above-the-loop-top spectrum in the lower-energy ($\lesssim 15$ keV) range. Furthermore, the above-the-loop-top source is generally faint and its spectrum reaches the detection limits at higher energies (e.g., $\gtrsim 80$ keV in the case of the fortuitously bright above-the-loop-top source, but more generally only up to ≈ 30 keV). Hence, the above-the-loop-top source is only observed over a rather limited energy range (*i.e.*, 15–80 keV),

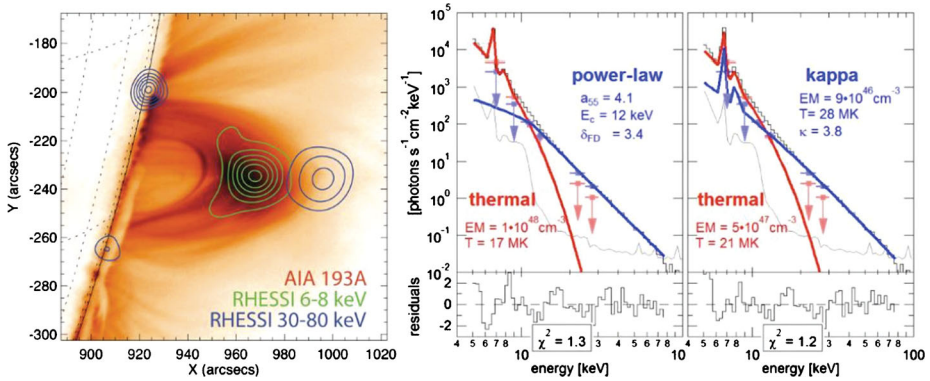


Figure 18 Left: X-ray (contours) and EUV (background) images of the limb flare of SOL2012-07-19T05:58. Lower energy thermal X-rays come from the loop-top region (green contours), whereas higher energy non-thermal X-rays come from the footpoint as well as ‘above-the-loop-top’ regions (blue contours). From Krucker and Battaglia (2014). Center: The combined data from both the loop-top and above-the-loop-top regions of another flare SOL2007-12-31T01:11 (histogram) fitted with a thermal and a power-law distribution (red and blue curves, respectively). Right: The same, combined data are now fitted with a thermal and a κ -distribution. From Oka *et al.* (2013). © AAS. Reproduced with permission.

and the observations therefore only provide limited diagnostic power to distinguish different interpretations.

Recently, κ -distributions have been proposed as yet another way of interpreting the spectral form in the above-the-loop-top region (Kašparová and Karlický, 2009; Oka *et al.*, 2013, 2015). Oka *et al.* (2013, 2015) argued that there should always be a thermal core component because of thermalization (in the lower-energy range) by Coulomb collisions and/or wave-particle interactions (see also Holman *et al.*, 2011). By varying the index κ , the κ -distribution can, in fact, represent not only cases with negligible nonthermal component (including super-hot cases), but also cases with a saturated nonthermal component (with no spectral break between the thermal and nonthermal components). We note that the spatial and temporal scales of kinetic processes are much smaller than those of *RHESSI* observations. Thus, it was argued that it is reasonable to assume a simple functional form for the lower-energy ($\lesssim 15$ keV) range rather than complex, nonthermal, or non-stationary spectral forms such as flat-top, bi-Maxwellian, bump, and beam. The thermal Maxwellian and κ -distributions are simple in the sense that they represent the state of maximum Boltzmann–Gibbs and Tsallis entropies, respectively (*e.g.*, Livadiotis and McComas, 2009). Based on the analysis of five events using the κ -distribution model, it was suggested that the lowest value of κ is ~ 4 and that the corresponding nonthermal fractions of electron density and energy are $\sim 20\%$ and $\sim 50\%$, respectively. The observations can be considered as bulk energization with all electrons being energized because the thermal part of the κ -distribution is much hotter than the pre-flare plasma.

4.1.3. Event-to-Event Variations of the Nonthermal Tail

Despite the difference in the interpretation (or extrapolated form) of the lower-energy range, at higher energy the nonthermal tail in the coronal X-ray source seems to be a generic feature. From a statistical analysis of 55 coronal source events during flares, it was reported that the power-law indices of photon spectra fall between ~ 4 and ~ 6 (Krucker and Lin, 2008). We note that coronal sources are often interpreted by the thin-target model and the

range corresponds to the power-law index $\delta = 3-5$ of the electron flux distribution under the assumption of the thin-target model.⁸

On the other hand, flare events with a nonthermal coronal X-ray source but no clear emission from footpoints have been reported (Veronig and Brown, 2004; Lee *et al.*, 2013). It has been argued that the column densities of the nonthermal coronal source were high and that energetic electrons must have lost their energies before reaching the footpoints. Then, the thick-target model can be applied to the coronal source of these events. The derived spectral index δ was between ~ 6 and ~ 7 , indicating very soft (steep) electron spectra.⁹

A variation in power-law index was also discussed for the above-the-loop-top source events that were analyzed with the κ -distribution (Oka *et al.*, 2015). It was reported that the κ values obtained were between ~ 4 and ~ 14 (or δ between ~ 4 and ~ 14),¹⁰ indicating a very wide range of power-law spectral index. A higher value of κ indicates that the spectrum is closer to Maxwellian. Galloway *et al.* (2010) showed that the nonthermal high-energy tail of a κ -like distribution can be thermalized into a Maxwellian over a timescale of $100-1000\tau_{\text{coll}}$, where τ_{coll} is the electron–electron collision time of the core particles, and it can be ~ 0.1 s in a plasma with 30 MK temperature and 10^9 cm⁻³ density. Thus, it was speculated that while electron acceleration may be achieved primarily by collisionless magnetic reconnection, the above-the-loop-top source density determines the electron energy partition and the associated spectral slope of the source spectra.

4.1.4. Confinement of Electrons

A standard scenario for footpoint emission is that electrons accelerated in the corona precipitate along flare loops and lose the bulk of their energy through electron–ion bremsstrahlung X-ray emission in the lower solar atmosphere. It has been reported that the measured differences between the coronal (thin-target) and footpoint (thick-target) power-law indices are consistent with this scenario (*e.g.*, Battaglia and Benz, 2006; Ishikawa *et al.*, 2011).

A more recent quantitative analysis indicated that there is a sufficient number of accelerated electrons in the coronal source to suggest not only precipitation into footpoint sources, but also that a fraction of the population is trapped within the source (Simões and Kontar, 2013). The observations of the above-the-loop-top source over a time period longer than the electron transit time across the source indicate by themselves that electrons are trapped within the source region.

From a theoretical point of view, Minoshima *et al.* (2011) developed and solved a drift-kinetic Fokker–Planck model to quantitatively discuss the importance of pitch-angle scattering for trapping of electrons within the above-the-loop-top region. Kontar *et al.* (2014) also used a Fokker–Planck approach to deduce the mean free paths of electrons trapped in a coronal source. On the other hand, particle-in-cell (PIC) simulations of energetic electron transport showed that a localized electrostatic potential or ‘double layer’ is formed and that it inhibits further transport of energetic electrons (Li, Drake, and Swisdak, 2012, 2013, 2014).

⁸The power-law index γ_{thin} of a thin-target photon spectrum is related to the power-law index δ of electron flux distribution and the power-law index δ' of electron density distribution by $\gamma_{\text{thin}} = \delta + 1$ and $\gamma_{\text{thin}} = \delta' + 0.5$, respectively (*e.g.*, Brown, 1971; Tandberg-Hanssen and Emslie, 1988).

⁹Here, the power-law index γ_{thick} of a uniform thick-target photon spectrum is related to the power-law index δ of the electron flux distribution and the power-law index δ' of electron density distribution by $\gamma_{\text{thick}} = \delta - 1$ and $\gamma_{\text{thick}} = \delta' - 1.5$, respectively (*e.g.*, Holman *et al.*, 2011).

¹⁰Because the phase space density of the κ -distribution has the form $f(v) \propto v^{-2(\kappa+1)}$, the corresponding power indices of the electron flux distributions are $\delta \sim 4$ and ~ 14 (or ~ 4.5 and ~ 14.5 for the density distribution).

Interestingly, Bian *et al.* (2014) proposed that a local stochastic acceleration of electrons within the X-ray source is still possible because a collisional loss can be taken into account instead of escape from the source region to explain the power-law formation. The authors furthermore derived the κ -distribution analytically based on the balance between the stochastic acceleration and the collisional loss.

To understand how the above-mentioned physics (scattering, double-layer, collisional loss, *etc.*) are related to each other and how they are related to the dynamics of flares, including magnetic reconnection, it is essential to have larger-scale kinetic simulations. It is also desirable to have more detailed observations of the above-the-loop-top source.

4.2. Mean Electron Fluxes from RHESSI and AIA Observations

Since 2010, a number of solar flares have been observed by both RHESSI and SDO/AIA. While RHESSI provides direct information on the high-energy part of the electron distribution function above ≈ 3 keV, the low-energy part up to about 1–1.5 keV can be constrained from AIA observations following the approach of Battaglia and Kontar (2013). These authors considered the electron mean flux spectrum $\langle n_e V F(E) \rangle$

$$\begin{aligned} \langle n_e V F(E) \rangle &= \int_V n_e(r) F(E, r) dV = \int_T n_e^2(r) f(E, r) \frac{dV}{dT} dT \\ &= \int_T \xi_f(T) f(E, r) dT, \end{aligned} \quad (12)$$

where $V = A \int dl$ is the emitting volume, A is the emitting plane-of-sky area on the Sun, $F(E) = n_e f(E)$, $\xi_f(T) = \int n_e^2 dV/dT = AC \int n_e n_H dl/dT = AC \text{DEM}_f(T)$ is the volumetric differential emission measure (*cf.*, Sections 3.1 and 3.6), and $C = n_e/n_H = 1/0.83$ for coronal and flare conditions.

Battaglia and Kontar (2013) considered $f(E)$ to be a Maxwellian and/or power-law distribution. They used the Maxwellian AIA responses (*cf.*, Section 3.5) to calculate the $\xi_f(T)$ functions and the corresponding mean electron flux $\langle n_e V F \rangle$ for the loop source from RHESSI and AIA separately. This was done for two events, the C4.1-class event SOL2010-08-14T10:05, and the well-known M7.7-class SOL2012-07-19T05:58 (see also, *e.g.*, Figure 18 (left) and Krucker and Battaglia, 2014; Sun, Cheng, and Ding, 2014; Oka *et al.*, 2015). Thermal and power-law fits to the RHESSI data were performed and extrapolated to lower energies (up to 2 keV) corresponding to AIA observations. For both flares the RHESSI fits overpredicted the AIA observations by a factor of at least two for all regions that were studied. For the above-the-loop-top source in the M7.7 flare, the overprediction was more than an order of magnitude. Conversely, the AIA DEMs, derived using the regularized inversion method of Hannah and Kontar (2012, 2013), and the corresponding $\langle n_e V F \rangle$ values were consistent with a hot isothermal plasma, but only up to energies of 1 and 0.5 keV for the C4.1 and M7.7 flares, respectively. Above these energies, excess flux above the isothermal $\langle n_e V F \rangle$ level was present. The authors suggested that the derived mean electron flux spectrum could be described by a combination of a Maxwellian core, secondary halo, and a nonthermal tail similar to the situation observed in the solar wind.

The analysis was applied to several above-the-loop-top sources by Oka *et al.* (2015). These authors fitted the observed RHESSI high-energy tails using several different components, including a power law, thermal and power-law, and a κ -distribution. The power-law fits overpredicted the AIA $\langle n_e V F \rangle$ values by several orders of magnitude (Oka *et al.*, 2015, Figure 5), while the thermal and power-law fits underpredicted them by at least an order of

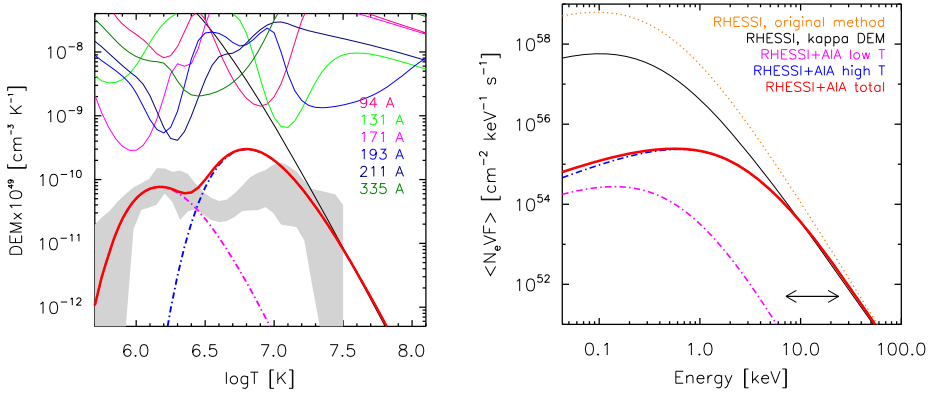


Figure 19 Comparison of the DEMs (left) and the electron mean flux spectrum (right) from analysis of RHESSI and AIA data. The κ -fit to the RHESSI data is shown as the thin dotted orange line, while the $\xi_\kappa(T)$ and the corresponding $\langle n_e V F \rangle$ is shown by the thin black line in the left panel. The $\xi_{\text{AIA}}(T)$ is denoted by the gray shaded area in the left panel. It consists of two components, $\xi^{\text{hot}}(T)$ and $\xi^{\text{cold}}(T)$, shown in blue and purple dash-dotted lines, respectively. From Battaglia, Motorina, and Kontar (2015), © AAS. Reproduced with permission.

magnitude. A caveat is that for the above-the-loop-top sources, the RHESSI thermal components can be beyond the temperature sensitivity of AIA. Thus, the AIA data represent only an upper limit because of the possible contribution from unresolved cooler plasma at temperatures of ≈ 10 MK or lower. Therefore, the thermal plus power-law fit to the RHESSI data, which underpredicts the AIA $\langle n_e V F \rangle$, is not ruled out by the constraints derived from AIA. Oka *et al.* (2015) pointed out, however, that such fits returned unreasonable fit parameters because of an artifact: a sharp lower-energy cutoff. In contrast to this, the third class of fit used, the κ -distribution, fits the high-energy tail observed by RHESSI well. In addition, the κ -distribution is not ruled out by the mean electron flux $\langle n_e V F \rangle$ derived from AIA (Oka *et al.*, 2015, Figure 5) and dispenses with the need of an artificial low-energy cutoff.

We note here that in these articles, the $\langle n_e V F \rangle$ values were derived under the assumption that $f(E)$ is a Maxwellian distribution. Battaglia, Motorina, and Kontar (2015) remedied this by using a κ -distribution instead (see Section 2 therein). The RHESSI 7–24 keV data for the loop source in the confined SOL2010-08-14T10:05 C4.1 event (studied previously by Battaglia and Kontar, 2013) were fit with a κ -distribution, yielding $\kappa = 4.1 \pm 0.1$, and also with a $\xi_\kappa(T)$, yielding $\kappa = 3.6 \pm 0.1$. This $\xi_\kappa(T)$ function is shown by a full black line in Figure 19, while the fitting with a κ -distribution is shown by the orange dotted line. The fitting interval of 7–24 keV is shown by the horizontal arrow in the right panel of Figure 19. The regularized inversion DEMs obtained from the AIA data alone, $\xi_{\text{AIA}}(T)$, are shown by the gray area in the left panel, denoting the uncertainties in the resulting DEMs. It contains a dip at $\log(T [\text{K}]) \approx 6.6$, a consequence of the lower AIA sensitivities at these temperatures. It is again seen that the $\xi_\kappa(T)$ derived from RHESSI alone overpredicts the $\xi_{\text{AIA}}(T)$ at temperatures $\log(T [\text{K}]) < 7.5$ and the $\langle n_e V F \rangle$ fluxes at energies below about 10 keV (Figure 19).

In addition to this, Battaglia, Motorina, and Kontar (2015) found that the combined RHESSI and AIA data together can be fit by using a two-component $\xi_\kappa(T)$ function, consisting of $\xi_\kappa^{\text{hot}}(T)$ and $\xi_\kappa^{\text{cold}}(T)$. These two components are shown in Figure 19 by purple and blue dash-dotted curves. Since the peak of the $\xi_\kappa^{\text{cold}}(T)$ function is located at

$\log(T [\text{K}]) = 6.2$, it probably represents the foreground or background emission from the non-flaring corona. Therefore, the flare emission is likely well-represented by a single $\xi_{\kappa}^{\text{hot}}(T)$ function peaking at about 11 MK. The values of κ obtained were $\kappa^{\text{hot}} = 3.9_{-0.1}^{+0.2}$ and $\kappa^{\text{cold}} = 4.5_{-1}^{+4}$, in broad agreement with those derived from RHESSI fitting alone.

These analyses show that taking the wider observed energy range into account provides tighter constraints on the mean electron flux spectrum in the flare plasma. Additionally, when only a limited energy range is approximated (*e.g.*, only RHESSI observations above several tens of keV), it could in principle lead to misleading results on the nature of the nonthermal component in the plasma. We note that these analyses used the AIA responses calculated for the Maxwellian distribution and that the κ -distributions can influence them (Section 3.5). This may be of potential importance mainly for low κ since the corresponding DEMs derived from AIA under the assumption of a κ -distribution can differ from the Maxwellian distribution, see Section 3.6.

Finally, we note that an independent indications of κ -distributions in solar flares were obtained by Jeffrey, Fletcher, and Labrosse (2016, 2017) by analyzing the *Hinode*/EIS Fe XXVI and Fe XXIII line profiles observed during flares. After accounting for the instrumental profile (via convolution), the line profiles were found to be consistent with κ values as low as 2, although higher values of 3–6 were found for Fe XXIII.

4.3. X-ray Line Spectra

In this section, we discuss the non-Maxwellian effects on the flare X-ray line spectra, especially those formed in the 1–7 Å range. Since these wavelengths correspond to ≈ 12.4 and 1.8 keV, respectively, and the lines are excited by electrons of these or higher energies, their intensities can be directly influenced by high-energy tails that are observed using bremsstrahlung emission (Section 4.1), but also other non-Maxwellian effects (Section 4.3.2).

4.3.1. Overview of the X-ray Line Observations at 1–7 Å

The diagnostic power and scientific value of high-resolution X-ray line spectra emitted by hot 1–30 MK astrophysical plasmas have been well established over the past half-century. Here, we briefly discuss the spectra observed in the 1–7 Å range during solar flares. These spectra are characterized by a multitude of emission lines, including (1) allowed lines of H-like and He-like ions from Si to Ni, (2) dielectronic satellite lines located longward of the respective allowed lines of the parent ion (Sections 4.3.1 and 4.3.2), (3) inner-shell excitation lines, (4) lines formed from excitation levels corresponding to high principal quantum number (Section 4.3.3), and (5) free–free and free–bound continua (see, *e.g.*, Phillips, Feldman, and Landi, 2008, Chapter 6.2 therein). A brief description of important instruments that observed or will be observing the lines in these short-wavelength bands is discussed below and in Section 6. We also briefly describe below two of the main nonequilibrium diagnostics provided in this wavelength range, *i.e.*, the possibility of searching for departures from Maxwellian distributions (Section 4.3.2) and from ionization equilibrium (Section 5.4). Both cases rely on observations of the satellite lines, formed by electrons that are dielectronically captured by ions (see Section 3.3.2 and Gabriel 1972).

Although there is no X-ray spectrometer observing the 1–7 Å solar flare emission lines at present, several of these instruments have been flown in the past. The first of these, flown in the 1960s and 1970s, observed the prominent spectral lines of H-like and He-like ions. The next generation of spectrometers in the late 1970s and early 1980s was flown on the

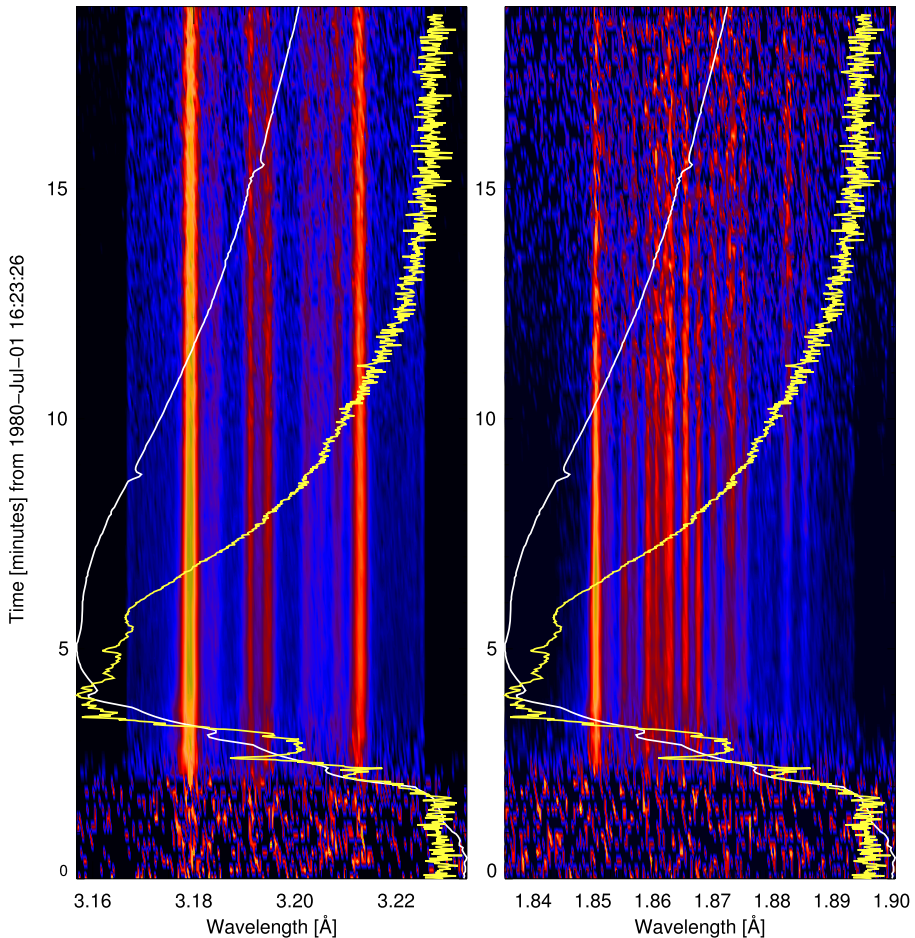
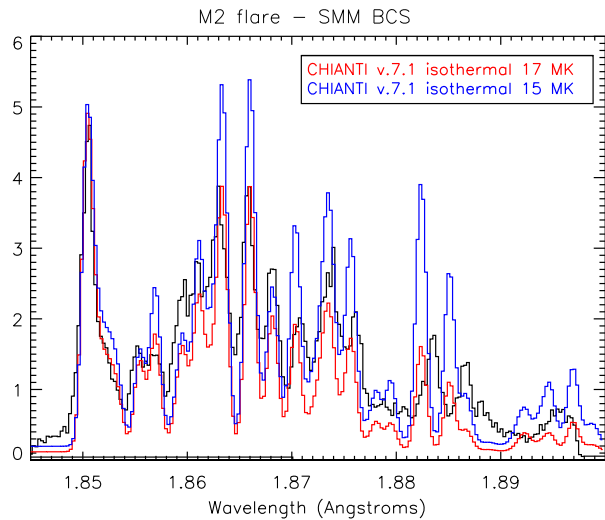


Figure 20 Time stack of normalized spectra for the flare SOL1980-07-01T16:29 observed by the BCS, a part of XRP on SMM. Left: Spectral region of Ca XIX He-like triplet (Channel 1). In the upper part, the line designations are adopted from Gabriel (1972). Right: Spectral region of the Fe XXV He-like triplet including lines formed in lower ionization stages (see above the stack). In both panels, the light curve of the hard X-ray emission as observed by the HXRBS full-Sun spectrometer in the range 20–500 keV is drawn (yellow), as well as the soft X-ray light curve measured by GOES in the 1–8 Å band (white). The Ca and Fe He-like lines are both pronounced from the very beginning of the impulsive flare for this event. More than 100 flare spectral cubes are available for the analysis from the SMM BCS data archive.

U.S. Navy *P78-1* (SOLFLEX, SOLEX; Doschek, Kreplin, and Feldman, 1979), the NASA *Solar Maximum Mission X-ray Polychromator* (XRP; Acton *et al.*, 1980, *cf.*, Figure 20), and the Japanese *Hinotori* spacecraft (SOX1, SOX2; Tanaka *et al.*, 1982). These allowed the time evolution of temperatures, emission measures, flows, and turbulent velocities to be studied and related to current theories of solar flares. This was later extended with the *Bragg Crystal Spectrometer* (BCS; Culhane *et al.*, 1991) onboard the Japanese *Yohkoh* spacecraft. The BCS had a collimator field of view of about $6' \times 6'$ and obtained spectra with eight proportional counters in the 1.7–3.2 Å range, with a resolving power of about 10^4 . Figure 21 shows as an example a BCS spectrum obtained in the Fe XXV channel during the peak phase

Figure 21 SMM/BCS spectrum during a solar flare (black) with superimposed CHIANTI simulated spectra at two slightly different temperatures (blue and red).



of a solar flare, with superimposed theoretical spectra obtained from CHIANTI v.7.1 (Landi *et al.*, 2013) assuming two isothermal distributions with temperatures of $T = 15$ and 17 MK, respectively. The figure shows how sensitive the intensities of individual lines are to the electron temperature. The spectral lines near the Fe XXV line are also sensitive to departures from Maxwellian distributions and ionization equilibrium.

At longer wavelengths above 3.4 \AA , the X-ray spectra were obtained during 2001–2003 by the RESIK bent-crystal spectrometer (*Rentgenovskij Spectrometer s Izognutymi Kristallami*; Sylwester *et al.*, 2005) onboard the CORONAS-F satellite. This spectrometer collected spectra of more than 200 flares in four bands that nearly continuously cover the $3.4\text{--}6.1 \text{ \AA}$ range.¹¹ The RESIK spectra include a number of strong emission lines due to transitions $1s^2 - 1s(np)$ and $1s - np$ in He-like and H-like ions, denoted by letters w and Ly , respectively. Sample RESIK spectra in four energy channels are shown in Figure 22 together with the identification of the main spectral features for the rise and decay phase of the C5.8 flare SOL2003-02-22T09:29. RESIK channels 1, 2, and 3 are dominated by K XVIII, Ar XVII triplets, and S XVI $Ly\alpha$ lines, respectively. Channel 4 contains strong S XV and Si XIII–Si XIV allowed lines, as well as a clearly resolved number of dielectronic satellite lines of Si XII.

4.3.2. Non-Maxwellian Analysis of X-ray Line Spectra

Gabriel and Phillips (1979) developed a technique for determining the departure of the electron velocity distribution from a Maxwellian. A departure from a Maxwellian distribution can be detected because dielectronic recombination lines are produced only by the electrons with a given energy, *i.e.*, by electrons whose energy is exactly equal to the energy difference between the initial and excited states of the dielectronic capture process (equal to within the energy width of the excited state, determined by its natural lifetime). In contrast to this, allowed lines formed by electron impact excitation can be produced by any electron with an energy greater than the threshold energy of the excited state.

¹¹Reduced level-2 spectra containing absolute fluxes for 101 flares and active region plasma is accessible at www.cbk.pan.wroc.pl/experiments/resik/RESIK_Level2/index.html.

Figure 22 RESIK spectra for the rise and decay phases of the C5.8 SOL2003-02-22T09:29 flare, obtained during 09:27:30–09:29:00 UT (top) and 09:30:00–09:34:00 UT (bottom). Colors denote individual spectral bands. Prominent spectral features are identified. Dotted lines connect maxima of H and He resonance transitions in S and Si.

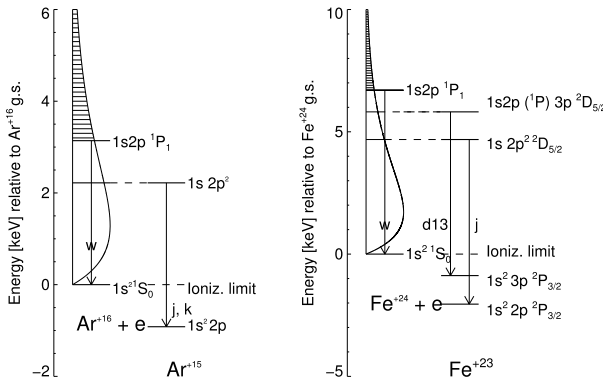
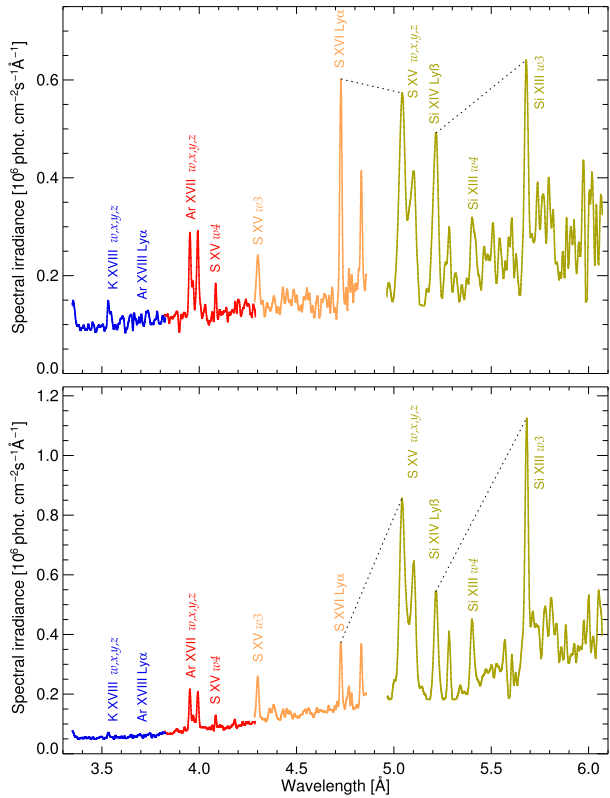
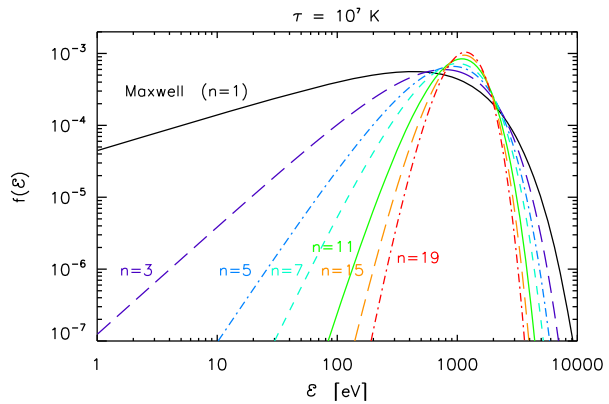


Figure 23 Diagram of energy levels for the argon and iron ions: Ar^{+15} (left) and Fe^{+23} . The free electron exciting satellite lines j and $d13 + d15$ are assumed to have a Maxwell–Boltzmann distribution with $T_e = 15$ MK (Ar) and $T_e = 20$ MK (Fe). The line w is excited by electrons with energies above 3.14 keV (Ar) and 6.7 keV (thatched areas) respectively, the Fe XXIV satellite line j is excited by monoenergetic electrons with $E = 4.69$ keV, and the Fe XXIV satellite $d13$ is excited by monoenergetic electrons with $E = 5.82$ keV.

An energy diagram showing which parts of the assumed Maxwellian electron population contribute to the excitation of the parent allowed w lines as well as dielectronic satellite lines (j , k , $d13$) is displayed in Figure 23 for the He-like Ar XVII and Fe XXV ions. It is clearly

Figure 24 Shape of the Maxwellian ($n = 1$) and n -distributions with $n = 3, 5, 7, 11, 15,$ and 19 . The distributions have the same mean energy corresponding to $\tau = 10^7$ K. The deviation from the Maxwellian distribution rises with the value of n .



seen that by increasing the temperature, the number of electrons contributing to the parent line intensity changes relative to the number of electrons at the resonance, which contribute to the satellite line intensity. The dependence of the satellite to the resonance-line intensity ratio scales approximately as $1/T$. Similarly, the intensities of allowed lines are increased when power-law tails (e.g., κ -distributions) are present. During flares, such power-law tails are observed by RHESSI at energies of $\gtrsim 4$ keV (see Section 4.1). The increase in intensities of the allowed lines arises because the enhanced number of high-energy particles at these energies increase the corresponding excitation rate. In contrast to this, the dielectronic lines that are formed at lower energies are not affected by this high-energy tail. Therefore, the ratio of intensities of the dielectronic to satellite lines will decrease (Gabriel and Phillips, 1979).

In order to apply this technique, very high-resolution spectrometers that resolve the dielectronic satellite lines are needed. The technique was successfully applied to laboratory plasmas (see, e.g., Bartiromo, Bombarda, and Giannella, 1985). In solar spectra, these satellite lines are hard to resolve. However, Seely, Feldman, and Doschek (1987) provided a nonthermal analysis of X-ray line spectra of three flares based on this technique, finding that the dielectronic satellite lines were increased during the early phase of a flare. This is in contrast to the prediction of what occurs in the presence of a high-energy tail or HXR burst, which were observed independently. The increase of the dielectronic satellites could also not be explained by multithermal plasma.

Instead, the observations were explained by the presence of a non-Maxwellian electron energy distribution that was more strongly peaked than the Maxwellian distribution, if the peak occurs at energies corresponding to formation of dielectronic satellite lines. It was found that such distributions occur in addition to the high-energy tails (see below) and that the occurrence of this distribution coincided with the occurrence of hard X-ray bursts.

These peaked electron distributions (Figure 24) have a different shape than a Maxwellian or a κ -distribution, and no high-energy tail. Dzifčáková (1998) modified the expression for the non-Maxwellian distribution used by Seely, Feldman, and Doschek (1987) to the n -distribution

$$f_n(E) dE = B_n \frac{2}{k_B T \sqrt{\pi}} \left(\frac{E}{k_B T} \right)^{n/2} \exp\left(-\frac{E}{k_B T} \right) dE, \tag{13}$$

where B_n is the normalization constant, and n and T are free parameters. The mean energy of the n -distribution is $\langle E \rangle = \frac{n+2}{2} k_B T = \frac{3}{2} k \tau$, where τ is the pseudo-temperature defined

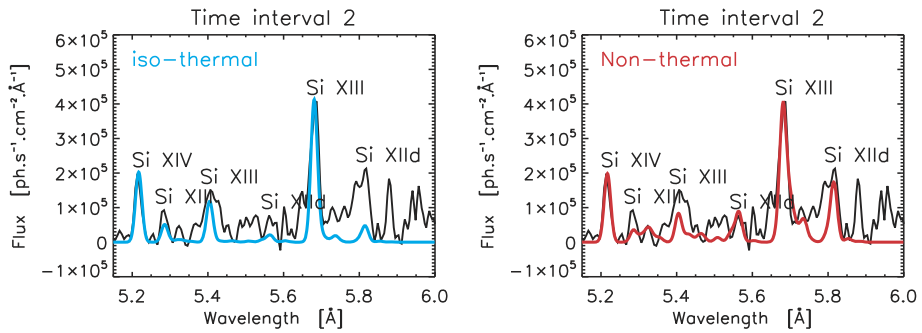


Figure 25 Comparison of the observed spectrum in the RESIK channel 4 with synthetic spectra for the Maxwellian distribution (left) and n -distribution with $n = 11$ (right). Credit: Dzifčáková *et al.* (2008), reproduced with permission © ESO.

from the mean kinetic energy, with the same physical meaning as the temperature for the Maxwellian distribution (Figure 24).

The physical conditions for the origin of the n -distribution were studied by Karlický, Dzifčáková, and Dudík (2012) and Karlický (2012). Karlický, Dzifčáková, and Dudík (2012) investigated the possibility that the n -distribution corresponds to the so-called “moving Maxwellian”, *i.e.*, a Maxwellian with a velocity drift. This distribution matches the n -distribution well; however, for the observed values of n , drift velocities several times higher than the thermal velocity are required. Of course, such a “moving Maxwellian” is unstable because of the Buneman instability. Nevertheless, the n -distribution in solar flares persists for several minutes or more (Dzifčáková *et al.*, 2008; Kulinová *et al.*, 2011). Karlický (2012) found that a distribution similar to an n -distribution can also originate in the double layers that form along flare loops. A strong gradient of the electric field in narrow double layers is able to form a stable non-Maxwellian distribution similar to an n -distribution with a Maxwellian background. As shown by Dzifčáková, Karlický, and Dudík (2013), a strongly peaked electron distribution formed on double layers together with a Maxwellian background distribution can produce spectra with enhanced intensities of satellite lines observed in solar flares.

The ionization equilibrium for n -distributions was calculated by Dzifčáková (1998) and updated by Dzifčáková and Dudík (2015). Calculations of the synthetic spectra (Dzifčáková and Tóthová, 2007) showed that the ionization equilibrium and subsequently the spectra are affected by the distribution function, with the ionization peaks being more peaked. The synthesis of the Fe, Ca, and Si helium-like line spectra during flares were performed for n -distributions by Dzifčáková (2006) and Kulinová *et al.* (2011). The influence on the total radiative losses and continua was subsequently studied by Dudík *et al.* (2011, 2012).

Dzifčáková *et al.* (2008) proposed the use of changes in the ionization and excitation equilibria with n -distributions for diagnostics from the flare X-ray line spectra observed at 5–6 Å by the RESIK spectrometer. These diagnostics used the ratio of the allowed lines of Si XIV to Si XIII, which are sensitive to the ionization state, together with the ratio of the allowed Si XIII line to satellite lines Si XIIId, which is sensitive to the n -distribution. The n -distributions with strong deviation from the Maxwellian, $n \gtrsim 11$, were able to explain high intensities of the satellite lines during the impulsive flare phase (Figure 25). This increase was about a factor two higher than in Maxwellian spectra. The spectra could not be interpreted as multithermal, although the DEM was calculated from the whole RESIK X-

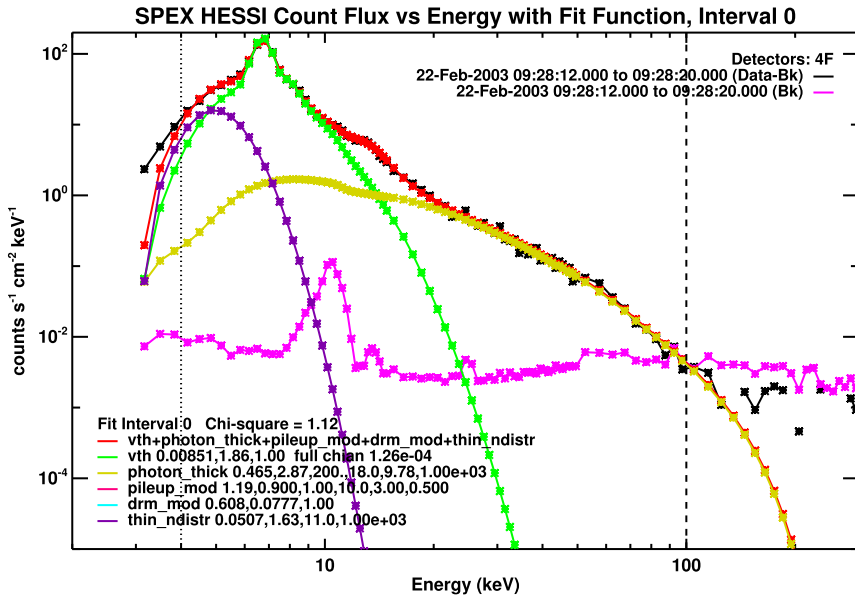


Figure 26 RHESSI spectrum fits of Kulinová *et al.* (2011) including an n -distribution with $n = 11$ (purple). The thermal and high-energy tail components are shown in green and yellow, respectively. Red denotes the sum of all components; black is the observed spectrum. Credit: Kulinová *et al.* (2011), reproduced with permission © ESO.

ray line spectrum. Furthermore, the presence of the n -distribution correlated well with the occurrence of type-III radio bursts.

Kulinová *et al.* (2011) used the nonthermal diagnostics proposed by Dzifčáková *et al.* (2008) for the analysis of three RESIK flares. An analysis of RHESSI data with energies lower than 10 keV (corresponding to the RESIK energy range) was also performed. Although RHESSI is strongly attenuated for these low energies, these authors also successfully diagnosed the n -distribution from RESIK data for two flares for which RHESSI data were available (Figure 26). In addition to this nonthermal component that corresponds to the n -distribution, the RHESSI spectra also contained a thermal component and a high-energy power-law tail. The parameters of the n -distribution derived from RESIK and RHESSI spectra agreed within their respective errors. The emission measure calculated from RHESSI for the n -distribution was about one order higher than for the thermal component of the plasma that explained the non-Maxwellian character of RESIK line spectra (Dzifčáková, Kulinová, and Kašparová, 2011). As in previous cases, the intensities of the satellite lines were enhanced by up to a factor two during the impulsive phase and flare maximum. This enhancement coincided with type-III radio bursts that were observed in radio frequency regions of 2.7–15.4 GHz.

Dzifčáková, Homola, and Dudík (2011) calculated theoretical spectra for a composite np -distribution characterized by an n -distribution bulk and a power-law tail. They showed that this composite distribution is also able to produce enhanced dielectronic satellites, while the Maxwellian distribution with power-law tails alone cannot produce this effect.

The dielectronic satellite lines from other elements in RESIK X-ray spectra usually have low intensities and are blended with allowed lines. This makes the application of a method analogous to Dzifčáková *et al.* (2008) difficult. However, the enhancement of Ar XVII line

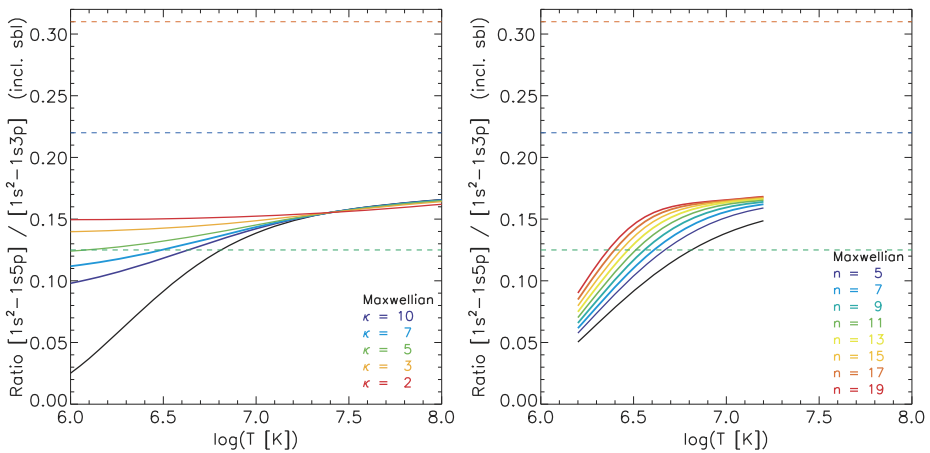


Figure 27 Si XIII $1s^2-1s5p$ to $1s^2-1s3p$ line intensity ratio as a function of temperature and the non-Maxwellian κ -distributions (left) and n -distributions (right panel). The values of individual non-Maxwellian parameters are indicated. Observed line ratios are indicated by dashed horizontal lines, corresponding to the rise (red), maximum (blue), and decay (green) phases of the C5.8 SOL2003-02-22T09:29 flare.

intensities was reported using the RESIK spectra for some flares. This enhancement can also potentially be explained by the overabundance of electrons at several keV similar to the n -distribution (Sylwester, Sylwester, and Phillips, 2008).

Independent theoretical diagnostics of the n -distribution were also proposed. These methods rely on the predicted disappearance of recombination edges in the free-bound continuum (Dudík *et al.*, 2012) or the polarization of gyroresonance emission in micro- and radio-wave regions (Fleishman and Kuznetsov, 2014).

4.3.3. H- and He-like High- n Transitions

During the impulsive phase, RESIK observed emission at wavelengths corresponding to allowed transitions from very high levels characterized by the principal quantum number n up to 6–7 (Kepa *et al.*, 2006). These intensities were strongly enhanced, by a factor of more than two when compared to the transitions from the lower levels ($n = 3$, see dashed lines in Figure 27). In contrast to this, the intensities of $n = 6-7$ lines became close to the expected values during the soft X-ray peak phase. Since the atomic data for these high- n levels were unavailable at the time, Kepa *et al.* (2006) used approximate methods to calculate the synthetic line intensities. These higher- n transitions are sensitive to local plasma conditions and are used in laboratory plasma diagnostics (Chen *et al.*, 2007). The observed intensity ratios could not be explained with an isothermal or multi-temperature approach.

In principle, nonthermal electrons that are present during the impulsive phase of flares could cause the observed increase. To verify this, we have used the cross-sections from the recent UK APAP-network calculations (Fernández-Menchero, Del Zanna, and Badnell, 2016) to predict the effects of a κ - or n -distribution on the line ratios (Figure 27). By considering a κ or n -distribution, it is possible to account for measurements collected for some flares during the decay phase alone, but not during the rise phase (Figure 27). The high-energy tail of a κ -distribution enhances the ratios at lower temperatures, but not at higher temperatures. Only a moderate increase is present for the n -distributions.

Therefore, even assuming the presence of non-Maxwellian electron distributions, this does not explain the strongly enhanced intensities of lines formed from high- n levels. Another possibility is that transient ionization conditions in recombining plasma prevail in the emitting source region. These may result in the overpopulation of higher- n levels (Dupree, 1968). Such persistent presence of recombining plasmas at the formation temperature of the observed lines is unlikely, however. An alternative mechanism contributing to overpopulation of higher- n levels could be charge exchange (Wargelin, Beiersdorfer, and Brown, 2008). Despite these possibilities, the mechanism increasing the high- n line intensities has not yet been identified.

5. Departures from Ionization Equilibrium

When studying the observed emission, it is common to assume that the excitation and de-excitation processes occur independently of ionization and recombination, because the timescales of these processes are extremely different, by orders of magnitude. It is also common to assume that the plasma is in ionization equilibrium, *i.e.*, the ion charge distribution is in a steady state. Such situations were assumed in Sections 3–4. However, it has long been recognized that solar events exist for which this latter assumption is likely to break down, mostly because of the large spectral variability that is observed on timescales shorter than the ion equilibration times. We describe the timescales below, in a separate subsection. We then summarize our current knowledge, based on some previous and more recent observations and models.

5.1. Atomic Timescales

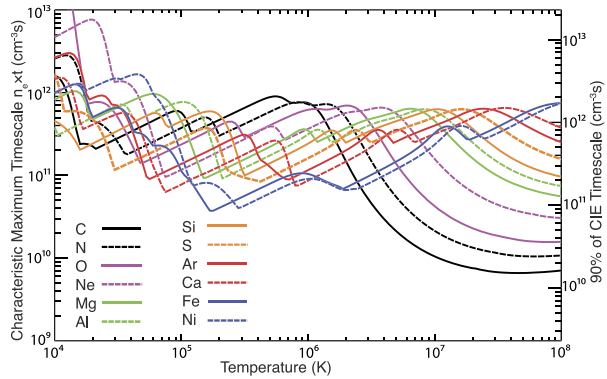
A plasma contains atoms, ions, free electrons, and radiation and may be permeated by a magnetic field. Interaction between these species collectively through collisional and radiative processes establishes the population structure of the emitting atom or ion. In turn, the population structure reflects key parameters of the plasma, such as electron and ion temperature, electron density, the thermal structures of the plasma, its chemical composition and ionization state, and its dynamics.

The lifetimes of the various states of ions vary enormously and determine the relaxation times of the atomic populations. The order of these timescales, together with the plasma development times and their values relative to observation times, determines the modeling approach.

The key lifetimes consist of two groups. The first group includes only the *atomic parameters* (ground, metastable, and excited state radiative decays and autoionizing decay). The second group depends on *plasma conditions*, especially particle density involved in processes such as free particle thermalization, charge-state change including ionization and recombination, and redistribution of population among excited states. Mass flows are also of importance (Sections 5.2 and 5.3). These two groups need to be compared with each other and with the *plasma timescales*, representing relaxation times of transient phenomena, plasma ion diffusion across temperature and density gradients, and observation times.

It is often assumed that the ion populations respond instantaneously to changes in the plasma temperature and density and that the ionization balance is calculated in *ionization equilibrium*. However, whenever there is an extremely rapid change in the plasma conditions, the ionization and recombination timescales can be greater than the plasma timescales.

Figure 28 Characteristic maximum timescales for ion equilibration as a function of T and Z . Individual elements are depicted by different colors and line styles. The axis at the right-hand side gives the density-weighted timescale for equilibration of 90% of the ions. From Smith and Hughes (2010), © AAS. Reproduced with permission.



This implies that the local ionization balance is no longer determined exclusively by the local temperature and density conditions, but depends on the past history of the temperature, density, and ionization state of the plasma. Therefore, the *time-dependent ion populations* need to be determined:

$$\left(\frac{\partial}{\partial t} + \mathbf{u} \cdot \nabla\right) N^{(z)} = n_e [q^{(z-1)} N^{(z-1)} + (q^{(z)} + \alpha^{(z)}) N^{(z)} + \alpha^{(z+1)} N^{(z+1)}], \quad (14)$$

where \mathbf{u} represents the bulk flow velocity and the left-hand side is generally no longer zero as in Equation (11). We recall that q and α are the *effective* ionization and recombination coefficients. They give the contribution to the growth rates for the ground state population, due to the effective ionization, which includes direct and excitation/autoionization contributions, and the effective recombination, which includes radiative, dielectronic, and three-body contributions (see Section 3.3).

Calculations of the ionization equilibration timescales have been performed by several authors, *e.g.*, Golub, Hartquist, and Quillen (1989), Reale and Orlando (2008), and Smith and Hughes (2010). Smith and Hughes (2010) showed that for the case of no flows ($\mathbf{u} = 0$), the characteristic product of the electron density and maximum timescale for equilibration (see Figure 28) is on the order of $n_e t \approx 10^{11} - 10^{12} \text{ cm}^{-3} \text{ s}$ and that the most abundant ion is often the slowest to reach equilibrium. This means that at the densities of few $10^9 - 10^{11} \text{ cm}^{-3}$ that are typical of the active corona and the TR, the solar plasma can be out of ionization equilibrium if intensity changes occur on timescales shorter than about 10–100 s. Such timescales for intensity changes are indeed often observed. Nonequilibrium ionization may be generated by a variety of processes in the solar corona and TR, ranging from impulsive plasma heating and cooling to mass flows through a steep temperature gradient, as in the TR. Since the line intensity (Equation (8)) depends directly on the relative ion abundance given by Equation (14), the presence of nonequilibrium ionization will necessarily lead to transient time-dependent phenomena that can be characterized by fast intensity changes.

5.2. Nonequilibrium Ionization in the TR

It has been known for a long time that the TR is highly dynamic. Even in the TR of the quiet Sun, downflows are ubiquitous, so the ions are flowing into regions with lower temperatures, given the steep gradient. Nonequilibrium ionization effects are therefore important in the TR. IRIS (De Pontieu *et al.*, 2014) observations with high temporal cadence and spatial

resolution (compared to previous missions) have now unambiguously confirmed this. *Hi-C* (Kobayashi *et al.*, 2014) high-resolution, and high-cadence observations have also shown the dynamical nature of the low-temperature emission. Intensity changes on timescales on the order of seconds have now been observed by IRIS and *Hi-C* in a multitude of phenomena outside of flares (*e.g.*, Testa *et al.*, 2013; Régnier *et al.*, 2014; Hansteen *et al.*, 2014; Peter *et al.*, 2014; Tian *et al.*, 2014; Vissers *et al.*, 2015; Tajfrouze *et al.*, 2016; Martínez-Sykora *et al.*, 2016).

5.2.1. 1D Hydrodynamic Modeling

Earlier 1D hydrodynamical modeling showed that nonequilibrium ionization has significant effects on line intensities, electron densities, and even relative abundances in the TR. The literature is extensive (see, *e.g.*, Raymond and Dupree, 1978; Dupree, Moore, and Shapiro, 1979; Borriani and Noci, 1982; Noci *et al.*, 1989; Raymond, 1990; Hansteen, 1993; Spadaro, Leto, and Antiochos, 1994; Edgar and Esser, 2000).

More elaborate 1D hydrodynamical modeling with an adaptive grid and a self-consistent calculation of the total radiative losses was introduced with the HYDRAD code (Bradshaw and Mason, 2003a). HYDRAD calculations confirmed strong enhancements in some TR ions such as C IV (Bradshaw, Del Zanna, and Mason, 2004). We note that ions such as C IV are known to be *anomalous* in the sense that their intensities are much stronger than those from ions formed at similar temperatures, assuming ionization equilibrium in the low-density limit (see, *e.g.*, Del Zanna, Landini, and Mason, 2002, and references therein).

The highly dynamic nature of the TR emission as observed by IRIS was recently studied in terms of nonequilibrium ionization by a number of authors. Doyle *et al.* (2012, 2013) applied the GCR technique to predict the response of TR lines to short heating bursts occurring at loop footpoints. Doyle *et al.* (2013) studied the Si IV 1393.76 Å and O IV 1401.16 Å lines. It was found that about 0.2 s after the occurrence of the burst, Si IV responds with an intensity increase by a factor of more than three, while the intensity of O IV is increased only weakly. With time, the Si IV intensity returns to values closer to the equilibrium values. The authors concluded that a rapid increase of Si IV over O IV is a signature of nonequilibrium ionization.

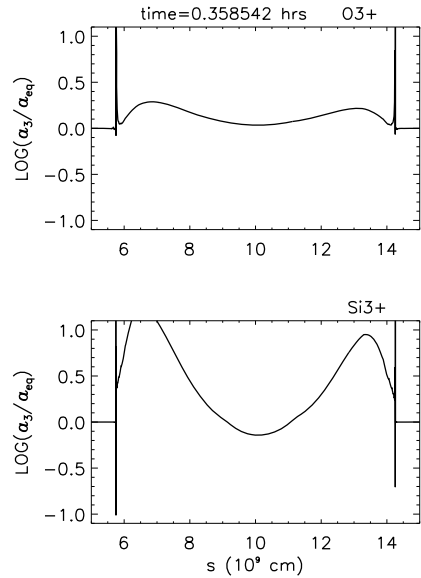
Judge *et al.* (2012) studied the nonequilibrium ionization effects in H, He, C, N, O, and Si during and after the heating of chromospheric plasma described by 1D hydrodynamic equations. In their model, the chromospheric plasma at heights of about 2 Mm was first heated and accelerated upward for about 30 s (model A therein), and then heated for another 30 s, until coronal temperatures of about 1 MK were reached. The evolution of the heated plasma in a calculation assuming ionization equilibrium was found to be more variable than the case involving full nonequilibrium treatment.

5.2.2. An Example of Nonequilibrium Ionization in IRIS TR Lines

To show how the nonequilibrium ionization influences the IRIS TR lines, we present an example hydrodynamic simulation including the nonequilibrium ionization. The emission of two lines, Si IV 1393.76 Å and O IV 1401.16 Å, and their response to nonequilibrium ionization is investigated using numerical simulations of coronal loop hydrodynamics, which reproduce a flaring small-scale event, and are compared with IRIS observations of April 2, 2014.

The standard set of hydrodynamic equations for the conservation of mass, momentum, and energy are solved in a 1D magnetically confined loop with a length of 80 Mm, using

Figure 29 Nonequilibrium/equilibrium population ratios as a function of the loop length for O IV (top panel) and Si IV (bottom panel). From *Giunta et al. (2016)*, © SISSA. Reproduced with permission.



the Adaptively Refined Godunov Solver (ARGOS, Antiochos *et al.*, 1999; MacNiece *et al.*, 2000) code following the approach of Susino *et al.* (2010). To simulate the behavior of a small flare, the case of an impulsive heating event with a pulse cadence of 1/4 of the loop cooling time, *i.e.*, $t = 250 \text{ s} = \tau_{\text{cool}}/4$ (Serio *et al.*, 1991), has been chosen (run 9 in Susino *et al.*, 2010). An energy of 10^{24} erg for each pulse (Parker, 1983, 1988) is supplied to an initial static loop with apex temperature of 7.5×10^5 K.

The system of equations for the ionization balance (Equation (14)) is then solved and provides the variations in ion populations with time for Si IV and O IV (Lanza *et al.*, 2001). The initial state at $t = 0 \text{ s}$ is defined as the static equilibrium loop solution before the heating is supplied.

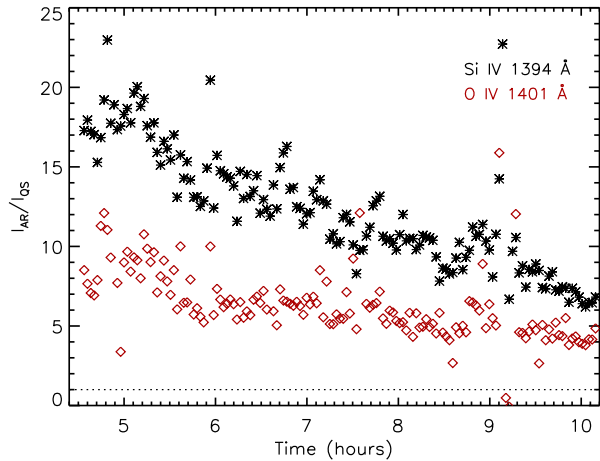
Figure 29 shows the ratio between the transient (a_3) and equilibrium (a_{eq}) ionization balance calculations as a function of the loop length s when the heating is turned on for O IV and Si IV. During a pulse, Si IV is enhanced at loop footpoints by a factor ≈ 10 compared to equilibrium, while O IV is enhanced only by a factor ≈ 3 . This shows that Si IV depends strongly on nonequilibrium ionization, and O IV, in contrast, is less affected.

This different response to transient ionization for the two ions may be directly compared with IRIS observations that investigate the behavior of the two lines Si IV 1349 Å and the O IV 1401 Å and the changes in their intensities during a flaring event with respect to a quiet region (Giunta *et al.*, 2016). When we assume that in the quiet-Sun region both ions are in ionization equilibrium, whereas the rapid variations of plasma conditions due to a transient event, such as a flare, lead to departure from ionization equilibrium, then the following relation is derived for each line (Giunta *et al.*, 2016):

$$\frac{I_{\text{AR}}}{I_{\text{QS}}} = \frac{\int_{\Delta T} G(T_e, n_e, t) dT}{\int_{\Delta T} G(T_e, n_e) dT} = \frac{a_3}{a_{\text{eq}}}, \tag{15}$$

where I_{AR} and I_{QS} are the line intensities of a given line in a flaring region and in a quiet region, respectively, a_3 and a_{eq} stand for the relative ion abundance of the Si IV and O IV out of and in equilibrium, respectively, and a_3/a_{eq} is the ion population ratio as shown in Figure 29.

Figure 30 Observed ratios between the intensities of the flaring region, I_{AR} , and the quiet region, I_{QS} , as a function of time for Si IV 1394 Å (black symbols) and O IV 1401 Å (red symbols). From Giunta *et al.* (2016), © SISSA. Reproduced with permission.



These results can be directly compared to observations. To do this, the data taken on April 2, 2014 from 04:33 to 10:11 UT are used. IRIS was pointed to an active region close to the limb. The observation consisted of a large coarse eight-step raster, with steps $8 \times 2''$, the field of view was $14'' \times 119''$, and the step cadence was 16.4 s. The raster cadence was 131 s with 155 raster positions. To increase the signal, each raster was summed along the X direction, and two regions were selected along the Y direction (200 pixels each): an active region (AR), and a quiet Sun (QS). Although O IV 1401.16 Å is much weaker than Si IV 1393.76 Å, the counts are sufficient when they are binned along X for each raster. Background-subtracted intensity ratios I_{AR}/I_{QS} are shown in Figure 30 as a function of time for the two lines. We see that Si IV is enhanced by a factor $\approx 7\text{--}23$, while the O IV intensity shows a less defined increase, ≈ 5 on average. This is in broad agreement with the enhancement that is due to nonequilibrium ionization of the hydrodynamic simulations shown in Figure 29.

5.2.3. Nonequilibrium Ionization in 3D Modeling with Bifrost and Consequences for IRIS Spectra

While 1D modeling is able to capture both the importance and the details of non-equilibrium ionization along a single magnetic structure, the solar atmosphere and especially the TR consists of many different structures. Realistic modeling of the TR involving many different structures is only possible using 3D codes. In this section, we discuss the setup as well as the results obtained by the Bifrost code (Gudiksen *et al.*, 2011). Bifrost is an MHD code for stellar atmospheres, solving the standard MHD equations using a staggered-mesh explicit code with a sixth-order spatial differential operator and a third-order time accuracy that is achieved through the Hyman predictor–corrector scheme. Boundary conditions are non-periodic, and the reflection at boundaries is minimized. Since the code is explicit, it includes a diffusive operator that is split into a small global diffusive term and a local hyperdiffusion term.

The implementation of the nonequilibrium ionization in the Bifrost simulation is discussed in detail by Olluri, Gudiksen, and Hansteen (2013b). The Bifrost simulation includes wavelength-dependent radiative transfer in non-LTE (i.e., departures from local thermodynamic equilibrium) conditions in the photosphere and lower chromosphere, optically thin

losses in the corona, and field-aligned heat conduction. Heating in the simulation occurs as a result of many dissipation events that relax the stressed magnetic fields (see Hansteen *et al.* 2015 and Carlsson *et al.* 2016 for more details). The nonequilibrium ionization is implemented via the DIPER package (Judge and Meisner, 1994). This approach considers collisional and radiative transitions (ionization, recombination, excitation, and spontaneous emission) between several tens of energy levels for each element. The total number of energy levels has to be restricted in order to make the simulation tractable on current supercomputers. Equations for populations of each level N_i of the form

$$\frac{\partial N_i}{\partial t} + \nabla \cdot (N_i \mathbf{u}) = \sum_{j \neq i}^{N_k} N_j P_{ji} - N_i \sum_{j \neq i}^{N_k} P_{ij} \quad (16)$$

are solved. Here, \mathbf{u} is the plasma bulk velocity, N_k is the total number of levels in the model ion, which can be either excitation or ionization levels, and P_{ij} is the rate coefficient between levels i and j . Equation (16) is solved for 12 levels for Si, 14 levels for O, and 20 levels for Fe X – Fe XV.

Following this implementation, Olluri, Gudiksen, and Hansteen (2013a) found significant departures from the ionization equilibrium in the Bifrost simulation. In particular, individual oxygen ions existed over much wider ranges of temperatures than in the ionization equilibrium (see Figure 3 in Olluri, Gudiksen, and Hansteen, 2013a). For example, O IV was found to exist over the range of $\log(T [\text{K}]) \approx 4.0\text{--}5.8$, and high ion fractions of O VI were found at $\log(T [\text{K}]) \approx 6.0$ instead of 5.5, as would be expected from equilibrium. These departures from equilibrium arose as a combination of advection that brings plasma from different temperature regions together with, *e.g.*, long recombination timescales for O III – O IV and long ionization timescales for O V. The occurrence of significant non-equilibrium ionization was found to have strong consequences for plasma diagnostics. In particular, the density diagnostics from O IV intercombination multiplet around 1400 Å was found to yield results different by up to an order of magnitude when the nonequilibrium ionization was taken into account. This occurred since the O IV emission in the simulation was formed at much lower temperatures than those in the ionization equilibrium. By taking the nonequilibrium ionization into account, Olluri *et al.* (2015) found that the spatially averaged Si IV and O IV intensities compared well with the observed ones.

The influence of nonequilibrium ionization on IRIS spectra has been discussed by De Pontieu *et al.* (2015) and Martínez-Sykora *et al.* (2016). De Pontieu *et al.* (2015) found that the IRIS resolution of 0.3'' does not reduce the significant nonthermal broadening previously observed at a lower resolution of about 1'' in the Si IV 1402.77 Å line. This broadening is on the order of 20 km s⁻¹ and is correlated with the line intensity. Using the Bifrost code, De Pontieu *et al.* (2015) found that the observed correlation between the line broadening and intensity can be only reproduced if nonequilibrium ionization is taken into account. Furthermore, the nonequilibrium ionization produced nonthermal broadening on the order of 2–10 km s⁻¹, a significant contribution to the observed one. Martínez-Sykora *et al.* (2016) reported that the Si IV/O IV ratio is positively correlated with the Si IV intensity, and that the nature of the correlation depends on the feature observed. The strongest increase in Si IV relative to O IV was found in active region spectra. Using the Bifrost MHD simulations, the authors found that the nonequilibrium ionization significantly (but not fully) reduces the discrepancy between the observed and predicted Si IV/O IV ratios and that these ratios become dependent of the Si IV intensities, similarly as observed. The authors explained this correlation as a consequence of the interplay between the thermal stratification of the atmosphere, its dynamics, and the nonequilibrium ionization.

5.3. Nonequilibrium Ionization in the Solar Lower Corona

Although apparently the solar corona often seems quasi-static, there are several cases where nonequilibrium ionization can be important. For example, it is quite possible that short-lived releases of energy occur at relatively low densities, where the plasma is likely out of ionization equilibrium. Here we briefly summarize some recent studies.

Bradshaw and Mason (2003a) studied cooling loops and found that advection flows on the order of $10\text{--}20\text{ km s}^{-1}$ can carry C VII into cooler regions where none should exist in equilibrium. This was a consequence of the long recombination timescales of C VII, which were about $2 \times 10^3\text{ s}$ in the simulation because the densities were lower than about 10^{10} cm^{-3} . As a result, the loop cooled more slowly than it would have done in the ionization equilibrium. Bradshaw and Mason (2003b) investigated the nonequilibrium ionization in a coronal loop that was transiently heated at its apex. Significant departures from ionization equilibrium were again found. The nonequilibrium ionization of Fe was of particular importance, leading to emissivities nearly five times higher than the equilibrium calculations. Furthermore, the emissivity profile along the loop was more uniform than in the equilibrium case.

Short-lived heating events in the solar corona were also considered by Bradshaw and Cargill (2006). In their simulation, a diffuse low-density loop was heated by a 30 s nanoflare. During this time, the apex density increased from 10^7 to 10^9 cm^{-3} , while the electron temperature reached 25 MK during the first 0.5 s and was kept above 10 MK for more than 20 s. As a result of this rapid heating, explosive chromospheric evaporation set in, characterized by strong blueshifts in Fe VIII during the first 15 seconds, followed by blueshifted emission from higher charged states of Fe. The ionic composition was found to be strongly affected by the heating and evaporation. In particular, the lowest charge states were found at highest temperatures. For example, at 20 s, Fe VIII was found to be formed at $\log(T\text{ [K]}) \approx 6.8$, while Fe IX–Fe XIV were found at progressively lower temperatures. Higher ionic stages lagged even farther behind, suggesting that the high-temperature lines, originating above 10 MK in ionization equilibrium, would likely not be observed because their emission measure is very low. These results were verified by Reale and Orlando (2008) using a range of models with heating durations of between 5 and 180 s. These authors concluded that hot plasma above $\approx 5\text{ MK}$ would not be detectable if the nanoflare durations were shorter than about 1 minute. We note that such results present a considerable obstacle in coronal heating studies, especially considering that some of the current instrumentation exhibits “blind spots” in terms of reliable DEM reconstruction at temperatures above $\log(T\text{ [K]}) \approx 6.8$ (Winebarger *et al.*, 2012).

Nanoflare heating occurring in storms that heat different loop threads were considered by Bradshaw and Klimchuk (2011). These authors found that hot plasma above 5 MK is present, but the individual AIA channels would be dominated by warm emission formed close to ionization equilibrium at temperatures of 1–2 MK. For the AIA 131 Å channel, which is sensitive to temperatures above 10 MK, it was found that the hot plasma contributes only up to 6% of the observed signal at most, and this only in cases that are characterized by strong total heating. Nevertheless, this hot emission was found again to be mostly out of equilibrium in short-duration heating models.

Dzifčáková, Dudík, and Mackovjak (2016) investigated the occurrence of non-equilibrium ionization arising from periodic high-energy electron beams. The beams were simulated by changing the distribution function from a Maxwellian to a κ -distribution with the same bulk of the distribution, but with highly different T . The periods considered were on the order of several tens of seconds, similar to the exposure times of coronal spectrometers

such as EIS. The plasma was found to be out of equilibrium for all cases with densities lower than 10^{11} cm^{-3} . Instantaneous spectra showed fast intensity changes in several lines. However, the spectra averaged over one period appeared multithermal, with DEMs similar to those observed for coronal loops.

Finally, significant out-of-equilibrium effects were found when studying the intensities of coronal lines at the base of newly reconnected field lines in the hot cores of active regions by Bradshaw, Aulanier, and Del Zanna (2011). This modeling was developed to provide a plausible explanation, within an interchange reconnection scenario (Del Zanna *et al.*, 2011a) for the coronal outflows, regions where hot ($T > 1 \text{ MK}$) coronal lines show progressively stronger outflows above sunspots and plage areas (Del Zanna, 2008). The reconnection process between a higher-pressure (higher temperature and density) hot loop and a surrounding field would initiate a rarefaction wave traveling toward the chromosphere. After about 300 s in the simulation, the wave produces outflows in the coronal lines that are similar to the observed outflows and are stronger in the higher-temperature lines. The lower-temperature lines around 1–2 MK are still formed near ionization equilibrium, while the higher-temperature lines around 3 MK are enhanced by a factor of two when time-dependent ionization is considered. The rapid expansion cools the plasma that does not recombine fast enough.

To summarize, nonequilibrium ionization effects can be significant at all electron temperatures in the solar corona, with details depending on the nature of the heating and cooling processes, and the associated flows. These nonequilibrium effects are crucial for an interpretation of plasma hotter than 5 MK. Plasma like this contains important information on the nature of coronal heating, but nonequilibrium effects may prevent detection with current instrumentation.

5.4. Nonequilibrium Ionization in Solar Flare Spectra

The high densities ($10^{11} - 10^{12} \text{ cm}^{-3}$) typical of solar flare plasma (for recent measurements see, *e.g.*, Graham, Fletcher, and Hannah, 2011; Del Zanna *et al.*, 2011b; Milligan *et al.*, 2012; Young *et al.*, 2013; Graham, Fletcher, and Labrosse, 2015; Doschek *et al.*, 2015) indicate less favorable conditions for the occurrence of nonequilibrium ionization (see Figure 28) than in the non-flaring solar corona. Nevertheless, nonequilibrium ionization could still be present, especially during the early phase when the electron density is still low.

The best measurements of nonequilibrium ionization effects in flare plasma have been obtained in the past by several instruments that observed the Fe XX–Fe XXVI X-ray emission lines around 1.84–1.92 Å. The ratios of inner-shell excitation lines such as the Fe XXIV q vs. the resonance lines of the He-like Fe XXV strongly depend on the ratio of the Li-like to the He-like relative abundance (Gabriel, 1972). Another diagnostic is the Fe XXIII inner-shell β line. As an example, we show in Figure 31 simulated spectra of this complex obtained by Mewe *et al.* (1985), who studied a flare observed by SMM/BCS. The authors considered heating of a 40 Mm long loop of initial temperature of 3.2 MK and density of $6 \times 10^9 \text{ cm}^{-3}$. Energy deposition occurred either at the apex, at footpoints, or in the form of a chromospheric heating by fast electron beams. It was found that the Ca equilibration times are about 30 s, while for Fe they are about one minute. In the apex heating case, the peak temperature and density was 21 MK and $2 \times 10^{10} \text{ cm}^{-3}$. In the footpoint heating case, the equilibration times were shorter as a result of the lower temperatures and higher densities; 15 MK and $5 \times 10^{10} \text{ cm}^{-3}$, respectively. In the synthetic spectra, it was found that the inner-shell lines such as q and β were enhanced compared to the directly excited resonance lines of He-like Fe XXV and Ca XIX. Furthermore, the ratios of these high-ionization resonance

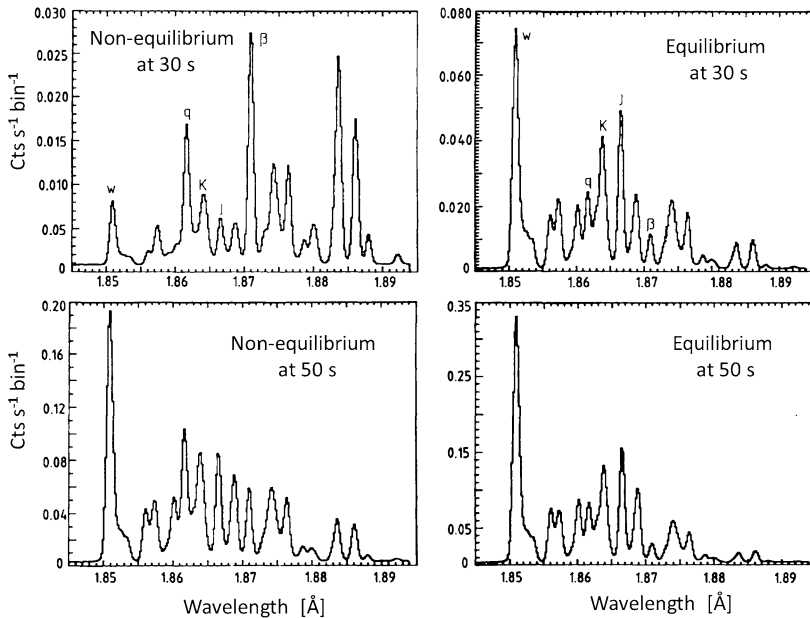


Figure 31 Simulated SMM BCS Fe xxv – xxii spectra for the flare SOL1980-11-12T17:05 30 s and 50 s after the start of transient heating. The left panels show results from a model with nonequilibrium ionization, and the right panels show results from an equilibrium ionization calculation. *Credit: Mewe, Gronenschild, and van den Oord (1985), reproduced with permission © ESO.*

lines relative to the continuum were decreased. This arose since the continuum is dominated by H and He, and is therefore unaffected by the nonequilibrium ionization effects in highly ionized metals.

The technique was also applied by Doschek, Kreplin, and Feldman (1979) to NRL SOLFLEX observations of the Fe lines in flares. They found strong departures from equilibrium, as the plasma can be always underionized. However, Doyle and Raymond (1981) found the data were consistent with ionization equilibrium when they interpreted the observations with different atomic data.

Doschek and Feldman (1981) applied the same technique as Doschek, Kreplin, and Feldman (1979) to NRL SOLFLEX observations of the Ca lines in flares. A similar analysis using the Ca lines observed by SMM/XRP was carried out by several authors, see, *e.g.*, Gabriel, Antonucci, and Steenman-Clark (1983), Antonucci *et al.* (1984). Significant uncertainties were present, but no obvious indications of departures from ionization equilibrium were found. Doschek and Tanaka (1987) reviewed the SMM and *Hinotori* observations, but found no clear evidence of transient ionization effects, although some marginal indications were present during the impulsive phase. With some modeling, they found that these effects can persist for times of up to several $10^{11}/n_e$ seconds. This means that at higher densities, the nonequilibrium ionization effects last shorter than at lower densities. If the flare plasma has densities lower than 10^{11} cm^{-3} , the non-equilibrium ionization can last several seconds or more, but detection is then hampered by the correspondingly low emission measures in combination with the detector sensitivities.

Time-dependent ionization today is often included in hydrodynamical models of flare loops, although the results are often close to those obtained assuming equilibrium. Differences have been found, however. For example, Bradshaw, Del Zanna, and Mason (2004)

applied the HYDRAD code to model the emission of a small compact flare, finding significant differences when nonequilibrium ionization was included. An 80 Mm loop was heated by a 300 s heating pulse located at the apex, raising its temperature from an initial value of 1.6 MK to about 7 MK, accompanied by a density increase from $4.7 \times 10^8 \text{ cm}^{-3}$ by a factor of about three. Flows of up to 200 km s^{-1} were produced. Strong enhancements of He I, He II, and C IV emissivities were found in the impulsive phase, later followed by a decrease. At the position of 20 Mm along the loop and 60 seconds into the simulation, Fe XIV and Fe XV were found to be enhanced over their equilibrium values by a factor of 28 and 6, respectively, but were depleted at the position of 10 Mm along a loop leg. In contrast to this, Fe XVIII was found to be depleted at all positions along the loop. Later on, at 210 s, the Fe XIV–Fe XVI emissions were close to their equilibrium value, while Fe XVII was found to be enhanced in the upper parts of the loop. However, Fe XIX was not present at all in the nonequilibrium ionization simulation.

Simulations using the HYDRAD code have also been carried out recently for a variety of chromospheric evaporation studies in solar flares, including chromospheric heating by electron beams and Alfvén waves (Reep, Bradshaw, and McAteer, 2013; Reep, Bradshaw, and Alexander, 2015; Reep and Russell, 2016; Polito *et al.*, 2016b). These simulations include nonequilibrium ionization by default, often without an accompanying equilibrium calculation. For example, the simulation of Polito *et al.* (2016b) predicted the highest Fe XXI and Fe XXIII evaporation velocities of more than 250 km s^{-1} to occur at the start of the chromospheric evaporation process, and decrease later on. This predicted behavior is in agreement with observed behavior. We note that the apex densities reached in such simulations are typically on the order of 10^{11} cm^{-3} , so that nonequilibrium effects cannot be excluded, especially in smaller flares.

The occurrence of nonequilibrium ionization in a reconnecting current sheet below an erupting flux rope has been studied by Shen *et al.* (2013). These authors found that the lower part of the current sheet is underionized, while the upper part at heights of about $2R_{\odot}$ is overionized. The reason is that in its lower part, the current sheet is heated on timescales shorter than the ionization timescales, while in its upper part, the heated plasma cools and expands more quickly than the recombination timescales. Flows related to the reconnection also played a role. Consequently, temperatures derived from observations would be under- and overestimated at low and large heights, respectively, if equilibrium conditions were assumed. Furthermore, AIA count rates predicted from the nonequilibrium simulation differed significantly from the rate obtained assuming ionization equilibrium. In particular, the discernible thin bright region visible in 131 Å and 94 Å AIA images, corresponding to the center of the current sheet, extends in the nonequilibrium simulation to larger heights than in the equilibrium simulation. In the regions outside of the current sheet, *i.e.*, in the ambient corona, nonequilibrium effects were significant (changes of more than 35% in line intensities) only at heights above $\approx 2R_{\odot}$, where the electron density was low.

5.5. Nonequilibrium Ionization and Solar Wind

Since the electron temperatures in the solar wind do not correspond to the local charge state of the solar wind, the solar wind is also not in ionization equilibrium. The ionic state in the solar wind is commonly inferred using Equation (14) applied to cases of solar wind expansion (*e.g.*, Ko *et al.*, 1997; Edgar and Esser, 2000), which explicitly includes $u \neq 0$. In a steady state that is characterized only by radial outflows, Ko *et al.* (1997) showed that

whether the ionic fractions correspond to equilibrium, or are “frozen in” depends not only on the local electron temperature, but also on the competition between the ion equilibration timescale (see Section 5.1) and the expansion timescale t_{exp} , which is given by

$$t_{\text{exp}} = \left| \frac{u}{n_e} \frac{\partial n_e}{\partial r} \right|^{-1}. \quad (17)$$

At large radii r , the density n_e is low, while the wind velocities u are high, meaning that $\partial N^{(+z)}/\partial r \rightarrow 0$, *i.e.*, the ion charge state is frozen in. Ko *et al.* (1997) showed that this almost always occurs within $5R_{\odot}$ for all the $T(r)$ and $n_e(r)$ studied. For some elements, such as C, O, and Mg, the ionic composition is frozen in (and thus out of equilibrium) at distances larger than $2R_{\odot}$, while for Si and Fe, the freezing-in occurs at radii larger than about $2.5R_{\odot}$ and $4R_{\odot}$, respectively (see Figure 5 therein).

Since the frozen-in charge state depends on the local conditions in the solar wind source region, it can be used to obtain constraints on these source regions (Ko *et al.*, 1997; Esser and Edgar, 2000). It is possible to do this with a variety of models, including different Poynting flux values or magnetic field geometries (open or closed) in different regions such as coronal holes, and even eruptions constituting transients in the solar wind (*e.g.*, Lynch *et al.*, 2011; Gruesbeck *et al.*, 2011; Landi *et al.*, 2012a,b, 2014; Lepri *et al.*, 2012; Oran *et al.*, 2015; Rodkin *et al.*, 2017).

The evolution of the charge state along an open magnetic field line was studied in a series of articles by Landi *et al.* (2012a,b, 2014). It was found that wind-induced departures from ionization equilibrium existed in the solar atmosphere, producing differences of up to a factor of three in total radiative losses of the upper chromosphere and TR when compared to equilibrium ion composition (Landi *et al.*, 2012b). Carbon and oxygen showed the most pronounced departures from equilibrium. Landi *et al.* (2012a) showed that the ions emitting the brightest lines (such as C IV, N V, O V–O VI) especially at low heights in coronal holes were out of equilibrium. Most ions except for the highest ionization states were found to be overabundant. However, at larger heights, some ions such as O V–O VI and Fe VIII–Fe XII were close to equilibrium, with departures being smaller than 25% in the case of Fe ions. Landi *et al.* (2014) used the models of Hansteen and Leer (1995), Cranmer, van Ballegoijen, and Edgar (2007), and Oran *et al.* (2013) to predict the emission line intensities and the fast solar wind charge-state distributions, and found that while TR lines are predicted well, coronal line intensities and the fast wind charge-state distribution are underpredicted, possibly because the fast wind encounters difficulties in reaching the high-ionization stages that correspond to local conditions.

Oran *et al.* (2015) calculated the charge-state evolution covering all latitudes in a realistic open magnetic field, and obtained similar results. In particular, the O VIII/O VII and C VII/C VI charge state ratios are underpredicted when compared to *Ulysses* observations. Similarly, the intensities of the S, Si, and Fe lines were underpredicted when compared to *Hinode*/EIS observations of a coronal hole. These authors suggested that the ionization rates in the low corona, which they assumed to be Maxwellian, are likely underpredicted. It was found that adding a second Maxwellian with 2% of particles and a temperature of 3 MK produced a much better agreement with both the observed charge-state composition and the EIS intensities. We note that Cranmer (2014) suggested that mild suprathermal tails characterized by a κ -distribution with $\kappa = 10$ –25 can be sufficiently energetic to enhance the O charge state in the solar wind.

6. Future Instrumentation for the Detection of Nonequilibrium Phenomena

As we have shown, detection of the nonequilibrium effects in the solar atmosphere through remote-sensing observations has proven difficult because of limitations in instrumentation or the small magnitude of the expected effects. A plasma may only be out of ionization equilibrium for tens of seconds in some cases (or a few seconds in the case of Doyle *et al.*, 2013), while the emission measure of the transient plasma may be very low (Section 5.4). Simultaneous coverage of consecutive ion stages of an element would allow transient ionization to be tracked through the atmosphere, while high-sensitivity observations of strong lines are needed to capture the evolution at cadences on the order of seconds. To study transient ionization during flares, new instruments with much improved sensitivity are required.

Remote-sensing detection of non-Maxwellian electron distributions provides a further challenge: to be sensitive to the distribution, a pair of emission lines from an ion should have significantly different excitation thresholds, but these lines are often widely separated in wavelength. This also places strong demands on the radiometric calibration of the instrument (*cf.*, BenMoussa *et al.*, 2013; Del Zanna, 2013; Warren, Ugarte-Urra, and Landi, 2014), which should have accuracies of 10% or better over this wavelength range. In addition, the lines are often weaker than the strongest lines from the ion (*e.g.*, Mackovjak, Dzifčáková, and Dudík, 2013; Dudík *et al.*, 2015), which means that again, high sensitivity is critical. Additionally, in the EUV and especially the X-ray range high spectral resolution is needed to resolve blended lines (Section 4.3).

In this section, we discuss the capabilities of future remote-sensing instruments for detecting signatures of nonequilibrium processes in the solar atmosphere. We include both instruments under construction (Section 6.1) and future design concepts (Section 6.2). *In situ* instruments were discussed in Sections 2.5 and 2.6, which highlighted future capabilities for improved measurements that will reach locations closer to the Sun than previously achieved.

6.1. Instruments Under Construction

At present, several instruments are under construction. These will be flown on *Solar Orbiter*, *Interhelioprobe*, *Proba-3*, the *International Space Station* (ISS), as well as sounding rockets.

6.1.1. *Solar Orbiter*

The *Solar Orbiter* mission will be the first to fully explore the interface region where solar wind and heliospheric structures originate. It will carry six remote-sensing and four *in situ* instruments that will link the solar wind to its source regions in the solar atmosphere. *Solar Orbiter* has been selected as the first medium-class mission of ESA's Cosmic Vision 2015–2025 program, implemented with NASA, and is due to be launched in 2018. *Solar Orbiter* will operate in coordination with *Solar Probe Plus*,¹² a NASA mission also due to be launched in 2018. The *Solar Probe Plus* will fly into the low solar corona, providing a unique opportunity for a deep investigation of the processes by which the Sun produces and accelerates the solar wind and energetic particles, and it will also probe how the solar corona is heated.

¹²<http://solarprobe.jhuapl.edu>.

The Spectral Investigation of the Coronal Environment (SPICE; Fludra *et al.*, 2013) onboard *Solar Orbiter* operates at extreme ultraviolet wavelengths in two bands, 704–790 Å and 973–1049 Å, which are dominated by emission lines from a wide range of ions of H, C, O, N, Ne, S, Mg, Si, and Fe. These lines are formed at temperatures from 10^4 to 10^7 K, allowing the study of the solar atmosphere from the chromosphere in the Lyman- β line up to the flaring corona (*e.g.*, Fe xx 721 Å). SPICE will mainly observe cool lines, so that in principle it could provide useful measurements for studying nonequilibrium ionization in the TR. Telemetry limitations will place some constraints on the number of lines and the field of view, however. Moreover, the sensitivity will only allow exposure times on the order of seconds for the stronger lines.

The *Spectrometer Telescope for Imaging X-rays* (STIX) will perform imaging spectroscopy in the X-ray region 4 to 150 keV using a Fourier-transform imaging technique similar to the technique used by the previous *Yohkoh*/HXT and RHESSI instruments. A set of cadmium telluride (CdTe) X-ray detectors provides a spectral resolution of ~ 1 keV at 6 keV, with unprecedented spatial resolution and sensitivity (near perihelion). A detailed description of the imaging technique is given in Benz *et al.* (2012).

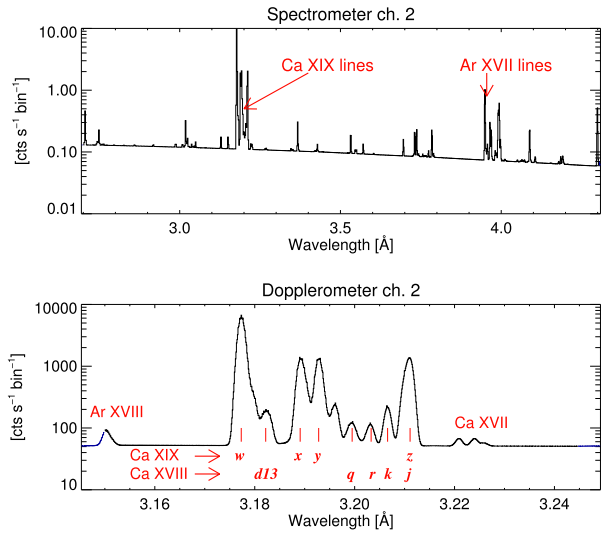
The set of *in situ* instruments on-board *Solar Orbiter* will allow plasma composition and energy distribution functions of individual particle species to be measured in the vicinity of the probe. On the other hand, STIX will play a key role by measuring nonthermal electron distribution functions in the solar atmosphere. A connection from the solar surface to the heliosphere can thus be made, in particular, how the distribution functions are modified by transport processes operating in the heliosphere.

6.1.2. Interhelioprobe

The Russian *Interhelioprobe* (IHP, Oraevsky *et al.*, 2001) program includes sending two interplanetary probes on orbits similar to the orbit of *Solar Orbiter*, reaching a location as close to the Sun as ≈ 60 solar radii. The probes are planned for launch in 2025 and 2026, and they will enable stereoscopic observations of the solar activity. Every one of the gravitational assist maneuvers will increase the inclinations of the orbital plane to the ecliptic, reaching 30° in the later phase of the missions. At perihelion, the structures of the solar atmosphere will be observed with a spatial resolution about three times better than from Earth, with the solar radiative fluxes up to 13 times greater. Both IHP spacecraft will be equipped with the identical ≈ 150 kg science payloads, consisting of 20 instruments for remote and *in situ* plasma diagnostics (Kuznetsov, 2015).

On both IHP spacecraft, the Polish-led Bragg bent-crystal spectrometer ChemiX (Siarkowski *et al.*, 2016) will be placed. This spectrometer will observe active regions and flaring plasma in the spectral range 1.5–9 Å using 10 monocrystal wafers that are bent cylindrically, which allow an improvement of a factor 10 in spectral resolution over RESIK. Careful construction and appropriate selection of materials will cause the X-ray fluorescence produced by the irradiance of solar X-rays on the instrument material, which commonly forms a background emission, to be minimized, allowing for reliable continuum measurements. Four crystals will cover slightly overlapping spectral ranges 1.500–2.713 Å, 2.700–4.304 Å, 4.290–5.228 Å, and 5.200–8.800 Å. The overlaps will allow for cross-calibration. The use of cooled CCD detectors to record the spectra will result in an increase of an order of magnitude of the continuum-to-background signal compared to RESIK. The other three pairs of identical crystal-detector units will form three Dopplerometers. The analysis of their high spectral resolution measurements will allow for precise determinations of the line-of-sight component of plasma motions.

Figure 32 Simulated ChemiX spectra as seen on the CCD at 1 AU predicted using the CHIANTI database. Top: spectrum in channel 2 containing the Ca XIX and Ar XVIII line groups. Bottom: Dopplerometer channel 2 spectrum that contains mostly the Ca He-like ion spectra in high resolution. A number of satellite lines are well resolved.



We note that the ChemiX spectral range contains dielectronic satellite lines that can be used to discern the non-Maxwellian effects (Section 4.3.2) from a range of elements and at a range of energies of 1.4–8.2 keV; this will enable sampling of the distribution function. Figure 32 shows examples of simulated spectra from channels 1 and 4. This simulation assumes plasma with temperature $T_e \approx 18.7$ MK and emission measure $EM \approx 5.6 \times 10^{49} \text{ cm}^{-3}$; *i.e.*, conditions corresponding to a typical GOES M5 class solar flare. Collimator and CCD efficiency are assumed to be unity.

6.1.3. SolpeX on the ISS

Another instrument capable of collecting high-resolution soft X-ray spectra and detect polarization is *Solar Polarimeter in X-rays* (SolpeX). This instrument consists of three functionally independent blocks that are included within the Russian instrument KORTES, to be mounted on the Sun-pointed platform onboard the *International Space Station* (ISS). The three SolpeX units are a simple pin-hole soft X-ray imager and spectrophotometer with a spatial resolution of $\approx 20''$, a spectral resolution of 0.5 keV, and a high cadence of 0.1 s; the *Bragg polarimeter* B-POL observing at 3.9–4.6 Å with a low linear polarization detection threshold of 1–2%, and finally, the fast-rotating drum X-ray spectrometer (RDS) with a high time resolution of 0.1 s. This combination of measuring blocks offers an opportunity to reliably measure possible X-ray polarization and high-cadence spectra of solar flares, in particular during the impulsive phase. Polarized bremsstrahlung and line emission caused by directed particle beams can be detected, and measurements of the velocities of evaporated hot plasma will be made.

Lines of only a few elements that are suitable for polarization detections are present in the B-POL spectral range. To extend the spectral coverage over the entire soft X-ray range (1–23 Å), the RDS spectrometer was included. A novelty of this instrument is the wavelength assignment to each photon that is Bragg-reflected from the crystal. This will be achieved by using the timing information on the photon arrival on the silicon drift detector. The symmetrical location of detectors on both sides of the drum with respect to the direction toward the Sun represents the configuration that is necessary to fulfill the tasks of a Dopplerometer

(Sylwester *et al.*, 2015). Eight flat crystals are planned to be used, two of them identical. Two identical crystals are placed in the classical Dopplerometer configuration. The combination of all the rotating crystals will enable a continuous spectral coverage, extending from 0.3 Å to 22.8 Å, recorded every 0.1 s.

6.1.4. Marshall Grazing-Incidence X-ray Spectrometer

The *Marshall Grazing-Incidence X-ray Spectrometer* (MAGIXs) is a NASA spectrometer designed to observe the Sun at energies of 6–24 Å (0.5–2 keV) with a spectral resolution of 22 mÅ and spatial resolution of $\approx 5''$. The instrument will be flown on a sounding rocket, allowing for ≈ 5 -minute observations of a portion of the solar corona. The spectral range of MAGIXs contains many Fe XVII–Fe XX spectral lines (Del Zanna and Mason, 2014; Schmelz and Winebarger, 2015). A goal of this mission is to constrain the amount of hot plasma in the solar active region cores. As discussed in Section 5.3, the emission measure of this plasma may be low because of the nonequilibrium ionization effects. Additionally, the multiple Fe XVII–Fe XVIII lines observed within the MAGIXs wavelength window may offer opportunities of detecting high-energy tails, possibly in combination with the AIA 94 Å filter observations.

6.1.5. Proba-3

Proba-3 is the first ESA mission to test new technologies to fly two spacecraft with tight constraints on their alignment. *Proba-3* will perform solar coronagraphic observations. The first spacecraft is the occulter. The second spacecraft, at about 150 meters away, has the coronagraph. The instrument will obtain measurements of the polarized brightness in the visible and of the forbidden Fe XIV coronal line. As we discussed in Section 3.5.2, observations of the forbidden visible line, in combination with those of the EUV Fe XIV lines (*e.g.*, from *Hinode*/EIS if the instrument is still operational), are potentially very useful to indicate whether non-Maxwellian distributions are present in the solar corona.

6.2. Proposed Future Instruments

6.2.1. The EUVST Instrument Proposed for Solar-C

The *Extreme-Ultraviolet Spectroscopic Telescope* (EUVST, Teriaca *et al.*, 2012), previously also named LEMUR (*Large European Module for solar Ultraviolet Research*) is an image-stabilized imaging spectrometer with a 0.14" pixel size and 0.3" spatial resolution that should observe in several spectral ranges, 170–215 Å, 690–850 Å, 925–1085 Å, and 1115–1275 Å in the first order and 463–542 Å and 557–637 Å in the second order with a spectral resolution $\lambda/\Delta\lambda$ of about $1.6\text{--}3 \times 10^4$. The design enables very short exposure times, up to 0.1 s for the brightest spectral lines. The EUVST has been proposed as an instrument for the JAXA-led *Solar-C* mission during the ESA M4 mission call in 2014, but was not approved at the time.

Multiple widely spaced spectral bands will enable non-Maxwellian diagnostics from lines formed at widely different energies, for example O IV. In addition, the high spatial resolution will allow the occurrence of nonequilibrium phenomena to be pinpointed to individual structures in the atmosphere.

6.2.2. Microcalorimeters

In the early 1980s, it was realized that microcalorimeters have the potential to measure the energy of an X-ray keV photon with an accuracy of a few eV. This is comparable with the spectral resolution of crystal Bragg spectrometers, but the effective area of a microcalorimeter is 4–5 orders of magnitude better. A microcalorimeter is a unique instrument as it allows simultaneously determining the energy and position of each X-ray incoming photon. At present, the best energy resolution (1.8 eV at 6 keV) is obtained with microcalorimeters with superconducting transition-edge sensors (TESs, Benz *et al.*, 2012). In the future, metallic magnetic microcalorimeters (MMCs) should enable sub-eV resolution. Thanks to their enormous sensitivity, microcalorimeters can revolutionize our understanding of coronal plasma processes, especially as concerns the non-equilibrium plasma dynamics of solar flares and active regions (Laming *et al.*, 2010). With appropriate imagers, direct observations of the spectra of microflares and possibly nanoflares will be possible. With a spectral resolution on the order of 1 eV, the spectral line profiles can be studied in detail, including thermal, Doppler, microturbulence, and multitemperature components. These components were seen in SMM BCS spectra of the main phase of flares (*cf.*, Figure 20).

Microcalorimeters could enable the detection of departures from ionization equilibrium in the impulsive phase, particularly in the 6.7 keV Fe line complex (Section 5.4). Intensity ratios of dielectronic satellites to the resonance line can also be used to determine the electron temperature, while the inner-shell excitation lines can be used to determine the abundance ratio of the Li-like/He-like Fe ions. In ionization equilibrium, the temperatures from these two ratios should be equal, but non-equality would indicate either an ionizing or recombining plasma.

Furthermore, the Fe XXI/Fe XXII ratios observed with crystal spectrometers on SMM were used to detect high electron densities in solar flares, approaching $10^{12} - 10^{13} \text{ cm}^{-3}$ (Phillips *et al.*, 1996). The microcalorimeter would provide similar spectral resolution, but with significantly wider bandpass, throughput, and spatial resolution.

7. Concluding Remarks

We have shown that nonequilibrium processes, including non-Maxwellian distributions and nonequilibrium ionization, can be important in a range of observed phenomena in the solar atmosphere. These include the TR, which is highly variable, solar active regions, and solar flares, and finally, the solar wind. Not including these nonequilibrium processes into the observational analysis can lead to severe misinterpretation of observations, while omitting them in time-dependent models can have significant consequences for the modeled dynamics.

Regarding the non-Maxwellian distributions, we note that strong constraints have been obtained for high-energy particles in the quiet solar atmosphere. This indicates that a range of structures in the quiet corona are probably close to being Maxwellian. In other coronal and TR structures, however, signatures of non-Maxwellian distributions were detected using EIS and IRIS. The non-Maxwellians are also routinely observed in the solar wind. It is currently unknown how the origin of the non-Maxwellian solar wind relates to structures in the low solar corona observed in UV, EUV, and X-rays. Although theoretical diagnostics for the detection of these non-Maxwellians in the wind source regions are being developed, they often rely on weaker spectral lines and/or the use of broad spectral ranges to capture lines formed at different excitation thresholds. This brings additional constraints in terms of

instrument calibration. In particular, the relative calibration uncertainties should be lowered in future missions, and careful accounting of the in-flight instrument degradation needs to be performed. Finally, to understand coronal heating and the formation of the solar wind, we need a set of remote-sensing and *in situ* observations that cover the solar atmosphere seamlessly from the chromosphere to the upper corona and then to the wind. The set of spacecraft under construction, such as *Solar Orbiter*, *Solar Probe Plus*, and *Interhelioprobe*, will for the first time help with this task, but should be supplemented with next-generation remote-sensing instruments operating in the UV and EUV, such as the proposed EUVST instrument.

Solar flares represent a class of dynamic phenomena for which non-Maxwellian distributions are routinely detected. It is important, however, to constrain the non-Maxwellian properties not only at high energies where the bremsstrahlung emission is observed with spectrometers such as RHESSI, but also at intermediate and low energies. The combination of RHESSI and AIA observations has shown that simple power-law fits to the high-energy bremsstrahlung emission are often incompatible with the emission detected at lower energies. Finally, the situation is further complicated by peaked n -distributions, especially during the impulsive phase of solar flares. To distinguish the various contributions to the observed emission, high spatial resolution are needed to understand the formation and propagation of these non-Maxwellians in the various structures involved in the flare. Additionally, we are currently in the curious situation of having better flare line spectra from stellar observations made by instruments such as *Chandra* and *XMM-Newton* than we do of the Sun (Laming *et al.*, 2010). A set of instruments under construction will resolve this mismatch, enabling direct comparisons with stellar observations in addition to addressing the issues discussed above. Furthermore, we also note that the observations of X-ray lines formed at lower temperatures in active region cores may lead to strong constraints on the properties of the electron distribution function there. The MAGIXs instrument will address this issue.

Dynamic phenomena in the solar atmosphere characterized by transient heating or cooling lead to the occurrence of nonequilibrium ionization. Although nonequilibrium ionization is more pronounced at lower densities, it can be important for nearly all layers of the outer solar atmosphere, from the TR to corona and even flares. Recent theoretical work has shown that nonequilibrium ionization can dramatically decrease the discrepancies between the TR line intensities observed by IRIS. In addition, the transient ionization significantly decreases the emission measure from the high-temperature emission that is expected to arise as a result of nanoflare heating of the corona. Diagnosing nonequilibrium ionization from observations is not straightforward as it requires observing ions with very different ionization and/or recombination rates, such as the Si IV and O IV ions observed with IRIS, or consecutive ionization stages of a single element. This further emphasizes the need to simultaneously observe numerous spectral lines from many ions. Such observations must also go hand-in-hand with time-dependent numerical modeling.

In summary, the presence and importance of nonequilibrium phenomena in the solar atmosphere and wind is now beyond question. These processes need to be carefully evaluated for each emitting structure; this task complicates the observational analysis. For such an undertaking to be routinely performed in the future, high-quality spectroscopic observations are indispensable. Publicly available spectroscopic databases including the necessary atomic data, such as CHIANTI, OPEN-ADAS, and KAPPA, are a cornerstone of such analyses. The accessibility of modeling codes such as HYDRAD and BIFROST is also invaluable.

Acknowledgements The authors thank the anonymous referee for numerous improvements to the manuscript. The authors also acknowledge useful discussions with M. Battaglia, P. Heinzel and A. Zemanová. J.D. and E.Dz. authors acknowledge support by Grant Agency of the Czech Republic, Grant No.

17-16447S, and institutional support RVO:67985815 from the Czech Academy of Sciences. G.D.Z. and H.E.M. acknowledge funding from STFC. J.D., G.D.Z., and H.E.M. acknowledge funding from Royal Society via the Newton Alumni programme. P.R.Y. acknowledges support from NASA grant NNX15AF25G. A.G. acknowledges the in-house research support provided by the STFC. B.S. and J.S. acknowledge support from the Polish National Science Centre grant 2013/11/B/ST9/00234. M.O. was supported by NASA grant NNX08AO83G at UC Berkeley. L.M. was supported by the UK Science and Technology Facilities Council grant ST/K001051/1. The authors benefited greatly from participation in the International Team 276 funded by the International Space Science Institute (ISSI) in Bern, Switzerland. CHIANTI is a collaborative project involving the University of Cambridge (UK), the George Mason University (USA), and the University of Michigan (USA). ADAS is a project managed at the University of Strathclyde (UK) and funded through memberships universities and astrophysics and fusion laboratories in Europe and worldwide.

References

- Acton, L.W., Finch, M.L., Gilbreth, C.W., Culhane, J.L., Bentley, R.D., Bowles, J.A., Guttridge, P., Gabriel, A.H., Firth, J.G., Hayes, R.W.: 1980, The soft X-ray polychromator for the Solar Maximum Mission. *Solar Phys.* **65**, 53. [DOI](#). [ADS](#).
- Allred, J.C., Kowalski, A.F., Carlsson, M.: 2015, A unified computational model for solar and stellar flares. *Astrophys. J.* **809**, 104. [DOI](#). [ADS](#).
- Antiochos, S.K., MacNeice, P.J., Spicer, D.S., Klimchuk, J.A.: 1999, The dynamic formation of prominence condensations. *Astrophys. J.* **512**, 985. [DOI](#). [ADS](#).
- Antonucci, E., Gabriel, A.H., Doyle, J.G., Dubau, J., Faucher, P., Jordan, C., Veck, N.: 1984, Derivation of ionization balance for calcium XVIII/XIX using XRP solar X-ray data. *Astron. Astrophys.* **133**, 239. [ADS](#).
- Arnaud, M., Raymond, J.: 1992, Iron ionization and recombination rates and ionization equilibrium. *Astrophys. J.* **398**, 394. [DOI](#). [ADS](#).
- Arnaud, M., Rothenflug, R.: 1985, An updated evaluation of recombination and ionization rates. *Astron. Astrophys. Suppl.* **60**, 425. [ADS](#).
- Aschwanden, M.J.: 2005, *Physics of the Solar Corona. An Introduction with Problems and Solutions*, 2nd edn., Springer, Berlin. [ADS](#).
- Badnell, N.R.: 2006, Radiative recombination data for modeling dynamic finite-density plasmas. *Astrophys. J. Suppl.* **167**, 334. [DOI](#). [ADS](#).
- Badnell, N.R., O'Mullane, M.G., Summers, H.P., Altun, Z., Bautista, M.A., Colgan, J., Gorczyca, T.W., Mitnik, D.M., Pindzola, M.S., Zatsarinny, O.: 2003, Dielectronic recombination data for dynamic finite-density plasmas. I. Goals and methodology. *Astron. Astrophys.* **406**, 1151. [DOI](#). [ADS](#).
- Bale, S.D., Goetz, K., Harvey, P.R., Turin, P., Bonnell, J.W., Dudok de Wit, T., Ergun, R.E., MacDowall, R.J., Puluza, M., Andre, M., Bolton, M., Bougeret, J.-L., Bowen, T.A., Burgess, D., Cattell, C.A., Chandran, B.D.G., Chaston, C.C., Chen, C.H.K., Choi, M.K., Connerney, J.E., Cranmer, S., Diaz-Aguado, M., Donakowski, W., Drake, J.F., Farrell, W.M., Ferreau, P., Fermin, J., Fischer, J., Fox, N., Glaser, D., Goldstein, M., Gordon, D., Hanson, E., Harris, S.E., Hayes, L.M., Hinze, J.J., Hollweg, J.V., Horbury, T.S., Howard, R.A., Hoxie, V., Jannet, G., Karlsson, M., Kasper, J.C., Kellogg, P.J., Kien, M., Klimchuk, J.A., Krasnoselskikh, V.V., Krucker, S., Lynch, J.J., Maksimovic, M., Malaspina, D.M., Marker, S., Martin, P., Martinez-Oliveros, J., McCauley, J., McComas, D.J., McDonald, T., Meyer-Vernet, N., Moncuquet, M., Monson, S.J., Mozer, F.S., Murphy, S.D., Odom, J., Oliverson, R., Olson, J., Parker, E.N., Pankow, D., Phan, T., Quataert, E., Quinn, T., Ruplin, S.W., Salem, C., Seitz, D., Sheppard, D.A., Siy, A., Stevens, K., Summers, D., Szabo, A., Timofeeva, M., Vaivads, A., Velli, M., Yehle, A., Werthimer, D., Wygant, J.R.: 2016, The FIELDS instrument suite for Solar Probe Plus – measuring the coronal plasma and magnetic field, plasma waves and turbulence, and radio signatures of solar transients. *Space Sci. Rev.* **204**, 49. [DOI](#). [ADS](#).
- Bartirromo, R., Bombarda, F., Giannella, R.: 1985, Spectroscopic study of nonthermal plasmas. *Phys. Rev. A* **32**, 531. [DOI](#). [ADS](#).
- Battaglia, M., Benz, A.O.: 2006, Relations between concurrent hard X-ray sources in solar flares. *Astron. Astrophys.* **456**, 751. [DOI](#). [ADS](#).
- Battaglia, M., Kontar, E.P.: 2013, Electron distribution functions in solar flares from combined X-ray and extreme-ultraviolet observations. *Astrophys. J.* **779**, 107. [DOI](#). [ADS](#).
- Battaglia, M., Motorina, G., Kontar, E.P.: 2015, Multithermal representation of the kappa-distribution of solar flare electrons and application to simultaneous X-ray and EUV observations. *Astrophys. J.* **815**, 73. [DOI](#). [ADS](#).
- Beck, A., Meyer-Vernet, N.: 2008, The trajectory of an electron in a plasma. *Am. J. Phys.* **76**, 934. [DOI](#).

- Benáček, J., Karlický, M., Yasnov, L.V.: 2017, Temperature dependent growth rates of the upper-hybrid waves and solar radio zebra patterns. *Astron. Astrophys.* **598**, A106. DOI. ADS, 6 pp.
- BenMoussa, A., Gissot, S., Schühle, U., Del Zanna, G., Auchère, F., Mekaoui, S., Jones, A.R., Walton, D., Eyles, C.J., Thuillier, G., Seaton, D., Dammasch, I.E., Cessateur, G., Meftah, M., Andretta, V., Berghmans, D., Bewsher, D., Bolsée, D., Bradley, L., Brown, D.S., Chamberlin, P.C., Dewitte, S., Didkovsky, L.V., Dominique, M., Eparvier, F.G., Foujols, T., Gillotay, D., Giordanengo, B., Halain, J.P., Hock, R.A., Irbah, A., Jeppesen, C., Judge, D.L., Kretschmar, M., McMullin, D.R., Nicula, B., Schmutz, W., Ucker, G., Wieman, S., Woodraska, D., Woods, T.N.: 2013, On-orbit degradation of solar instruments. *Solar Phys.* **288**, 389. DOI. ADS.
- Benz, A., Krucker, S., Hurford, G.J., Arnold, N.G., Orleanski, P., Gröbelbauer, H.-P., et al.: 2012, The spectrometer telescope for imaging X-rays on board the Solar Orbiter mission. *Proc. SPIE* **8443**, 84433L. DOI. ADS. Space Telescopes and Instrumentation 2012: Ultraviolet to Gamma Ray.
- Benz, A.O.: 2008, Flare observations. *Living Rev. Solar Phys.* **5**, 1. DOI.
- Bian, N.H., Kontar, E.P.: 2013, Stochastic acceleration by multi-island contraction during turbulent magnetic reconnection. *Phys. Rev. Lett.* **110**(15), 151101. DOI. ADS.
- Bian, N.H., Emslie, A.G., Stackhouse, D.J., Kontar, E.P.: 2014, The formation of kappa-distribution accelerated electron populations in solar flares. *Astrophys. J.* **796**, 142. DOI. ADS.
- Boerner, P., Edwards, C., Lemen, J., Rausch, A., Schrijver, C., Shine, R., Shing, L., Stern, R., Tarbell, T., Title, A., Wolfson, C.J., Soufli, R., Spiller, E., Gullikson, E., McKenzie, D., Windt, D., Golub, L., Podgorski, W., Testa, P., Weber, M.: 2012, Initial calibration of the Atmospheric Imaging Assembly (AIA) on the Solar Dynamics Observatory (SDO). *Solar Phys.* **275**, 41. DOI. ADS.
- Bogachev, S.A., Somov, B.V.: 2005, Comparison of the Fermi and betatron acceleration efficiencies in collapsing magnetic traps. *Astron. Lett.* **31**, 537. DOI. ADS.
- Borrini, G., Noci, G.: 1982, Non-equilibrium ionization in coronal loops. *Solar Phys.* **77**, 153. DOI. ADS.
- Bradshaw, S.J., Cargill, P.J.: 2006, Explosive heating of low-density coronal plasma. *Astron. Astrophys.* **458**, 987. DOI. ADS.
- Bradshaw, S.J., Klimchuk, J.A.: 2011, What dominates the coronal emission spectrum during the cycle of impulsive heating and cooling? *Astrophys. J. Suppl.* **194**, 26. DOI. ADS.
- Bradshaw, S.J., Mason, H.E.: 2003a, A self-consistent treatment of radiation in coronal loop modelling. *Astron. Astrophys.* **401**, 699. DOI. ADS.
- Bradshaw, S.J., Mason, H.E.: 2003b, The radiative response of solar loop plasma subject to transient heating. *Astron. Astrophys.* **407**, 1127. DOI. ADS.
- Bradshaw, S.J., Raymond, J.: 2013, Collisional and radiative processes in optically thin plasmas. *Space Sci. Rev.* **178**, 271. DOI. ADS.
- Bradshaw, S.J., Aulanier, G., Del Zanna, G.: 2011, A reconnection-driven rarefaction wave model for coronal outflows. *Astrophys. J.* **743**, 66. DOI. ADS.
- Bradshaw, S.J., Del Zanna, G., Mason, H.E.: 2004, On the consequences of a non-equilibrium ionisation balance for compact flare emission and dynamics. *Astron. Astrophys.* **425**, 287. ADS.
- Bradshaw, S.J., Klimchuk, J.A., Reep, J.W.: 2012, Diagnosing the time-dependence of active region core heating from the emission measure. I. Low-frequency nanoflares. *Astrophys. J.* **758**, 53. DOI. ADS.
- Brown, J.C.: 1971, The deduction of energy spectra of non-thermal electrons in flares from the observed dynamic spectra of hard X-ray bursts. *Solar Phys.* **18**, 489. DOI. ADS.
- Bryans, P.: 2006, On the spectral emission of non-Maxwellian plasmas. Ph.D. thesis, University of Strathclyde. ADS.
- Bryans, P., Landi, E., Savin, D.W.: 2009, A new approach to analyzing solar coronal spectra and updated collisional ionization equilibrium calculations. II. Updated ionization rate coefficients. *Astrophys. J.* **691**, 1540. DOI. ADS.
- Burge, C.A., MacKinnon, A.L., Petkaki, P.: 2014, Effect of binary collisions on electron acceleration in magnetic reconnection. *Astron. Astrophys.* **561**, A107. DOI. ADS.
- Burge, C.A., Petkaki, P., MacKinnon, A.L.: 2012, Particle acceleration in the presence of weak turbulence at an X-type neutral point. *Solar Phys.* **280**, 575. DOI. ADS.
- Bykov, A.M., Malkov, M.A., Raymond, J.C., Krassilchtchikov, A.M., Vladimirov, A.E.: 2013, Collisionless shocks in partly ionized plasma with cosmic rays: Microphysics of non-thermal components. *Space Sci. Rev.* **178**, 599. DOI. ADS.
- Cargill, P.J.: 2014, Active region emission measure distributions and implications for nanoflare heating. *Astrophys. J.* **784**, 49. DOI. ADS.
- Cargill, P.J., Vlahos, L., Baumann, G., Drake, J.F., Nordlund, Å.: 2012, Current fragmentation and particle acceleration in solar flares. *Space Sci. Rev.* **173**, 223. DOI. ADS.
- Carlsson, M., Stein, R.F.: 2002, Dynamic hydrogen ionization. *Astrophys. J.* **572**, 626. DOI. ADS.
- Carlsson, M., Hansteen, V.H., Gudiksen, B.V., Leenaarts, J., De Pontieu, B.: 2016, A publicly available simulation of an enhanced network region of the Sun. *Astron. Astrophys.* **585**, A4. DOI. ADS.

- Caspi, A., Lin, R.P.: 2010, RHESSI line and continuum observations of super-hot flare plasma. *Astrophys. J. Lett.* **725**, L161. DOI. ADS.
- Caspi, A., Krucker, S., Lin, R.P.: 2014, Statistical properties of super-hot solar flares. *Astrophys. J.* **781**, 43. DOI. ADS.
- Chateau, Y.F., Meyer-Vernet, N.: 1991, Electrostatic noise in non-Maxwellian plasmas – generic properties and ‘kappa’ distributions. *J. Geophys. Res.* **96**, 5825. DOI. ADS.
- Che, H., Goldstein, M.L.: 2014, The origin of non-Maxwellian solar wind electron velocity distribution function: Connection to nanoflares in the solar corona. *Astrophys. J. Lett.* **795**, L38. DOI. ADS.
- Chen, H., Gu, M.F., Behar, E., Brown, G.V., Kahn, S.M., Beiersdorfer, P.: 2007, Laboratory measurements of high- n iron L-Shell X-ray lines. *Astrophys. J. Suppl.* **168**, 319. DOI. ADS.
- Chen, Q., Petrosian, V.: 2012, Impulsive phase coronal hard X-ray sources in an X3.9 class solar flare. *Astrophys. J.* **748**, 33. DOI. ADS.
- Chew, G.F., Goldberger, M.L., Low, F.E.: 1956, The Boltzmann equation and the one-fluid hydromagnetic equations in the absence of particle collisions. *Proc. Roy. Soc. London Ser. A, Math. Phys. Sci.* **236**, 112. DOI. ADS.
- Chiuderi, C., Chiuderi Drago, F.: 2004, Effect of suprathermal particles on the quiet Sun radio emission. *Astron. Astrophys.* **422**, 331. DOI. ADS.
- Collier, M.R.: 2004, Are magnetospheric suprathermal particle distributions (κ functions) inconsistent with maximum entropy considerations? *Adv. Space Res.* **33**, 2108. DOI. ADS.
- Cranmer, S.R.: 2014, Suprathermal electrons in the solar corona: Can nonlocal transport explain heliospheric charge states? *Astrophys. J. Lett.* **791**, L31. DOI. ADS.
- Cranmer, S.R., van Ballegooyen, A.A., Edgar, R.J.: 2007, Self-consistent coronal heating and solar wind acceleration from anisotropic magnetohydrodynamic turbulence. *Astrophys. J. Suppl.* **171**, 520. DOI. ADS.
- Cranmer, S.R., Matthaeus, W.H., Breech, B.A., Kasper, J.C.: 2009, Empirical constraints on proton and electron heating in the fast solar wind. *Astrophys. J.* **702**, 1604. DOI. ADS.
- Culhane, J.L., Hiei, E., Doschek, G.A., Cruise, A.M., et al.: 1991, The Bragg crystal spectrometer for SOLAR-A. *Solar Phys.* **136**, 89. DOI. ADS.
- Culhane, J.L., Harra, L.K., James, A.M., Al-Janabi, K., Bradley, L.J., Chaudry, R.A., Rees, K., Tandy, J.A., Thomas, P., Whillock, M.C.R., Winter, B., Doschek, G.A., Korendyke, C.M., Brown, C.M., Myers, S., Mariska, J., Seely, J., Lang, J., Kent, B.J., Shaughnessy, B.M., Young, P.R., Simnett, G.M., Castelli, C.M., Mahmoud, S., Mapson-Menard, H., Probyn, B.J., Thomas, R.J., Davila, J., Dere, K., Windt, D., Shea, J., Hagood, R., Moye, R., Hara, H., Watanabe, T., Matsuzaki, K., Kosugi, T., Hansteen, V., Wikstol, Ø.: 2007, The EUV imaging spectrometer for Hinode. *Solar Phys.* **243**, 19. DOI. ADS.
- Curdt, W., Brekke, P., Feldman, U., Wilhelm, K., Dwivedi, B.N., Schühle, U., Lemaire, P.: 2001, The SUMER spectral atlas of solar-disk features. *Astron. Astrophys.* **375**, 591. DOI. ADS.
- De Pontieu, B., Title, A.M., Lemen, J.R., Kushner, G.D., Akin, D.J., Allard, B., Berger, T., Boerner, P., Cheung, M., Chou, C., Drake, J.F., Duncan, D.W., Freeland, S., Heyman, G.F., Hoffman, C., Hurlburt, N.E., Lindgren, R.W., Mathur, D., Rehse, R., Sabolish, D., Seguin, R., Schrijver, C.J., Tarbell, T.D., Wülser, J.-P., Wolfson, C.J., Yanari, C., Mudge, J., Nguyen-Phuc, N., Timmons, R., van Bezoujen, R., Weingrod, I., Brookner, R., Butcher, G., Dougherty, B., Eder, J., Knagenhjelm, V., Larsen, S., Mansir, D., Phan, L., Boyle, P., Cheimets, P.N., DeLuca, E.E., Golub, L., Gates, R., Hertz, E., McKillop, S., Park, S., Perry, T., Podgorski, W.A., Reeves, K., Saar, S., Testa, P., Tian, H., Weber, M., Dunn, C., Eccles, S., Jaeggli, S.A., Kankelborg, C.C., Mashburn, K., Pust, N., Springer, L., Carvalho, R., Kleint, L., Marmie, J., Mazmanian, E., Pereira, T.M.D., Sawyer, S., Strong, J., Worden, S.P., Carlsson, M., Hansteen, V.H., Leenaarts, J., Wiesmann, M., Aloise, J., Chu, K.-C., Bush, R.I., Scherrer, P.H., Brekke, P., Martinez-Sykora, J., Lites, B.W., McIntosh, S.W., Uitenbroek, H., Okamoto, T.J., Gummin, M.A., Auker, G., Jerram, P., Pool, P., Waltham, N.: 2014, The Interface Region Imaging Spectrograph (IRIS). *Solar Phys.* **289**, 2733. DOI. ADS.
- De Pontieu, B., McIntosh, S., Martinez-Sykora, J., Peter, H., Pereira, T.M.D.: 2015, Why is non-thermal line broadening of spectral lines in the lower transition region of the sun independent of spatial resolution? *Astrophys. J. Lett.* **799**, L12. DOI. ADS.
- Del Zanna, G.: 2008, Flows in active region loops observed by Hinode EIS. *Astron. Astrophys.* **481**, L49. DOI. ADS.
- Del Zanna, G.: 2013, A revised radiometric calibration for the Hinode/EIS instrument. *Astron. Astrophys.* **555**, A47. DOI. ADS.
- Del Zanna, G., Mason, H.E.: 2003, Solar active regions: SOHO/CDS and TRACE observations of quiescent coronal loops. *Astron. Astrophys.* **406**, 1089. DOI. ADS.
- Del Zanna, G., Mason, H.E.: 2014, Elemental abundances and temperatures of quiescent solar active region cores from X-ray observations. *Astron. Astrophys.* **565**, A14. DOI. ADS.

- Del Zanna, G., Fernández-Menchero, L., Badnell, N.R.: 2015, Benchmarking atomic data for astrophysics: Si III. *Astron. Astrophys.* **574**, A99. DOI. ADS.
- Del Zanna, G., Landini, M., Mason, H.E.: 2002, Spectroscopic diagnostics of stellar transition regions and coronae in the XUV: AU Mic in quiescence. *Astron. Astrophys.* **385**, 968.
- Del Zanna, G., Aulanier, G., Klein, K.-L., Török, T.: 2011a, A single picture for solar coronal outflows and radio noise storms. *Astron. Astrophys.* **526**, A137. DOI. ADS.
- Del Zanna, G., Mitra-Kraev, U., Bradshaw, S.J., Mason, H.E., Asai, A.: 2011b, The 22 May 2007 B-class flare: New insights from Hinode observations. *Astron. Astrophys.* **526**, A1. DOI. ADS.
- Del Zanna, G., Storey, P.J., Badnell, N.R., Mason, H.E.: 2012, Atomic data for astrophysics: Fe XII soft X-ray lines. *Astron. Astrophys.* **543**, A139. DOI. ADS.
- Del Zanna, G., Storey, P.J., Badnell, N.R., Mason, H.E.: 2014, Atomic data for astrophysics: Fe IX. *Astron. Astrophys.* **565**, A77. DOI. ADS.
- Del Zanna, G., Dere, K.P., Young, P.R., Landi, E., Mason, H.E.: 2015a, CHIANTI – an atomic database for emission lines. Version 8. *Astron. Astrophys.* **582**, A56. DOI. ADS.
- Del Zanna, G., Tripathi, D., Mason, H., Subramanian, S., O'Dwyer, B.: 2015b, The evolution of the emission measure distribution in the core of an active region. *Astron. Astrophys.* **573**, A104. DOI. ADS.
- Dere, K.P.: 2007, Ionization rate coefficients for the elements hydrogen through zinc. *Astron. Astrophys.* **466**, 771. DOI. ADS.
- Dere, K.P., Landi, E., Mason, H.E., Monsignori Fossi, B.C., Young, P.R.: 1997, CHIANTI – an atomic database for emission lines. *Astron. Astrophys. Suppl.* **125**, 149. DOI. ADS.
- Doschek, G.A., Feldman, U.: 1981, On ionization equilibrium in solar flares as determined from X-ray emission lines of Ca XVIII and Ca XIX. *Astrophys. J.* **251**, 792. DOI. ADS.
- Doschek, G.A., Tanaka, K.: 1987, Transient ionization and solar flare X-ray spectra. *Astrophys. J.* **323**, 799. DOI. ADS.
- Doschek, G.A., Kreplin, R.W., Feldman, U.: 1979, High-resolution solar flare X-ray spectra. *Astrophys. J. Lett.* **233**, L157. ADS.
- Doschek, G.A., Warren, H.P., Dennis, B.R., Reep, J.W., Caspi, A.: 2015, Flare footpoint regions and a surge observed by Hinode/EIS, RHESSI, and SDO/AIA. *Astrophys. J.* **813**, 32. DOI. ADS.
- Doyle, J.G., Raymond, J.C.: 1981, New ionization fractions for the lithium- and helium-like ionization stages of calcium and iron. *Mon. Not. Roy. Astron. Soc.* **196**, 907. DOI. ADS.
- Doyle, J.G., Raymond, J.C.: 1984, Flare parameters for the 7 September, 1973 two-ribbon flare. *Solar Phys.* **90**, 97. DOI. ADS.
- Doyle, J.G., Madjarska, M.S., Dzifčáková, E., Dammasch, I.E.: 2004, Coronal response of bi-directional jets. *Solar Phys.* **221**, 51. DOI. ADS.
- Doyle, J.G., Giunta, A., Singh, A., Madjarska, M.S., Summers, H., Kellett, B.J., O'Mullane, M.: 2012, The diagnostic potential of transition region lines undergoing transient ionization in dynamic events. *Solar Phys.* **280**, 111. DOI. ADS.
- Doyle, J.G., Giunta, A., Madjarska, M.S., Summers, H., O'Mullane, M., Singh, A.: 2013, Diagnosing transient ionization in dynamic events. *Astron. Astrophys.* **557**, L9. DOI. ADS.
- Drake, J.F., Swisdak, M., Che, H., Shay, M.A.: 2006, Electron acceleration from contracting magnetic islands during reconnection. *Nature* **443**, 553. DOI.
- Dudík, J., Dzifčáková, E., Karlický, M., Kulinová, A.: 2011, The bound–bound and free–free radiative losses for the nonthermal distributions in solar and stellar coronae. *Astron. Astrophys.* **529**, A103. DOI. ADS.
- Dudík, J., Kašparová, J., Dzifčáková, E., Karlický, M., Mackovjak, Š.: 2012, The non-Maxwellian continuum in the X-ray, UV, and radio range. *Astron. Astrophys.* **539**, A107. DOI. ADS.
- Dudík, J., Del Zanna, G., Mason, H.E., Dzifčáková, E.: 2014a, Signatures of the non-Maxwellian κ -distributions in optically thin line spectra. I. Theory and synthetic Fe IX – XIII spectra. *Astron. Astrophys.* **570**, A124. DOI. ADS.
- Dudík, J., Del Zanna, G., Dzifčáková, E., Mason, H.E., Golub, L.: 2014b, Solar transition region lines observed by the interface region imaging spectrograph: Diagnostics for the O IV and Si IV lines. *Astrophys. J. Lett.* **780**, L12. DOI. ADS.
- Dudík, J., Mackovjak, Š., Dzifčáková, E., Del Zanna, G., Williams, D.R., Karlický, M., Mason, H.E., Lörinčík, J., Kotřč, P., Fárník, F., Zemanová, A.: 2015, Imaging and spectroscopic observations of a transient coronal loop: Evidence for the non-Maxwellian $kappa$ -distributions. *Astrophys. J.* **807**, 123. DOI. ADS.
- Dufton, P.L., Kingston, A.E., Keenan, F.P.: 1984, Observational evidence for non-Maxwellian electron energy distributions in the solar transition region. *Astrophys. J. Lett.* **280**, L35. DOI. ADS.
- Duijveman, A., Hoyng, P., Machado, M.E.: 1982, X-ray imaging of three flares during the impulsive phase. *Solar Phys.* **81**, 137. DOI. ADS.
- Dupree, A.K.: 1968, The population of high atomic levels in the solar corona. *Astrophys. J.* **152**, L125. DOI.

- Dupree, A.K., Moore, R.T., Shapiro, P.R.: 1979, Nonequilibrium ionization in solar and stellar winds. *Astrophys. J. Lett.* **229**, L101. DOI. ADS.
- Dzifčáková, E.: 1992, The ionization balance of the Fe in the solar corona for a non-Maxwellian electron distribution function. *Solar Phys.* **140**, 247. DOI. ADS.
- Dzifčáková, E.: 1998, The ionization equilibrium in the solar corona for the electron power distribution. *Solar Phys.* **178**, 317. DOI. ADS.
- Dzifčáková, E.: 2002, The updated Fe ionization equilibrium for the electron κ -distributions. *Solar Phys.* **208**, 91. ADS.
- Dzifčáková, E.: 2006, The influence of the electron κ -distribution in the solar corona on the Fe VIII–Fe XV line intensities. *Solar Phys.* **234**, 243. DOI. ADS.
- Dzifčáková, E., Dudík, J.: 2013, H to Zn ionization equilibrium for the non-Maxwellian electron κ -distributions: Updated calculations. *Astrophys. J. Suppl.* **206**, 6. DOI. ADS.
- Dzifčáková, E., Dudík, J.: 2015, Ionisation equilibrium for the non-Maxwellian electron n -distributions in solar flares: Updated calculations. *Solar Phys.* **290**, 3545. DOI. ADS.
- Dzifčáková, E., Kulinová, A.: 2001, The Fe XXV excitation equilibrium in the solar corona for the electron power distributions using a pseudo-temperature. *Solar Phys.* **203**, 53. DOI. ADS.
- Dzifčáková, E., Kulinová, A.: 2010, The diagnostics of the Kappa-distributions from EUV spectra. *Solar Phys.* **263**, 25.
- Dzifčáková, E., Kulinová, A.: 2011, Diagnostics of the κ -distribution using Si III lines in the solar transition region. *Astron. Astrophys.* **531**, A122. DOI. ADS.
- Dzifčáková, E., Mason, H.E.: 2008, Computation of non-Maxwellian electron excitation rates for ions of astrophysical interest: Fe XV – a test case. *Solar Phys.* **247**, 301.
- Dzifčáková, E., Tóthová, D.: 2007, Synthetic spectra of the Fe VIII – Fe XVI emission lines for electron non-thermal distributions. *Solar Phys.* **240**, 211. DOI. ADS.
- Dzifčáková, E., Dudík, J., Mackovjak, Š.: 2016, Non-equilibrium ionization by a periodic electron beam. I. Synthetic coronal spectra and implications for interpretation of observations. *Astron. Astrophys.* **589**, A68. DOI. ADS.
- Dzifčáková, E., Homola, M., Dudík, J.: 2011, The ionization equilibrium and flare line spectra for the electron distribution with a power-law tail. *Astron. Astrophys.* **531**, A111. DOI. ADS.
- Dzifčáková, E., Karlický, M., Dudík, J.: 2013, Dielectronic satellite lines and double layers in solar flares. *Astron. Astrophys.* **550**, A60. DOI. ADS.
- Dzifčáková, E., Kulinová, A., Kašparová, J.: 2011, The Diagnostics of the Shape of the Electron Distribution Function during the Solar Flares. In: Johns-Krull, C., Browning, M.K., West, A.A. (eds.) *16th Cambridge Workshop on Cool Stars, Stellar Systems, and the Sun, Astronomical Society of the Pacific Conference Series* **448**, 1095. ADS.
- Dzifčáková, E., Kulinová, A., Chifor, C., Mason, H.E., Del Zanna, G., Sylwester, J., Sylwester, B.: 2008, Nonthermal and thermal diagnostics of a solar flare observed with RESIK and RHESSI. *Astron. Astrophys.* **488**, 311. DOI. ADS.
- Dzifčáková, E., Dudík, J., Kotrč, P., Fárník, F., Zemanová, A.: 2015, KAPPA: A package for synthesis of optically thin spectra for the non-Maxwellian κ -distributions based on the Chianti database. *Astrophys. J. Suppl.* **217**, 14. DOI. ADS.
- Edgar, R.J., Esser, R.: 2000, Nonequilibrium ionization and first ionization potential effect diagnostics. *Astrophys. J. Lett.* **538**, L167. DOI. ADS.
- Esser, R., Edgar, R.J.: 2000, Reconciling spectroscopic electron temperature measurements in the solar corona with in situ charge state observations. *Astrophys. J. Lett.* **532**, L71. DOI. ADS.
- Feldman, U., Landi, E., Doschek, G.A.: 2007, Diagnostics of suprathermal electrons in active-region plasmas using He-like UV lines. *Astrophys. J.* **660**, 1674. DOI. ADS.
- Fernández-Menclero, L., Del Zanna, G., Badnell, N.R.: 2016, Scaling of collision strengths for highly-excited states of ions of the H- and He-like sequences. *Astron. Astrophys.* **592**, A135. DOI. ADS.
- Fleishman, G.D., Kuznetsov, A.A.: 2014, Theory of gyroresonance and free-free emissions from non-Maxwellian quasi-steady-state electron distributions. *Astrophys. J.* **781**, 77. DOI. ADS.
- Fletcher, L., Dennis, B.R., Hudson, H.S., Krucker, S., Phillips, K., Veronig, A., Battaglia, M., Bone, L., Caspi, A., Chen, Q., Gallagher, P., Grigis, P.T., Ji, H., Liu, W., Milligan, R.O., Temmer, M.: 2011, An observational overview of solar flares. *Space Sci. Rev.* **159**, 19. DOI. ADS.
- Fludra, A., Griffin, D., Caldwell, M., Eccleston, P., Cornaby, J., Drummond, D., Grainger, W., Greenway, P., Grundy, T., Howe, C., McQuirk, C., Middleton, K., Poyntz-Wright, O., Richards, A., Rogers, K., Sawyer, C., Shaughnessy, B., Sidher, S., Tosh, I., Beardsley, S., Burton, G., Marshall, A., Waltham, N., Woodward, S., Appourchoux, T., Philippon, A., Auchere, F., Buchlin, E., Gabriel, A., Vial, J.-C., Schühle, U., Curdt, W., Innes, D., Meinig, S., Peter, H., Solanki, S., Teriaca, L., Gyo, M., Büchel, V., Haberleiter, M., Pfiffner, D., Schmutz, W., Carlsson, M., Haugan, S.V., Davila, J., Jordan, P., Thompson, W., Hassler, D., Walls, B., Deforest, C., Hanley, J., Johnson, J., Phelan, P., Blecha, L., Cottard, H.,

- Paciotti, G., Autissier, N., Allemand, Y., Relecom, K., Munro, G., Butler, A., Klein, R., Gottwald, A.: 2013, SPICE EUV spectrometer for the Solar Orbiter mission. In: *Solar Physics and Space Weather Instrumentation V, Proc. SPIE* **8862**, 88620F. DOI. ADS.
- Gabriel, A.H.: 1972, Dielectronic satellite spectra for highly-charged helium-like ion lines. *Mon. Not. Roy. Astron. Soc.* **160**, 99. DOI. ADS.
- Gabriel, A.H., Phillips, K.J.H.: 1979, Dielectronic satellite spectra for highly charged helium-like ions. IV – iron satellite lines as a measure of non-thermal electron energy distributions. *Mon. Not. Roy. Astron. Soc.* **189**, 319. ADS.
- Gabriel, A.H., Antonucci, E., Steenman-Clark, L.: 1983, Non-thermal and non-equilibrium effects in soft X-ray flare spectra. *Solar Phys.* **86**, 59. DOI. ADS.
- Galloway, R.K., Helander, P., MacKinnon, A.L., Brown, J.C.: 2010, Thermalisation and hard X-ray bremsstrahlung efficiency of self-interacting solar flare fast electrons. *Astron. Astrophys.* **520**, A72. DOI. ADS.
- Garrett, B.H.: 1981, The charging of spacecraft surfaces (paper 1R1000). *Rev. Geophys. Space Phys.* **19**, 577. DOI. ADS.
- Giuliani, P., Neukirch, T., Wood, P.: 2005, Particle motion in collapsing magnetic traps in solar flares. I. Kinematic theory of collapsing magnetic traps. *Astrophys. J.* **635**, 636. DOI. ADS.
- Giunta, A.S., Henderson, S., O’Mullane, M., Harrison, J., Doyle, J.G., Summers, H.P.: 2016, Diagnosing transient plasma status: from solar atmosphere to tokamak divertor. *J. Instrum.* **11**, C09008. DOI. ADS.
- Golding, T.P., Carlsson, M., Leenaarts, J.: 2014, Detailed and simplified nonequilibrium helium ionization in the solar atmosphere. *Astrophys. J.* **784**, 30. DOI. ADS.
- Golding, T.P., Leenaarts, J., Carlsson, M.: 2016, Non-equilibrium helium ionization in an MHD simulation of the solar atmosphere. *Astrophys. J.* **817**, 125. DOI. ADS.
- Golub, L., Hartquist, T.W., Quillen, A.C.: 1989, Comments on the observability of coronal variations. *Solar Phys.* **122**, 245. DOI. ADS.
- Golub, L., Deluca, E., Austin, G., Bookbinder, J., Caldwell, D., Cheimets, P., Cirtain, J., Cosmo, M., Reid, P., Sette, A., Weber, M., Sakao, T., Kano, R., Shibasaki, K., Hara, H., Tsuneta, S., Kumagai, K., Tamura, T., Shimojo, M., McCracken, J., Carpenter, J., Haight, H., Siler, R., Wright, E., Tucker, J., Rutledge, H., Barbera, M., Peres, G., Varisco, S.: 2007, The X-Ray Telescope (XRT) for the Hinode Mission. *Solar Phys.* **243**, 63. DOI. ADS.
- Gordovskyy, M., Browning, P.K., Kontar, E.P., Bian, N.H.: 2013, Effect of collisions and magnetic convergence on electron acceleration and transport in reconnecting twisted solar flare loops. *Solar Phys.* **284**, 489. DOI. ADS.
- Gordovskyy, M., Browning, P.K., Kontar, E.P., Bian, N.H.: 2014, Particle acceleration and transport in reconnecting twisted loops in a stratified atmosphere. *Astron. Astrophys.* **561**, A72. DOI. ADS.
- Graham, D.R., Fletcher, L., Hannah, I.G.: 2011, Hinode/EIS plasma diagnostics in the flaring solar chromosphere. *Astron. Astrophys.* **532**, A27. DOI. ADS.
- Graham, D.R., Fletcher, L., Labrosse, N.: 2015, Determining energy balance in the flaring chromosphere from oxygen V line ratios. *Astron. Astrophys.* **584**, A6. DOI. ADS.
- Gruesbeck, J.R., Lepri, S.T., Zurbuchen, T.H., Antiochos, S.K.: 2011, Constraints on coronal mass ejection evolution from in situ observations of ionic charge states. *Astrophys. J.* **730**, 103. DOI. ADS.
- Gu, M.F.: 2003, Radiative recombination rate coefficients for bare through F-like isosequences of Mg, Si, S, Ar, Ca, Fe, and Ni. *Astrophys. J.* **589**, 1085. DOI. ADS.
- Gudiksen, B.V., Carlsson, M., Hansteen, V.H., Hayek, W., Leenaarts, J., Martínez-Sykora, J.: 2011, The stellar atmosphere simulation code Bifrost. Code description and validation. *Astron. Astrophys.* **531**, A154. DOI. ADS.
- Guo, F., Giacalone, J.: 2012, Particle acceleration at a flare termination shock: Effect of large-scale magnetic turbulence. *Astrophys. J.* **753**, 28. DOI. ADS.
- Hahn, M., Savin, D.W.: 2015, A simple method for modeling collision processes in plasmas with a kappa energy distribution. *Astrophys. J.* **809**, 178. DOI. ADS.
- Hannah, I.G., Kontar, E.P.: 2012, Differential emission measures from the regularized inversion of Hinode and SDO data. *Astron. Astrophys.* **539**, A146. DOI. ADS.
- Hannah, I.G., Kontar, E.P.: 2013, Multi-thermal dynamics and energetics of a coronal mass ejection in the low solar atmosphere. *Astron. Astrophys.* **553**, A10. DOI. ADS.
- Hannah, I.G., Hudson, H.S., Hurford, G.J., Lin, R.P.: 2010, Constraining the hard X-ray properties of the quiet sun with new RHESSI observations. *Astrophys. J.* **724**, 487. DOI. ADS.
- Hannah, I.G., Hudson, H.S., Battaglia, M., Christe, S., Kašparová, J., Krucker, S., Kundu, M.R., Veronig, A.: 2011, Microflares and the statistics of X-ray flares. *Space Sci. Rev.* **159**, 263. DOI. ADS.
- Hannah, I.G., Grefenstette, B.W., Smith, D.M., Glesener, L., Krucker, S., Hudson, H.S., Madsen, K.K., Marsh, A., White, S.M., Caspi, A., Shih, A.Y., Harrison, F.A., Stern, D., Boggs, S.E., Christensen,

- F.E., Craig, W.W., Hailey, C.J., Zhang, W.W.: 2016, The first X-ray imaging spectroscopy of quiescent solar active regions with NuSTAR. *Astrophys. J. Lett.* **820**, L14. DOI. ADS.
- Hansteen, V.: 1993, A new interpretation of the redshift observed in optically thin transition region lines. *Astrophys. J.* **402**, 741. DOI. ADS.
- Hansteen, V.H., Leer, E.: 1995, Coronal heating, densities, and temperatures and solar wind acceleration. *J. Geophys. Res.* **100**, 21577. DOI. ADS.
- Hansteen, V., De Pontieu, B., Carlsson, M., Lemen, J., Title, A., Boerner, P., Hurlburt, N., Tarbell, T.D., Wuelser, J.P., Pereira, T.M.D., De Luca, E.E., Golub, L., McKillop, S., Reeves, K., Saar, S., Testa, P., Tian, H., Kankelborg, C., Jaeggli, S., Kleint, L., Martínez-Sykora, J.: 2014, The unresolved fine structure resolved: IRIS observations of the solar transition region. *Science* **346**, 1255757. DOI. ADS.
- Hansteen, V., Guerreiro, N., De Pontieu, B., Carlsson, M.: 2015, Numerical simulations of coronal heating through footpoint braiding. *Astrophys. J.* **811**, 106. DOI. ADS.
- Harrison, F.A., Craig, W.W., Christensen, F.E., Hailey, C.J., Zhang, W.W., Boggs, S.E., Stern, D., Cook, W.R., Forster, K., Giommi, P., Grefenstette, B.W., Kim, Y., Kitaguchi, T., Koglin, J.E., Madsen, K.K., Mao, P.H., Miyasaka, H., Mori, K., Perri, M., Pivovarov, M.J., Puccetti, S., Rana, V.R., Westergaard, N.J., Willis, J., Zoglauer, A., An, H., Bachetti, M., Barrière, N.M., Bellm, E.C., Bhalerao, V., Brejnholt, N.F., Fuerst, F., Liebe, C.C., Markwardt, C.B., Nynka, M., Vogel, J.K., Walton, D.J., Wik, D.R., Alexander, D.M., Cominsky, L.R., Hornschemeier, A.E., Hornstrup, A., Kaspi, V.M., Madejski, G.M., Matt, G., Molendi, S., Smith, D.M., Tomsick, J.A., Ajello, M., Ballantyne, D.R., Baloković, M., Barret, D., Bauer, F.E., Blandford, R.D., Brandt, W.N., Brenneman, L.W., Chiang, J., Chakrabarty, D., Chenevez, J., Comastri, A., Dufour, F., Elvis, M., Fabian, A.C., Farrah, D., Fryer, C.L., Gotthelf, E.V., Grindlay, J.E., Helfand, D.J., Krivonos, R., Meier, D.L., Miller, J.M., Natalucci, L., Ogle, P., Ofek, E.O., Ptak, A., Reynolds, S.P., Rigby, J.R., Tagliaferri, G., Thorsett, S.E., Treister, E., Urry, C.M.: 2013, The Nuclear Spectroscopic Telescope Array (NuSTAR) high-energy X-ray mission. *Astrophys. J.* **770**, 103. DOI. ADS.
- Hasegawa, A., Mima, K., Duong-van, M.: 1985, Plasma distribution function in a superthermal radiation field. *Phys. Rev. Lett.* **54**, 2608. DOI. ADS.
- Heinzl, P.: 1991, A chromospheric response to pulse beam heating. *Solar Phys.* **135**, 65. DOI. ADS.
- Hellinger, P., Matteini, L., Štverák, Š., Trávníček, P.M., Marsch, E.: 2011, Heating and cooling of protons in the fast solar wind between 0.3 and 1 AU: Helios revisited. *J. Geophys. Res.* **116**, 9105. DOI.
- Hellinger, P., Štverák, Š., Trávníček, P.M., Matteini, L., Velli, M.: 2013, Proton thermal energetics in the solar wind: Helios reloaded. *J. Geophys. Res.* DOI.
- Hollweg, J.V.: 1974, On electron heat conduction in the solar wind. *J. Geophys. Res.* **79**, 3845. DOI. ADS.
- Holman, G.D., Sui, L., Schwartz, R.A., Emslie, A.G.: 2003, Electron bremsstrahlung hard X-ray spectra, electron distributions, and energetics in the 2002 July 23 solar flare. *Astrophys. J. Lett.* **595**, L97. DOI. ADS.
- Holman, G.D., Aschwanden, M.J., Aurass, H., Battaglia, M., Grigis, P.C., Kontar, E.P., Liu, W., Saint-Hilaire, P., Zharkova, V.V.: 2011, Implications of X-ray observations for electron acceleration and propagation in solar flares. *Space Sci. Rev.* **159**, 107. DOI. ADS.
- Ishikawa, S.-n., Glesener, L., Christe, S., Ishibashi, K., Brooks, D.H., Williams, D.R., Shimojo, M., Sako, N., Krucker, S.: 2014, Constraining hot plasma in a non-flaring solar active region with FOXSI hard X-ray observations. *Publ. Astron. Soc. Japan* **66**, S15. DOI. ADS.
- Ishikawa, S., Krucker, S., Takahashi, T., Lin, R.P.: 2011, On the relation of above-the-loop and footpoint hard X-ray sources in solar flares. *Astrophys. J.* **737**, 48. DOI. ADS.
- Jeffrey, N.L.S., Fletcher, L., Labrosse, N.: 2016, First evidence of non-Gaussian solar flare EUV spectral line profiles and accelerated non-thermal ion motion. *Astron. Astrophys.* **590**, A99. DOI. ADS.
- Jeffrey, N.L.S., Fletcher, L., Labrosse, N.: 2017, Non-Gaussian velocity distributions in solar flares from extreme ultraviolet lines: a possible diagnostic of ion acceleration. *Astrophys. J.* **836**, 35. DOI. ADS.
- Judge, P.G., Meisner, R.W.: 1994, The 'HAO spectral diagnostics package' (HAOS-Diaper). In: Hunt, J.J. (ed.) *Solar Dynamic Phenomena and Solar Wind Consequences, the Third SOHO Workshop, ESA Special Publication* **373**, 67. ADS.
- Judge, P.G., Woods, T.N., Brekke, P., Rottman, G.J.: 1995, On the failure of standard emission measure analysis for solar extreme-ultraviolet and ultraviolet irradiance spectra. *Astrophys. J. Lett.* **455**, L85. DOI. ADS.
- Judge, P.G., de Pontieu, B., McIntosh, S.W., Olluri, K.: 2012, The connection of type II spicules to the corona. *Astrophys. J.* **746**, 158. DOI. ADS.
- Karlický, M.: 2009, Electron beam-plasma interaction and the return-current formation. *Astrophys. J.* **690**, 189. DOI. ADS.
- Karlický, M.: 2012, The n-distribution of electrons and double layers in the electron-beam-return-current system of solar flares. *Astrophys. J.* **750**, 49. DOI. ADS.

- Karlický, M., Kosugi, T.: 2004, Acceleration and heating processes in a collapsing magnetic trap. *Astron. Astrophys.* **419**, 1159. DOI. ADS.
- Karlický, M., Dzifčáková, E., Dudík, J.: 2012, On the physical meaning of n-distributions in solar flares. *Astron. Astrophys.* **537**, A36. DOI. ADS.
- Kašparová, J., Karlický, M.: 2009, Kappa distribution and hard X-ray emission of solar flares. *Astron. Astrophys.* **497**, L13. DOI. ADS.
- Kašparová, J., Varady, M., Heinzel, P., Karlický, M., Moravec, Z.: 2009, Response of optical hydrogen lines to beam heating. I. Electron beams. *Astron. Astrophys.* **499**, 923. DOI. ADS.
- Keenan, F.P., Dufton, P.L., Kingston, A.E., Cook, J.W.: 1989, Si III line ratios from the high-resolution telescope and spectrograph on board Spacelab 2 – the effects of non-Maxwellian electron distribution functions. *Astrophys. J.* **340**, 1135. DOI. ADS.
- Kepa, A., Sylwester, J., Sylwester, B., Siarkowski, M., Phillips, K.J.H., Kuznetsov, V.D.: 2006, Observations of $1s^2$ – $1s$ np and $1s$ –np lines in RESIK soft X-ray spectra. *Adv. Space Res.* **38**, 1538. DOI. ADS.
- Klimchuk, J.A.: 2006, On solving the coronal heating problem. *Solar Phys.* **234**, 41. DOI. ADS.
- Klimchuk, J.A.: 2015, Key Aspects of Coronal Heating. In: *AAS/AGU Triennial Earth-Sun Summit, AAS/AGU Triennial Earth-Sun Summit 1*, 203.08. ADS.
- Ko, Y.-K., Fisk, L.A., Geiss, J., Gloeckler, G., Guhathakurta, M.: 1997, An empirical study of the electron temperature and heavy ion velocities in the south polar coronal hole. *Solar Phys.* **171**, 345. ADS.
- Kobayashi, K., Cirtain, J., Winebarger, A.R., Korreck, K., Golub, L., Walsh, R.W., De Pontieu, B., DeForest, C., Title, A., Kuzin, S., Savage, S., Beabout, D., Beabout, B., Podgorski, W., Caldwell, D., McCracken, K., Ordway, M., Bergner, H., Gates, R., McKillop, S., Cheimets, P., Platt, S., Mitchell, N., Windt, D.: 2014, The High-Resolution Coronal Imager (Hi-C). *Solar Phys.* **289**, 4393. DOI. ADS.
- Kontar, E.P., Brown, J.C., Emslie, A.G., Hajdas, W., Holman, G.D., Hurford, G.J., Kašparová, J., Mallik, P.C.V., Massone, A.M., McConnell, M.L., Piana, M., Prato, M., Schmahl, E.J., Suarez-Garcia, E.: 2011, Deducing electron properties from hard X-ray observations. *Space Sci. Rev.* **159**, 301. DOI. ADS.
- Kontar, E.P., Bian, N.H., Emslie, A.G., Vilmer, N.: 2014, Turbulent pitch-angle scattering and diffusive transport of hard X-ray-producing electrons in flaring coronal loops. *Astrophys. J.* **780**, 176. DOI. ADS.
- Krucker, S., Battaglia, M.: 2014, Particle densities within the acceleration region of a solar flare. *Astrophys. J.* **780**, 107. DOI. ADS.
- Krucker, S., Lin, R.P.: 2008, Hard X-ray emissions from partially occulted solar flares. *Astrophys. J.* **673**, 1181. DOI. ADS.
- Krucker, S., Battaglia, M., Cargill, P.J., Fletcher, L., Hudson, H.S., MacKinnon, A.L., Masuda, S., Sui, L., Tomczak, M., Veronig, A.L., Vlahos, L., White, S.M.: 2008, Hard X-ray emission from the solar corona. *Astron. Astrophys. Rev.* **16**, 155. DOI. ADS.
- Krucker, S., Hudson, H.S., Glesener, L., White, S.M., Masuda, S., Wuelser, J.-P., Lin, R.P.: 2010, Measurements of the coronal acceleration region of a solar flare. *Astrophys. J.* **714**, 1108. DOI. ADS.
- Krueger, A.: 1979, *Introduction to Solar Radio Astronomy and Radio Physics, Geophysics and Astrophysics Monographs 16*, Reidel, Dordrecht. ADS.
- Kulinová, A., Kašparová, J., Dzifčáková, E., Sylwester, J., Sylwester, B., Karlický, M.: 2011, Diagnostics of non-thermal distributions in solar flare spectra observed by RESIK and RHESSI. *Astron. Astrophys.* **533**, A81. DOI. ADS.
- Kuznetsov, V.D.: 2015, Solar and heliospheric space missions. *Adv. Space Res.* **55**, 879. DOI. ADS.
- Laming, J.M., Lepri, S.T.: 2007, Ion charge states in the fast solar wind: New data analysis and theoretical refinements. *Astrophys. J.* **660**, 1642. DOI. ADS.
- Laming, J.M., Adams, J., Alexander, D., Aschwanden, M., Bailey, C., Bandler, S., et al.: 2010, Science objectives for an X-ray microcalorimeter observing the sun. *arXiv*. ADS, 7 pp.
- Landi, E., Del Zanna, G., Young, P.R., Dere, K.P., Mason, H.E., Landini, M.: 2006, CHIANTI – an atomic database for emission lines. VII. New data for X-rays and other improvements. *Astrophys. J. Suppl.* **162**, 261. DOI.
- Landi, E., Gruesbeck, J.R., Lepri, S.T., Zurbuchen, T.H., Fisk, L.A.: 2012a, Charge state evolution in the solar wind. II. Plasma charge state composition in the inner corona and accelerating fast solar wind. *Astrophys. J.* **761**, 48. DOI. ADS.
- Landi, E., Gruesbeck, J.R., Lepri, S.T., Zurbuchen, T.H., Fisk, L.A.: 2012b, Charge state evolution in the solar wind. Radiative losses in fast solar wind plasmas. *Astrophys. J. Lett.* **758**, L21. DOI. ADS.
- Landi, E., Young, P.R., Dere, K.P., Del Zanna, G., Mason, H.E.: 2013, CHIANTI – an atomic database for emission lines. XIII. Soft X-ray improvements and other changes. *Astrophys. J.* **763**, 86. DOI. ADS.
- Landi, E., Oran, R., Lepri, S.T., Zurbuchen, T.H., Fisk, L.A., van der Holst, B.: 2014, Charge state evolution in the solar wind. III. Model comparison with observations. *Astrophys. J.* **790**, 111. DOI. ADS.
- Landi, S., Pantellini, F.G.E.: 2001, On the temperature profile and heat flux in the solar corona: Kinetic simulations. *Astron. Astrophys.* **372**, 686. DOI. ADS.

- Landi, S., Matteini, L., Pantellini, F.: 2012, On the competition between radial expansion and Coulomb collisions in shaping the electron velocity distribution function: Kinetic simulations. *Astrophys. J.* **760**, 143. DOI. ADS.
- Landi, S., Matteini, L., Pantellini, F.: 2014, Electron heat flux in the solar wind: Are we observing the collisional limit in the 1 AU data? *Astrophys. J. Lett.* **790**, L12. DOI. ADS.
- Lang, J., Kent, B.J., Breeveld, A.A., Breeveld, E.R., Bromage, B.J.I., Hollandt, J., Payne, J., Pike, C.D., Thompson, W.T.: 2000, The laboratory calibration of the SOHO Coronal Diagnostic Spectrometer. *J. Opt. A, Pure Appl. Opt.* **2**, 88. DOI. ADS.
- Lang, J., Kent, B.J., Paustian, W., Brown, C.M., Keyser, C., Anderson, M.R., Case, G.C.R., Chaudry, R.A., James, A.M., Korendyke, C.M., Pike, C.D., Probyn, B.J., Rippington, D.J., Seely, J.F., Tandy, J.A., Whillock, M.C.R.: 2006, Laboratory calibration of the Extreme-Ultraviolet Imaging Spectrometer for the Solar-B satellite. *Appl. Opt.* **45**, 8689. DOI. ADS.
- Lanza, A.F., Spadaro, D., Lanzafame, A.C., Antiochos, S.K., MacNeice, P.J., Spicer, D.S., O'Mullane, M.G.: 2001, *Astrophys. J.* **547**, 1116.
- Le Chat, G., Issautier, K., Meyer-Vernet, N., Zouganelis, I., Moncuquet, M., Hoang, S.: 2010, Quasi-thermal noise spectroscopy: preliminary comparison between kappa and sum of two Maxwellian distributions. In: Maksimovic, M., et al. (eds.) *Twelfth International Solar Wind Conference, AIP Conf. Proc.* **1216**, 316. DOI. ADS.
- Lee, J., Lim, D., Choe, G.S., Kim, K.-S., Jang, M.: 2013, Coronal thick target hard X-ray emissions and radio emissions. *Astrophys. J. Lett.* **769**, L11. DOI. ADS.
- Leenaarts, J., Carlsson, M., Hansteen, V., Rutten, R.J.: 2007, Non-equilibrium hydrogen ionization in 2D simulations of the solar atmosphere. *Astron. Astrophys.* **473**, 625. DOI. ADS.
- Lemaire, J.: 2010, Half a century of kinetic solar wind models. In: Maksimovic, M., et al. (eds.) *Twelfth International Solar Wind Conference, AIP Conf. Proc.* **1216**, 8. DOI. ADS.
- Lemen, J.R., Title, A.M., Akin, D.J., Boerner, P.F., Chou, C., Drake, J.F., Duncan, D.W., Edwards, C.G., Friedlaender, F.M., Heyman, G.F., Hurlburt, N.E., Katz, N.L., Kushner, G.D., Levay, M., Lindgren, R.W., Mathur, D.P., McFeaters, E.L., Mitchell, S., Rehse, R.A., Schrijver, C.J., Springer, L.A., Stern, R.A., Tarbell, T.D., Wuelser, J.-P., Wolfson, C.J., Yanari, C., Bookbinder, J.A., Cheimets, P.N., Caldwell, D., Deluca, E.E., Gates, R., Golub, L., Park, S., Podgorski, W.A., Bush, R.I., Scherrer, P.H., Gummin, M.A., Smith, P., Auker, G., Jerram, P., Pool, P., Soufli, R., Windt, D.L., Beardsley, S., Clapp, M., Lang, J., Waltham, N.: 2012, The Atmospheric Imaging Assembly (AIA) on the Solar Dynamics Observatory (SDO). *Solar Phys.* **275**, 17. DOI. ADS.
- Lepri, S.T., Laming, J.M., Rakowski, C.E., von Steiger, R.: 2012, Spatially dependent heating and ionization in an ICME observed by both ACE and Ulysses. *Astrophys. J.* **760**, 105. DOI. ADS.
- Leubner, M.P.: 2004, Core-halo distribution functions: A natural equilibrium state in generalized thermostatics. *Astrophys. J.* **604**, 469. DOI. ADS.
- Li, G., Kong, X., Zank, G., Chen, Y.: 2013, On the spectral hardening at $\gtrsim 300$ keV in solar flares. *Astrophys. J.* **769**, 22. DOI. ADS.
- Li, T.C., Drake, J.F., Swisdak, M.: 2012, Suppression of energetic electron transport in flares by double layers. *Astrophys. J.* **757**, 20. DOI. ADS.
- Li, T.C., Drake, J.F., Swisdak, M.: 2013, Coronal electron confinement by double layers. *Astrophys. J.* **778**, 144. DOI. ADS.
- Li, T.C., Drake, J.F., Swisdak, M.: 2014, Dynamics of double layers, ion acceleration, and heat flux suppression during solar flares. *Astrophys. J.* **793**, 7. DOI. ADS.
- Lin, R.P.: 2011, Energy release and particle acceleration in flares: Summary and future prospects. *Space Sci. Rev.* **159**, 421. DOI. ADS.
- Lin, R.P., Hudson, H.S.: 1971, 10–100 keV electron acceleration and emission from solar flares. *Solar Phys.* **17**, 412. DOI. ADS.
- Lin, R.P., Dennis, B.R., Hurford, G.J., Smith, D.M., Zehnder, A., Harvey, P.R., Curtis, D.W., Pankow, D., Turin, P., Bester, M., Csillaghy, A., Lewis, M., Madden, N., van Beek, H.F., Appleby, M., Raudorf, T., McTiernan, J., Ramaty, R., Schmahl, E., Schwartz, R., Krucker, S., Abiad, R., Quinn, T., Berg, P., Hashii, M., Sterling, R., Jackson, R., Pratt, R., Campbell, R.D., Malone, D., Landis, D., Barrington-Leigh, C.P., Slassi-Sennou, S., Cork, C., Clark, D., Amato, D., Orwig, L., Boyle, R., Banks, I.S., Shirey, K., Tolbert, A.K., Zarro, D., Snow, F., Thomsen, K., Henneck, R., McHedlishvili, A., Ming, P., Fivian, M., Jordan, J., Wanner, R., Crubb, J., Preble, J., Matranga, M., Benz, A., Hudson, H., Canfield, R.C., Holman, G.D., Crannell, C., Kosugi, T., Emslie, A.G., Vilmer, N., Brown, J.C., Johns-Krull, C., Aschwanden, M., Metcalf, T., Conway, A.: 2002, The Reuven Ramaty High-Energy Solar Spectroscopic Imager (RHESSI). *Solar Phys.* **210**, 3. DOI. ADS.
- Lin, R.P., Krucker, S., Hurford, G.J., Smith, D.M., Hudson, H.S., Holman, G.D., Schwartz, R.A., Dennis, B.R., Share, G.H., Murphy, R.J., Emslie, A.G., Johns-Krull, C., Vilmer, N.: 2003, RHESSI observations

- of particle acceleration and energy release in an intense solar gamma-ray line flare. *Astrophys. J. Lett.* **595**, L69. DOI. ADS.
- Livadiotis, G.: 2015a, Introduction to special section on origins and properties of kappa distributions: Statistical background and properties of kappa distributions in space plasmas. *J. Geophys. Res.* **120**, 1607. DOI. ADS.
- Livadiotis, G.: 2015b, Kappa and q indices: Dependence on the degrees of freedom. *Entropy* **17**, 2062. DOI.
- Livadiotis, G., McComas, D.J.: 2009, Beyond kappa distributions: Exploiting Tsallis statistical mechanics in space plasmas. *J. Geophys. Res.* **114**, 11105. DOI. ADS.
- Livadiotis, G., McComas, D.J.: 2010, Exploring transitions of space plasmas out of equilibrium. *Astrophys. J.* **714**, 971. DOI. ADS.
- Livadiotis, G., McComas, D.J.: 2011, Invariant kappa distribution in space plasmas out of equilibrium. *Astrophys. J.* **741**, 88. DOI. ADS.
- Livadiotis, G., McComas, D.J.: 2013, Understanding kappa distributions: A toolbox for space science and astrophysics. *Space Sci. Rev.* **175**, 183. DOI. ADS.
- Ljepojevic, N.N., MacNeice, P.: 1988, Non-Maxwellian distribution functions in flaring coronal loops – comparison of Landau–Fokker–Planck and BGK solutions. *Solar Phys.* **117**, 123. DOI. ADS.
- Longcope, D.W., Des Jardins, A.C., Carranza-Fulmer, T., Qiu, J.: 2010, A quantitative model of energy release and heating by time-dependent, localized reconnection in a flare with thermal loop-top X-ray source. *Solar Phys.* **267**, 107. DOI. ADS.
- Lynch, B.J., Reinard, A.A., Mulligan, T., Reeves, K.K., Rakowski, C.E., Allred, J.C., Li, Y., Laming, J.M., MacNeice, P.J., Linker, J.A.: 2011, Ionic composition structure of coronal mass ejections in axisymmetric magnetohydrodynamic models. *Astrophys. J.* **740**, 112. DOI. ADS.
- Mackovjak, Š., Džifčáková, E., Dudík, J.: 2013, On the possibility to diagnose the Non-Maxwellian κ -distributions from the Hinode/EIS EUV spectra. *Solar Phys.* **282**, 263. DOI. ADS.
- Mackovjak, Š., Džifčáková, E., Dudík, J.: 2014, Differential emission measure analysis of active region cores and quiet Sun for the non-Maxwellian κ -distributions. *Astron. Astrophys.* **564**, A130. DOI. ADS.
- MacNiece, P.J., Olson, K.M., Mobarry, C., de Fainchtein, R., Packer, C.: 2000., *Comput. Phys. Commun.* **126**, 330.
- Maksimovic, M., Pierrard, V., Lemaire, J.F.: 1997, A kinetic model of the solar wind with Kappa distribution functions in the corona. *Astron. Astrophys.* **324**, 725. ADS.
- Maksimovic, M., Pierrard, V., Riley, P.: 1997, Ulysses electron distributions fitted with Kappa functions. *Geophys. Res. Lett.* **24**, 1151. DOI. ADS.
- Maksimovic, M., Hoang, S., Meyer-Vernet, N., Moncuquet, M., Bougeret, J.-L., Phillips, J.L., Canu, P.: 1995, Solar wind electron parameters from quasi-thermal noise spectroscopy and comparison with other measurements on Ulysses. *J. Geophys. Res.* **100**, 19881. DOI. ADS.
- Maksimovic, M., Issautier, K., Meyer-Vernet, N., Perche, C., Moncuquet, M., Zouganelis, I., Bale, S.D., Vilmer, N., Bougeret, J.-L.: 2005, Solar wind electron temperature and density measurements on the Solar Orbiter with thermal noise spectroscopy. *Adv. Space Res.* **36**, 1471. DOI. ADS.
- Marsch, E.: 2006, Kinetic physics of the solar corona and solar wind. *Living Rev. Solar Phys.* **3**, 1. DOI. ADS.
- Marsch, E., Rosenbauer, H., Schwenn, R., Muehlhaeuser, K.-H., Neubauer, F.M.: 1982a, Solar wind helium ions – observations of the HELIOS solar probes between 0.3 and 1 AU. *J. Geophys. Res.* **87**, 35.
- Marsch, E., Schwenn, R., Rosenbauer, H., Muehlhaeuser, K.-H., Pilipp, W., Neubauer, F.M.: 1982b, Solar wind protons – three-dimensional velocity distributions and derived plasma parameters measured between 0.3 and 1 AU. *J. Geophys. Res.* **87**, 52.
- Martínez-Sykora, J., De Pontieu, B., Hansteen, V.H., Gudiksen, B.: 2016, Time dependent nonequilibrium ionization of transition region lines observed with IRIS. *Astrophys. J.* **817**, 46. DOI. ADS.
- Maruca, B.A., Kasper, J.C., Gary, S.P.: 2012, Instability-driven limits on helium temperature anisotropy in the solar wind: Observations and linear Vlasov analysis. *Astrophys. J.* **748**, 137. DOI.
- Mason, H.E., Monsignori Fossi, B.C.: 1994, Spectroscopic diagnostics in the VUV for solar and stellar plasmas. *Astron. Astrophys. Rev.* **6**, 123. DOI. ADS.
- Masuda, S., Kosugi, T., Hara, H., Tsuneta, S., Ogawara, Y.: 1994, A loop-top hard X-ray source in a compact solar flare as evidence for magnetic reconnection. *Nature* **371**, 495. DOI. ADS.
- Matteini, L., Hellinger, P., Landi, S., Trávníček, P., Velli, M.: 2012, Ion kinetics in the solar wind: Coupling global expansion to local microphysics. *Space Sci. Rev.* **172**, 373. DOI.
- Matteini, L., Hellinger, P., Goldstein, B.E., Landi, S., Velli, M., Neugebauer, M.: 2013, Signatures of kinetic instabilities in the solar wind. *J. Geophys. Res.* **118**, 2771. DOI.
- Matteini, L., Hellinger, P., Schwartz, S.J., Landi, S.: 2015, Fire hose instability driven by alpha particle temperature anisotropy. *Astrophys. J.* **812**, 13. DOI.
- Mazzotta, P., Mazzitelli, G., Colafrancesco, S., Vittorio, N.: 1998, Ionization balance for optically thin plasmas: Rate coefficients for all atoms and ions of the elements H to Ni. *Astron. Astrophys. Suppl.* **133**, 403. DOI. ADS.

- McWhirter, R.W.P., Summers, H.P.: 1984, Atomic radiation from low density plasma. In: *Applied Atomic Collision Physics, vol. 2. Plasmas*, 51. DOI.
- Mewe, R., Gronenschild, E.H.B.M., van den Oord, G.H.J.: 1985, Calculated X-radiation from optically thin plasmas. *V. Astron. Astrophys. Suppl.* **62**, 197. ADS.
- Mewe, R., Lemen, J.R., Peres, G., Schrijver, J., Serio, S.: 1985, Solar X-ray spectrum simulations for flaring loop models with emphasis on transient ionization effects during the impulsive phase. *Astron. Astrophys.* **152**, 229. ADS.
- Meyer-Vernet, N.: 1993, Aspects of Debye shielding. *Am. J. Phys.* **61**, 249. DOI.
- Meyer-Vernet, N.: 1999, How does the solar wind blow? A simple kinetic model. *Eur. J. Phys.* **20**, 167. DOI. ADS.
- Meyer-Vernet, N.: 2001, Large scale structure of planetary environments: The importance of not being Maxwellian. *Planet. Space Sci.* **49**, 247. DOI. ADS.
- Meyer-Vernet, N.: 2007, *Basics of the Solar Wind*, Cambridge University Press, Cambridge ADS.
- Meyer-Vernet, N., Issautier, K.: 1998, Electron temperature in the solar wind: Generic radial variation from kinetic collisionless models. *J. Geophys. Res.* **103**, 29705. DOI. ADS.
- Meyer-Vernet, N., Perche, C.: 1989, Tool kit for antennae and thermal noise near the plasma frequency. *J. Geophys. Res.* **94**, 2405. DOI. ADS.
- Meyer-Vernet, N., Hoang, S., Issautier, K., Maksimovic, M., Manning, R., Moncuquet, M., Stone, R.G.: 1998, Measuring plasma parameters with thermal noise spectroscopy. In: Pfaff, R., et al. (eds.) *Measurement Techniques in Space Plasmas: Fields, Geophys. Monograph Ser:* **103**, 205. ADS.
- Miller, J.A., Cargill, P.J., Emslie, A., Holamn, G.D., Dennis, B.R., Larosa, T.N., Winglee, R.M., Benka, S.G., Tsuneta, S.: 1997, Critical issues for understanding particle acceleration in impulsive solar flares. *J. Geophys. Res.* **102**, 1463. ADS.
- Milligan, R.O., Kennedy, M.B., Mathioudakis, M., Keenan, F.P.: 2012, Time-dependent density diagnostics of solar flare plasmas using SDO/EVE. *Astrophys. J. Lett.* **755**, L16. DOI. ADS.
- Minoshima, T., Masuda, S., Miyoshi, Y., Kusano, K.: 2011, Coronal electron distribution in solar flares: Drift-kinetic model. *Astrophys. J.* **732**, 111. DOI. ADS.
- Moncuquet, M., Matsumoto, H., Bougeret, J.-L., Blomberg, L.G., Issautier, K., Kasaba, Y., Kojima, H., Maksimovic, M., Meyer-Vernet, N., Zarka, P.: 2006, The radio waves and thermal electrostatic noise spectroscopy (SORBET) experiment on BEPICOLOMBO/MMO/PWI: Scientific objectives and performance. *Adv. Space Res.* **38**, 680. DOI. ADS.
- Nicholls, D.C., Dopita, M.A., Sutherland, R.S.: 2012, Resolving the electron temperature discrepancies in H II regions and planetary nebulae: κ -distributed electrons. *Astrophys. J.* **752**, 148. DOI. ADS.
- Nicolaou, G., Livadiotis, G.: 2016, Misestimation of temperature when applying Maxwellian distributions to space plasmas described by kappa distributions. *Astrophys. Space Sci.* **361**, 359. DOI. ADS.
- Nikolić, D., Gorczyca, T.W., Korista, K.T., Ferland, G.J., Badnell, N.R.: 2013, Suppression of dielectronic recombination due to finite density effects. *Astrophys. J.* **768**, 82. DOI. ADS.
- Nishizuka, N., Shibata, K.: 2013, Fermi acceleration in plasmoids interacting with fast shocks of reconnection via fractal reconnection. *Phys. Rev. Lett.* **110**(5), 051101. DOI. ADS.
- Noci, G., Spadaro, D., Zappala, R.A., Antiochos, S.K.: 1989, Mass flows and the ionization states of coronal loops. *Astrophys. J.* **338**, 1131. DOI. ADS.
- Oka, M., Phan, T.-D., Krucker, S., Fujimoto, M., Shinohara, I.: 2010, Electron acceleration by multi-island coalescence. *Astrophys. J.* **714**, 915. DOI. ADS.
- Oka, M., Ishikawa, S., Saint-Hilaire, P., Krucker, S., Lin, R.P.: 2013, Kappa distribution model for hard X-ray coronal sources of solar flares. *Astrophys. J.* **764**, 6. DOI. ADS.
- Oka, M., Krucker, S., Hudson, H.S., Saint-Hilaire, P.: 2015, Electron energy partition in the above-the-looptop solar hard X-ray sources. *Astrophys. J.* **799**, 129. DOI. ADS.
- Olbert, S.: 1968, Summary of Experimental Results from M.I.T. Detector on IMP-1. In: Carovillano, R.D.L., McClay, J.F. (eds.) *Physics of the Magnetosphere, Astrophys. Spa. Sci. Lib.* **10**, 641. DOI. ADS.
- Olbert, S.: 1981, Inferences about the solar wind dynamics from observed distributions of electrons and ions. In: Guyenne, T.D., Lévy, G. (eds.) *ESA Special Publication, ESA SP-161*, 135. ADS.
- Olluri, K., Gudiksen, B.V., Hansteen, V.H.: 2013a, Non-equilibrium ionization effects on the density line ratio diagnostics of O IV. *Astrophys. J.* **767**, 43. DOI. ADS.
- Olluri, K., Gudiksen, B.V., Hansteen, V.H.: 2013b, Non-equilibrium ionization in the Bifrost stellar atmosphere code. *Astron. J.* **145**, 72. DOI. ADS.
- Olluri, K., Gudiksen, B.V., Hansteen, V.H., De Pontieu, B.: 2015, Synthesized spectra of optically thin emission lines. *Astrophys. J.* **802**, 5. DOI. ADS.
- Oraevsky, V.N., Galeev, A.A., Kuznetsov, V.D., Zelenyi, L.M.: 2001, Orbiter and Russian Aviation and Space Agency Interhelioprobe. In: *Inter Solar Encounter. Proc. First Solar Orbiter Workshop, ESA SP-493*, 95. ADS.

- Oran, R., van der Holst, B., Landi, E., Jin, M., Sokolov, I.V., Gombosi, T.I.: 2013, A global wave-driven magnetohydrodynamic solar model with a unified treatment of open and closed magnetic field topologies. *Astrophys. J.* **778**, 176. DOI. ADS.
- Oran, R., Landi, E., van der Holst, B., Lepri, S.T., Vásquez, A.M., Nuevo, F.A., Frazin, R., Manchester, W., Sokolov, I., Gombosi, T.I.: 2015, A steady-state picture of solar wind acceleration and charge state composition derived from a global wave-driven MHD model. *Astrophys. J.* **806**, 55. DOI. ADS.
- Owocki, S., Townsend, R., Ud-Doula, A.: 1999, Charge states of C and O from coronal holes: Non-Maxwellian distribution vs. unequal ion speeds. In: Habbal, S.R., Halas, C.D. (eds.) *The solar wind nine conference*, American Institute of Physics Conference Series **471**, 263. DOI.
- Owocki, S.P., Scudder, J.D.: 1983, The effect of a non-Maxwellian electron distribution on oxygen and iron ionization balances in the solar corona. *Astrophys. J.* **270**, 758. DOI. ADS.
- Parker, E.N.: 1983, Magnetic neutral sheets in evolving fields – Part two – Formation of the solar corona. *Astrophys. J.* **264**, 642. DOI.
- Parker, E.N.: 1988, Nanoflares and the solar X-ray corona. *Astrophys. J.* **330**, 474. DOI.
- Parker, E.N.: 2010, Kinetic and hydrodynamic representations of coronal expansion and the solar wind. In: Maksimovic, M., et al. (eds.) *Twelfth International Solar Wind Conference, AIP Conf. Proc.* **1216**, 3. DOI. ADS.
- Pesnell, W.D., Thompson, B.J., Chamberlin, P.C.: 2012, The Solar Dynamics Observatory (SDO). *Solar Phys.* **275**, 3. DOI. ADS.
- Peter, H., Tian, H., Curdt, W., Schmit, D., Innes, D., De Pontieu, B., Lemen, J., Title, A., Boerner, P., Hurlburt, N., Tarbell, T.D., Wuelser, J.P., Martínez-Sykora, J., Kleint, L., Golub, L., McKillip, S., Reeves, K.K., Saar, S., Testa, P., Kankelborg, C., Jaeggli, S., Carlsson, M., Hansteen, V.: 2014, Hot explosions in the cool atmosphere of the Sun. *Science* **346**, 1255726. DOI. ADS.
- Petkaki, P., MacKinnon, A.L.: 2011, Acceleration of charged particles by fluctuating and steady electric fields in a X-type magnetic field. *Adv. Space Res.* **48**, 884. DOI. ADS.
- Phillips, K.J.H., Feldman, U., Landi, E.: 2008, *Ultraviolet and X-ray Spectroscopy of the Solar Atmosphere*, Cambridge University Press, Cambridge. ADS.
- Phillips, K.J.H., Bhatia, A.K., Mason, H.E., Zarro, D.M.: 1996, High coronal electron densities in a solar flare from Fe XXI and Fe XXII X-ray line measurements. *Astrophys. J.* **466**, 549. DOI. ADS.
- Pierrard, V., Lazar, M.: 2010, Kappa distributions: Theory and applications in space plasmas. *Solar Phys.* **267**, 153. DOI. ADS.
- Pierrard, V., Pieters, M.: 2014, Coronal heating and solar wind acceleration for electrons, protons, and minor ions obtained from kinetic models based on kappa distributions. *J. Geophys. Res.* **119**, 9441. DOI. ADS.
- Pierrard, V., Lazar, M., Schlickeiser, R.: 2011, Evolution of the electron distribution function in the whistler wave turbulence of the solar wind. *Solar Phys.* **269**, 421. DOI. ADS.
- Pierrard, V., Maksimovic, M., Lemaire, J.: 1999, Electron velocity distribution functions from the solar wind to the corona. *J. Geophys. Res.* **104**, 17021. DOI. ADS.
- Pierrard, V., Lazar, M., Poedts, S., Štverák, Š., Maksimovic, M., Trávníček, P.M.: 2016, The electron temperature and anisotropy in the solar wind. Comparison of the core and halo populations. *Solar Phys.* **291**, 2165. DOI. ADS.
- Pilipp, W.G., Muehlhaeuser, K.-H., Miggenrieder, H., Montgomery, M.D., Rosenbauer, H.: 1987, Characteristics of electron velocity distribution functions in the solar wind derived from the HELIOS plasma experiment. *J. Geophys. Res.* **92**, 1075. DOI. ADS.
- Pinfield, D.J., Keenan, F.P., Mathioudakis, M., Phillips, K.J.H., Curdt, W., Wilhelm, K.: 1999, Evidence for non-Maxwellian electron energy distributions in the solar transition region: Si III line ratios from SUMER. *Astrophys. J.* **527**, 1000. DOI. ADS.
- Pinto, R.F., Gordovskyy, M., Browning, P.K., Vilmer, N.: 2016, Thermal and non-thermal emission from reconnecting twisted coronal loops. *Astron. Astrophys.* **585**, A159. DOI. ADS.
- Polito, V., Del Zanna, G., Dudík, J., Mason, H.E., Giunta, A., Reeves, K.K.: 2016a, Density diagnostics derived from the O IV and S IV intercombination lines observed by IRIS. *Astron. Astrophys.* **594**, A64. DOI. ADS.
- Polito, V., Reep, J.W., Reeves, K.K., Simões, P.J.A., Dudík, J., Del Zanna, G., Mason, H.E., Golub, L.: 2016b, Simultaneous IRIS and Hinode/EIS observations and modelling of the 2014 October 27 X2.0 class flare. *Astrophys. J.* **816**, 89. DOI. ADS.
- Priest, E., Forbes, T.: 2000, *Magnetic Reconnection*, Cambridge University Press, Cambridge. ADS.
- Ralchenko, Y., Feldman, U., Doschek, G.A.: 2007, Is there a high-energy particle population in the quiet solar corona? *Astrophys. J.* **659**, 1682. DOI. ADS.
- Raymond, J.C.: 1990, Predicted extreme-ultraviolet and X-ray spectrum of a microflare-heated corona. *Astrophys. J.* **365**, 387. DOI. ADS.
- Raymond, J.C., Dupree, A.K.: 1978, C III density diagnostics in nonequilibrium plasmas. *Astrophys. J.* **222**, 379. DOI. ADS.

- Reale, F., Orlando, S.: 2008, Nonequilibrium of ionization and the detection of hot plasma in nanoflare-heated coronal loops. *Astrophys. J.* **684**, 715. DOI. ADS.
- Reep, J.W., Russell, A.J.B.: 2016, Alfvénic wave heating of the upper chromosphere in flares. *Astrophys. J. Lett.* **818**, L20. DOI. ADS.
- Reep, J.W., Bradshaw, S.J., Alexander, D.: 2015, Optimal electron energies for driving chromospheric evaporation in solar flares. *Astrophys. J.* **808**, 177. DOI. ADS.
- Reep, J.W., Bradshaw, S.J., McAteer, R.T.J.: 2013, On the sensitivity of the GOES flare classification to properties of the electron beam in the thick-target model. *Astrophys. J.* **778**, 76. DOI. ADS.
- Régnier, S., Alexander, C.E., Walsh, R.W., Winebarger, A.R., Cirtain, J., Golub, L., Korreck, K.E., Mitchell, N., Platt, S., Weber, M., De Pontieu, B., Title, A., Kobayashi, K., Kuzin, S., DeForest, C.E.: 2014, Sparkling extreme-ultraviolet bright dots observed with Hi-C. *Astrophys. J.* **784**, 134. DOI. ADS.
- Rodkin, D., Goryaev, F., Pagano, P., Gibb, G., Slemzin, V., Shugay, Y., Veselovsky, I., Mackay, D.H.: 2017, Origin and ion charge state evolution of solar wind transients during 4–7 August 2011. *Solar Phys.* **292**, 90. DOI. ADS.
- Roussel-Dupré, R.: 1980a, Non-Maxwellian velocity distribution functions associated with steep temperature gradients in the solar transition region. I – Estimate of the electron velocity distribution functions. *Solar Phys.* **68**, 243. DOI. ADS.
- Roussel-Dupré, R.: 1980b, Non-Maxwellian velocity distribution functions associated with steep temperature gradients in the solar transition region. II. The effect of non-Maxwellian electron distribution functions on ionization equilibrium calculations for carbon, nitrogen and oxygen. *Solar Phys.* **68**, 265. DOI. ADS.
- Saint-Hilaire, P., Krucker, S., Lin, R.P.: 2008, A statistical survey of hard X-ray spectral characteristics of solar flares with two footpoints. *Solar Phys.* **250**, 53. DOI. ADS.
- Sakao, T.: 1994, Characteristics of solar flare hard X-ray sources as revealed with the Hard X-ray Telescope aboard the Yohkoh satellite. PhD thesis, University of Tokyo. ADS.
- Salem, C., Bosqued, J.-M., Larson, D.E., Mangeney, A., Maksimovic, M., Perche, C., Lin, R.P., Bougeret, J.-L.: 2001, Determination of accurate solar wind electron parameters using particle detectors and radio wave receivers. *J. Geophys. Res.* **106**, 21701. DOI. ADS.
- Schmelz, J.T., Winebarger, A.R.: 2015, What can observations tell us about coronal heating? *Phil. Trans. Roy. Soc. London Ser. A, Math. Phys. Sci.* **373**, 20140257. DOI. ADS.
- Schmelz, J.T., Kashyap, V.L., Saar, S.H., Dennis, B.R., Grigis, P.C., Lin, L., De Luca, E.E., Holman, G.D., Golub, L., Weber, M.A.: 2009, Some like it hot: Coronal heating observations from Hinode X-ray telescope and RHESSI. *Astrophys. J.* **704**, 863. DOI. ADS.
- Scudder, J.D.: 1992a, On the causes of temperature change in inhomogeneous low-density astrophysical plasmas. *Astrophys. J.* **398**, 299. DOI. ADS.
- Scudder, J.D.: 1992b, Why all stars should possess circumstellar temperature inversions. *Astrophys. J.* **398**, 319. DOI. ADS.
- Scudder, J.D., Karimabadi, H.: 2013, Ubiquitous non-thermals in astrophysical plasmas: Restating the difficulty of maintaining Maxwellians. *Astrophys. J.* **770**, 26. DOI. ADS.
- Scudder, J.D., Olbert, S.: 1979, A theory of local and global processes which affect solar wind electrons. I – The origin of typical 1 AU velocity distribution functions – steady state theory. *J. Geophys. Res.* **84**, 2755. DOI. ADS.
- Scudder, J.D., Olbert, S.: 1983, The collapse of the local, Spitzer–Haerm formulation and a global-local generalization for heat flow in an inhomogeneous, fully ionized plasma. In: *NASA Conf. Publ., NASA Conference Publication* **228**, 163. ADS.
- Seely, J.F., Feldman, U., Doschek, G.A.: 1987, Observation of nonthermal energy distributions during the impulsive phase of solar flares. *Astrophys. J.* **319**, 541. DOI. ADS.
- Serio, S., Reale, F., Jakimiec, J., Sylwester, B., Sylwester, J.: 1991, Dynamics of flaring loops. I – Thermodynamic decay scaling laws. *Astron. Astrophys.* **241**, 197. ADS.
- Shen, C., Reeves, K.K., Raymond, J.C., Murphy, N.A., Ko, Y.-K., Lin, J., Mikić, Z., Linker, J.A.: 2013, Non-equilibrium ionization modeling of the current sheet in a simulated solar eruption. *Astrophys. J.* **773**, 110. DOI. ADS.
- Shoub, E.C.: 1983, Invalidation of local thermodynamic equilibrium for electrons in the solar transition region. I – Fokker–Planck results. *Astrophys. J.* **266**, 339. DOI. ADS.
- Siarkowski, M., Sylwester, J., Bakała, J., Szaforz, Ż., Kowaliński, M., Kordylewski, Z., Płoceniak, S., Podgórski, P., Sylwester, B., Trzebiński, W., Stęślicki, M., Phillips, K.J.H., Dudnik, O.V., Kurbatov, E., Kuznetsov, V.D., Kuzin, S., Zimovets, I.V.: 2016, ChemiX: a Bragg crystal spectrometer for the Interhelioprobe interplanetary mission. *Exp. Astron.* **41**, 327. DOI. ADS.
- Simões, P.J.A., Kontar, E.P.: 2013, Implications for electron acceleration and transport from non-thermal electron rates at looptop and footpoint sources in solar flares. *Astron. Astrophys.* **551**, A135. DOI. ADS.
- Smith, R.K., Hughes, J.P.: 2010, Ionization equilibrium timescales in collisional plasmas. *Astrophys. J.* **718**, 583. DOI. ADS.

- Somov, B.V., Kosugi, T.: 1997, Collisionless reconnection and high-energy particle acceleration in solar flares. *Astrophys. J.* **485**, 859. [ADS](#).
- Spadaro, D., Leto, P., Antiochos, S.K.: 1994, Observational tests for nonequilibrium ionization in the solar corona. *Astrophys. J.* **427**, 453. [DOI](#). [ADS](#).
- Spitzer, L., Härm, R.: 1953, Transport phenomena in completely ionised gas. *Phys. Rev.* **89**, 977. [DOI](#).
- Stone, R.G., Bougeret, J.L., Caldwell, J., Canu, P., de Conchy, Y., Cornilleau-Wehrin, N., Desch, M.D., Fainberg, J., Goetz, K., Goldstein, M.L.: 1992, The unified radio and plasma wave investigation. *Astron. Astrophys. Suppl.* **92**, 291. [ADS](#).
- Strong, K.T.: 1978, PhD thesis, Univ. College London. [ADS](#).
- Sui, L., Holman, G.D.: 2003, Evidence for the formation of a large-scale current sheet in a solar flare. *Astrophys. J. Lett.* **596**, L251. [DOI](#). [ADS](#).
- Summers, H.P.: 1974a, Appleton Laboratory Internal Memorandum IM367 & Re-issued with Improvements as AL-R-5.
- Summers, H.P.: 1974b, The ionization equilibrium of hydrogen-like to argon-like ions of elements. *Mon. Not. Roy. Astron. Soc.* **169**, 663. [DOI](#). [ADS](#).
- Summers, H.P., Dickson, W.J., O'Mullane, M.G., Badnell, N.R., Whiteford, A.D., Brooks, D.H., Lang, J., Loch, S.D., Griffin, D.C.: 2006, Ionization state, excited populations and emission of impurities in dynamic finite density plasmas: I. The generalized collisional radiative model for light elements. *Plasma Phys. Control. Fusion* **48**, 263. [DOI](#). [ADS](#).
- Sun, J.Q., Cheng, X., Ding, M.D.: 2014, Differential emission measure analysis of a limb solar flare on 2012 July 19. *Astrophys. J.* **786**, 73. [DOI](#). [ADS](#).
- Susino, R., Lanzafame, A.C., Lanza, A.F., Spadaro, D.: 2010, Signatures of impulsive localized heating in the temperature distribution of multi-stranded coronal loops. *Astrophys. J.* **709**, 499. [DOI](#). [ADS](#).
- Suzuki, S., Dulk, G.A.: 1985, In: McLean, D.J., Labrum, N.R. (eds.) *Bursts of Type III and Type V*, 289. [ADS](#).
- Sylwester, J., Sylwester, B., Phillips, K.J.H.: 2008, RESIK observations of helium-like argon X-ray line emission in solar flares. *Astrophys. J. Lett.* **681**, L117. [DOI](#). [ADS](#).
- Sylwester, J., Gaicki, I., Kordylewski, Z., Kowaliński, M., Nowak, S., Płocieniak, S., Siarkowski, M., Sylwester, B., Trzebiński, W., Bakała, J., Culhane, J.L., Whyndham, M., Bentley, R.D., Guttridge, P.R., Phillips, K.J.H., Lang, J., Brown, C.M., Doschek, G.A., Kuznetsov, V.D., Oraevsky, V.N., Stepanov, A.I., Lisin, D.V.: 2005, Resik: A bent crystal X-ray spectrometer for studies of solar coronal plasma composition. *Solar Phys.* **226**, 45. [DOI](#). [ADS](#).
- Sylwester, J., Kordylewski, Z., Płocieniak, S., Siarkowski, M., et al.: 2015, X-ray flare spectra from the DIOGENESS Spectrometer and its concept applied to ChemiX on the InterhelioProbe Spacecraft. *Solar Phys.* **290**, 3683. [DOI](#). [ADS](#).
- Tajfirouze, E., Reale, F., Peres, G., Testa, P.: 2016, EUV flickering of solar coronal loops: A new diagnostic of coronal heating. *Astrophys. J. Lett.* **817**, L11. [DOI](#). [ADS](#).
- Tanaka, K., Watannabe, T., Nishi, K., Akita, K.: 1982, High-resolution solar flare X-ray spectra obtained with rotating spectrometers on the HINOTORI satellite. *Astrophys. J. Lett.* **254**, L59. [DOI](#). [ADS](#).
- Tandberg-Hanssen, E., Emslie, A.G.: 1988, *The Physics of Solar Flares*, Cambridge University Press, Cambridge. [ADS](#).
- Tao, J., Wang, L., Zong, Q., Li, G., Salem, C.S., Wimmer-Schweingruber, R.F., He, J., Tu, C., Bale, S.D.: 2016, Quiet-time suprathermal ($\sim 0.1 - 1.5$ keV) electrons in the solar wind. *Astrophys. J.* **820**, 22. [DOI](#). [ADS](#).
- Teriaca, L., Andretta, V., Auchère, F., Brown, C.M., Buchlin, E., Cauzzi, G., Culhane, J.L., Curdt, W., Davila, J.M., Del Zanna, G., Doschek, G.A., Fineschi, S., Fludra, A., Gallagher, P.T., Green, L., Harra, L.K., Imada, S., Innes, D., Kliem, B., Korendyke, C., Mariska, J.T., Martínez-Pillet, V., Parenti, S., Pat-sourakos, S., Peter, H., Poletto, L., Rutten, R.J., Schühle, U., Siemer, M., Shimizu, T., Socas-Navarro, H., Solanki, S.K., Spadaro, D., Trujillo-Bueno, J., Tsuneta, S., Dominguez, S.V., Vial, J.-C., Walsh, R., Warren, H.P., Wiegelmann, T., Winter, B., Young, P.: 2012, LEMUR: Large European module for solar Ultraviolet Research. European contribution to JAXA's Solar-C mission. *Exp. Astron.* **34**, 273. [DOI](#). [ADS](#).
- Testa, P., De Pontieu, B., Martínez-Sykora, J., DeLuca, E., Hansteen, V., Cirtain, J., Winebarger, A., Golub, L., Kobayashi, K., Korreck, K., Kuzin, S., Walsh, R., DeForest, C., Title, A., Weber, M.: 2013, Observing coronal nanoflares in active region moss. *Astrophys. J. Lett.* **770**, L1. [DOI](#). [ADS](#).
- Testa, P., De Pontieu, B., Allred, J., Carlsson, M., Reale, F., Daw, A., Hansteen, V., Martínez-Sykora, J., Liu, W., DeLuca, E.E., Golub, L., McKillop, S., Reeves, K., Saar, S., Tian, H., Lemen, J., Title, A., Boerner, P., Hurlburt, N., Tarbell, T.D., Wuelser, J.P., Kleint, L., Kankelborg, C., Jaeggli, S.: 2014, Evidence of nonthermal particles in coronal loops heated impulsively by nanoflares. *Science* **346**, 1255724. [DOI](#). [ADS](#).

- Tian, H., Kleint, L., Peter, H., Weber, M., Testa, P., DeLuca, E., Golub, L., Schanche, N.: 2014, Observations of subarcsecond bright dots in the transition region above sunspots with the Interface Region Imaging Spectrograph. *Astrophys. J. Lett.* **790**, L29. DOI. ADS.
- Tsallis, C.: 1988, Possible generalization of Boltzmann–Gibbs statistics. *J. Stat. Phys.* **52**, 479. DOI. ADS.
- Tsallis, C.: 2009, *Introduction to Nonextensive Statistical Mechanics*, Springer, New York.
- Tsuneta, S.: 1996, Structure and dynamics of magnetic reconnection in a solar flare: Erratum. *Astrophys. J.* **464**, 1055. DOI. ADS.
- Tsuneta, S., Naito, T.: 1998, Fermi acceleration at the fast shock in a solar flare and the impulsive loop-top hard X-ray source. *Astrophys. J. Lett.* **495**, L67. DOI. ADS.
- Vasyliunas, V.M.: 1968a, A survey of low-energy electrons in the evening sector of the magnetosphere with OGO 1 and OGO 3. *J. Geophys. Res.* **73**, 2839. DOI. ADS.
- Vasyliunas, V.M.: 1968b, Low-energy electrons in the magnetosphere as observed by OGO-1 and OGO-3. In: Carovillano, R.D.L., McClay, J.F. (eds.) *Physics of the Magnetosphere*, *Astrophys. Spa. Sci. Lib.* **10**, 622. ADS.
- Veck, N.J., Strong, K.T., Jordan, C., Simnett, G.M., Cargill, P.J., Priest, E.R.: 1984, The development and cooling of a solar limb-flare. *Mon. Not. Roy. Astron. Soc.* **210**, 443. DOI. ADS.
- Veronig, A.M., Brown, J.C.: 2004, A coronal thick-target interpretation of two hard X-ray loop events. *Astrophys. J. Lett.* **603**, L117. DOI. ADS.
- Viall, N.M., Klimchuk, J.A.: 2011, Patterns of nanoflare storm heating exhibited by an active region observed with Solar Dynamics Observatory/Atmospheric Imaging Assembly. *Astrophys. J.* **738**, 24. DOI. ADS.
- Vilmer, N., MacKinnon, A.L., Hurford, G.J.: 2011, Properties of energetic ions in the solar atmosphere from γ -ray and neutron observations. *Space Sci. Rev.* **159**, 167. DOI. ADS.
- Vissers, G.J.M., Rouppe van der Voort, L.H.M., Rutten, R.J., Carlsson, M., De Pontieu, B.: 2015, Ellerman bombs at high resolution. III. Simultaneous observations with IRIS and SST. *Astrophys. J.* **812**, 11. DOI. ADS.
- Vocks, C.: 2012, Kinetic models for whistler wave scattering of electrons in the solar corona and wind. *Space Sci. Rev.* **172**, 303. DOI. ADS.
- Vocks, C., Dzifčáková, E., Mann, G.: 2016, Suprathermal electron distributions in the solar transition region. *Astron. Astrophys.* **596**, A41. DOI.
- Vocks, C., Mann, G., Rausche, G.: 2008, Formation of suprathermal electron distributions in the quiet solar corona. *Astron. Astrophys.* **480**, 527. DOI. ADS.
- Vocks, C., Salem, C., Lin, R.P., Mann, G.: 2005, Electron halo and strahl formation in the solar wind by resonant interaction with whistler waves. *Astrophys. J.* **627**, 540. DOI. ADS.
- Wannawichian, S., Ruffolo, D., Kartavykh, Y.Y.: 2003, Ionization fractions of slow ions in a plasma with kappa distributions for the electron velocity. *Astrophys. J. Suppl.* **146**, 443. DOI. ADS.
- Wargelin, B.J., Beiersdorfer, P., Brown, G.V.: 2008, EBIT charge-exchange measurements and astrophysical applications. *Can. J. Phys.* **86**, 151. DOI. ADS.
- Warren, H.P., Ugarte-Urra, I., Landi, E.: 2014, The absolute calibration of the EUV imaging spectrometer on Hinode. *Astrophys. J. Suppl.* **213**, 11. DOI. ADS.
- Warren, H.P., Winebarger, A.R., Brooks, D.H.: 2012, A systematic survey of high-temperature emission in solar active regions. *Astrophys. J.* **759**, 141. DOI. ADS.
- Watanabe, T., Hara, H., Yamamoto, N., Kato, D., Sakaue, H.A., Murakami, I., Kato, T., Nakamura, N., Young, P.R.: 2009, Fe XIII density diagnostics in the EIS observing wavelengths. *Astrophys. J.* **692**, 1294. DOI. ADS.
- Wedemeyer-Böhm, S., Carlsson, M.: 2011, Non-equilibrium calcium ionisation in the solar atmosphere. *Astron. Astrophys.* **528**, A1. DOI. ADS.
- West, M.J., Bradshaw, S.J., Cargill, P.J.: 2008, On the lifetime of hot coronal plasmas arising from nanoflares. *Solar Phys.* **252**, 89. DOI. ADS.
- White, S.M., Benz, A.O., Christe, S., Fárník, F., Kundu, M.R., Mann, G., Ning, Z., Raulin, J.-P., Silva-Válio, A.V.R., Saint-Hilaire, P., Vilmer, N., Warmuth, A.: 2011, The relationship between solar radio and hard X-ray emission. *Space Sci. Rev.* **159**, 225. DOI. ADS.
- Wilhelm, K., Curdt, W., Marsch, E., Schühle, U., Lemaire, P., Gabriel, A., Vial, J.-C., Grewing, M., Huber, M.C.E., Jordan, S.D., Poland, A.I., Thomas, R.J., Kühne, M., Timothy, J.G., Hassler, D.M., Siegmund, O.H.W.: 1995, SUMER – Solar Ultraviolet Measurements of Emitted Radiation. *Solar Phys.* **162**, 189. DOI. ADS.
- Winebarger, A.R.: 2012, The Frequency of Heating in Active Region Cores: Results from the Fifth Coronal Loops Workshop. In: Golub, L., De Moortel, I., Shimizu, T. (eds.) *Fifth Hinode Science Meeting*, *Astronomical Society of the Pacific Conference Series* **456**, 103. ADS.
- Winebarger, A.R., Warren, H.P., Schmelz, J.T., Cirtain, J., Mulu-Moore, F., Golub, L., Kobayashi, K.: 2012, Defining the “blind spot” of Hinode EIS and XRT temperature measurements. *Astrophys. J. Lett.* **746**, L17. DOI. ADS.

- Yan, L., Peter, H., He, J., Tian, H., Xia, L., Wang, L., Tu, C., Zhang, L., Chen, F., Barczynski, K.: 2015, Self-absorption in the solar transition region. *Astrophys. J.* **811**, 48. [DOI](#). [ADS](#).
- Yoon, P.H., Kim, S., Choe, G.S., Moon, Y.-J.: 2016, Revised model of the steady-state solar wind halo electron velocity distribution function. *Astrophys. J.* **826**, 204. [DOI](#). [ADS](#).
- Young, P.R., Watanabe, T., Hara, H., Mariska, J.T.: 2009, High-precision density measurements in the solar corona. I. Analysis methods and results for Fe XII and Fe XIII. *Astron. Astrophys.* **495**, 587. [DOI](#). [ADS](#).
- Young, P.R., Doschek, G.A., Warren, H.P., Hara, H.: 2013, Properties of a solar flare kernel observed by Hinode and SDO. *Astrophys. J.* **766**, 127. [DOI](#). [ADS](#).
- Younger, S.M.: 1981, Electron impact ionization cross sections and rates for highly ionized atoms. *J. Quant. Spectrosc. Radiat. Transf.* **26**, 329. [DOI](#). [ADS](#).
- Zharkova, V.V., Arzner, K., Benz, A.O., Browning, P., Dauphin, C., Emslie, A.G., Fletcher, L., Kontar, E.P., Mann, G., Onofri, M., Petrosian, V., Turkmani, R., Vilmer, N., Vlahos, L.: 2011, Recent advances in understanding particle acceleration processes in solar flares. *Space Sci. Rev.* **159**, 357. [DOI](#). [ADS](#).
- Zouganelis, I., Maksimovic, M., Meyer-Vernet, N., Lamy, H., Issautier, K.: 2004, A transonic collisionless model of the solar wind. *Astrophys. J.* **606**, 542. [DOI](#). [ADS](#).
- Zouganelis, I., Meyer-Vernet, N., Landi, S., Maksimovic, M., Pantellini, F.: 2005, Acceleration of weakly collisional solar-type winds. *Astrophys. J. Lett.* **626**, L117. [DOI](#). [ADS](#).
- Zweibel, E.G., Yamada, M.: 2009, Magnetic reconnection in astrophysical and laboratory plasmas. *Annu. Rev. Astron. Astrophys.* **47**, 291. [DOI](#). [ADS](#).